A DIAPER-EMBEDDED PAPER-BASED SENSING PLATFORM WITH ON-BOARD URINE-ACTIVATED BATTERY FOR URINARY TRACT DISEASE SCREENING

by
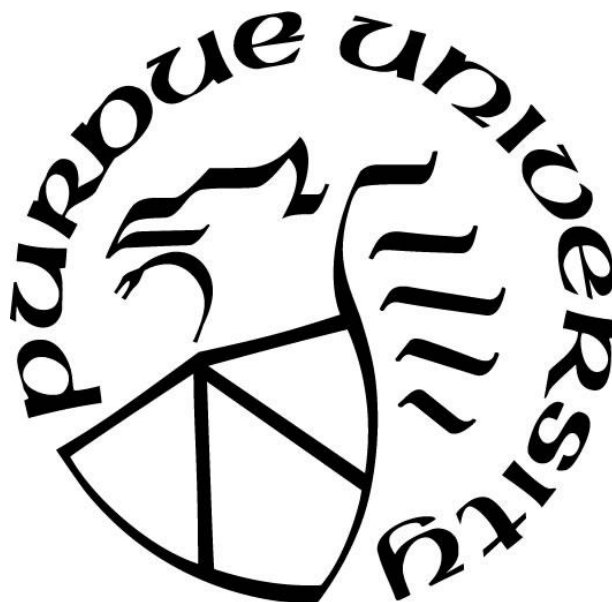
Wuyang Yu

A Dissertation

Submitted to the Faculty of Purdue University

In Partial Fulfillment of the Requirements for the degree of

Doctor of Philosophy

School of Electrical & Computer Engineering

West Lafayette, Indiana

December 2018

THE PURDUE UNIVERSITY GRADUATE SCHOOL
STATEMENT OF COMMITTEE APPROVAL

Dr. Babak Ziaie, Chair

    School of Electrical and Computer Engineering

Dr. Zhihong Chen

    School of Electrical and Computer Engineering

Dr. Çağrı A. Savran

    School of Mechanical Engineering

Dr. Byunghoo Jung

    School of Electrical and Computer Engineering

Approved by:

    Dr. Pedro Irazoqui

        Head of the Graduate Program

After some thinking, I decide to dedicate this dissertation to all the Ph.D. students who also pondered in many nights, struggled through many failures, yet experienced the pure joy of resolving problems with no obviously existing answers. I would also like to dedicate this dissertation to my wife and my parents for their unreserved support and love throughout my graduate study.

ACKNOWLEDGMENTS

First, I want to sincerely thank Prof. Babak Ziaie for the past 6 years being my advisor. You have always been providing me insightful research suggestionst and supporting my growth. It was my privilege to work in the Ziaie group, learn from you and all other team members and gain research experience, which has helped me transition into my new career and will continue to be beneficial to me lifetime.

I also would like to thank Prof. Byunghoo Jung, Dr. Charles R. Powell, Mr. Weeseong Seo and Mr. Tianlin Tan for all the collaborative assistance through my dissertation research.

In the end, I also want to thank Drs. Girish Chitnis, Rahim Rahimi and Manuel Ochoa for their generous help on my transitioning from a college student to a graduate researcher in all perspectives.

TABLE OF CONTENTS

LIST OF TABLES

LIST OF FIGURES

ABSTRACT

Author: Yu, Wuyang PhD
Institution: Purdue University
Degree Received: December 2018
Title: A Diaper-Embedded Paper-Based Sensing Platform with On-Board Urine-Activated
        Battery for Urinary Tract Disease Screening
Committee Chair: Babak Ziaie

Urinalysis is a common laboratory test used for diagnosis of a variety of systemic and genitourinary diseases. Although, collection of sample for urinalysis is extremely easy, when performed during an office visit, in pediatric and geriatric populations, who use diaper, such collection is not trivial and can result in missing important diagnostic information. For example, urinary tract infections (UTIs), are a major source of morbidity in incontinent elderly with dementia who cannot communicate their symptom to their caregivers. Although most UTIs are easily treatable with antibiotics, if not identified and treated timely, they can cause ascending infection, loss of kidney function, sepsis, and possible death. Deployment of smart, autonomous, diaper-embedded systems that can detect early signs of urinary dysfunction can have a significant impact on healthcare of our rapidly aging population. In this dissertation, I propose a diaper-embedded, low-cost, and disposable sensing platform comprising of a urine-activated battery and sensors for detection of nitrite (a surrogate for UTI), red blood cells (hematuria), and protein (proteinuria). I will first discuss my efforts to develop an optical/colorimetric nitrite sensor and a urine-activated power source, all fabricated on a hydrophobic paper/polymeric substrate through laser-assisted machining and lamination-assembly. The system stays in a dormant state until wetted by urine, after which the on-board power source is activated, awakening the rest of the measurement system (i.e., a light emitting diode, a photodetector, interface electronics, and a low-power Bluetooth module) and transmitting the presence or absence of nitrite in the urine to vicinal caregivers in a point-of-care and autonomous fashion. Thorough characterization of the performance and reliability analysis of the platform are also presented to envision its use as an end product. Afterwards, I will discuss the characterization of sensors, based on similar principle, for detecting red blood cells (hematuria) and protein (proteinuria), and the extendibility of the proposed platform for a multi-parameter system measuring nitrite, blood, and protein in the urine. Finally, I will conclude with other possible applications besides urinalysis for the proposed system.

CHAPTER 1. INTRODUCTION

1.1 Background of Urinalysis

As a filtrate of blood, urine has been considered as an important health barometer to be analyzed for the diagnosis (urinalysis) of various systemic and genitourinary diseases, primarily UTIs, kidney disease and diabetes. [1] These diseases are under a great public attention due to their prevalence and severity. For example, UTIs are some of the most common infections in the body, of which the societal costs are approximately $3.5 billion yearly in the United States [2]; 10% of American adult population have some level of chronic kidney disease (CKD, which may turn into kidney failure) and kidney disease is the 9th leading lethal cause in the United States [3]; 422 million adults have diabetes and 1.5 million deaths are directly related to it per year [4]. Some of the diseases are asymptomatic in their early but treatable stages, when urinalysis can provide timely detection and prevent them from further causing severe health problems.

Conventional urinalysis technologies involve macroscopic, microscopic and chemical analysis and urine culture. Macroscopic analysis involves the evaluation of the physical appearance (color, cloudiness, and odor) of urine, which can be traced back to 400 BC in ancient Egypt. Though it is of little diagnostic value itself, visual macroscopic assessment is usually interpreted in conjunction with microscopic and chemical examination to confirm what is in the urine sample. Normal urine would be mostly a transparent liquid in pale yellow ascribed to urobilin or urochrome. [1, 5, 6] Irregular urine color or clarity could be the results of dehydration (dark honey or amber), ingestion of certain medications or foods (for example, blackberries and beets may cause red urine), or unfortunately diseases (hematuria by the presence of brown-red turbidity, led by damaged kidney). Figure 1.1 illustrates the probable causes for abnormal urine appearances. [6] In addition, a whiff of strong smell in urine might also result from some foods or a sign of UTIs, diabetes, and other diseases. [1, 5]
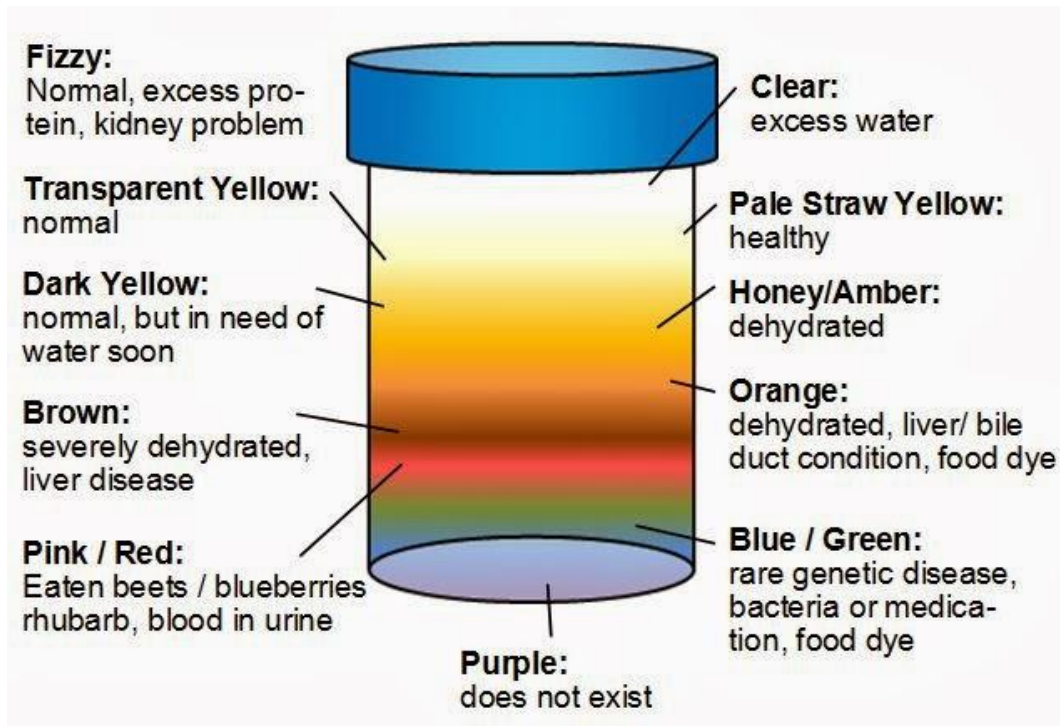
Figure 1.1 Human urine color meaning chart [6]

Microscopic analysis examines urine samples under a microscope for any cells, casts, crystals or bacteria. [7] It is typically conducted when irregular outcomes are obtained in macroscopic assessment or chemical examination, which otherwise is quite time-consuming. Urine samples are usually centrifuged to concentrate the sediment inside with the supernatant decanted. Then, the sample is inspected at either low power or high power to identify and count the substances. Common seen substances include red blood cells (RBCs), white blood cells (WBCs), epithelial cells (EC), casts, bacteria, crystals, etc. In healthy people, a trace amount of RBC (0-5 RBCs per high power field), WBC (0-5 WBCs per high power field), EC (few per low power field), casts (0-5 hyaline casts per low power field) and bacteria (contaminated during collection unless with a clean-catch) are present in urine samples because of normal physiological activities. [8] Nevertheless, increased amount of those substances may be a sign of urinary tract infections, inflammation or kidney diseases. In addition, urine culture is usually as a test for the identification of exact bacterial species, to deploy the most effective treatment. Generally, despite being accurate in diagnosis, laboratory or hospital tests (microscopic urinalysis, urine culture, etc.) are time-consuming and not cost-effective as an initial screening means.
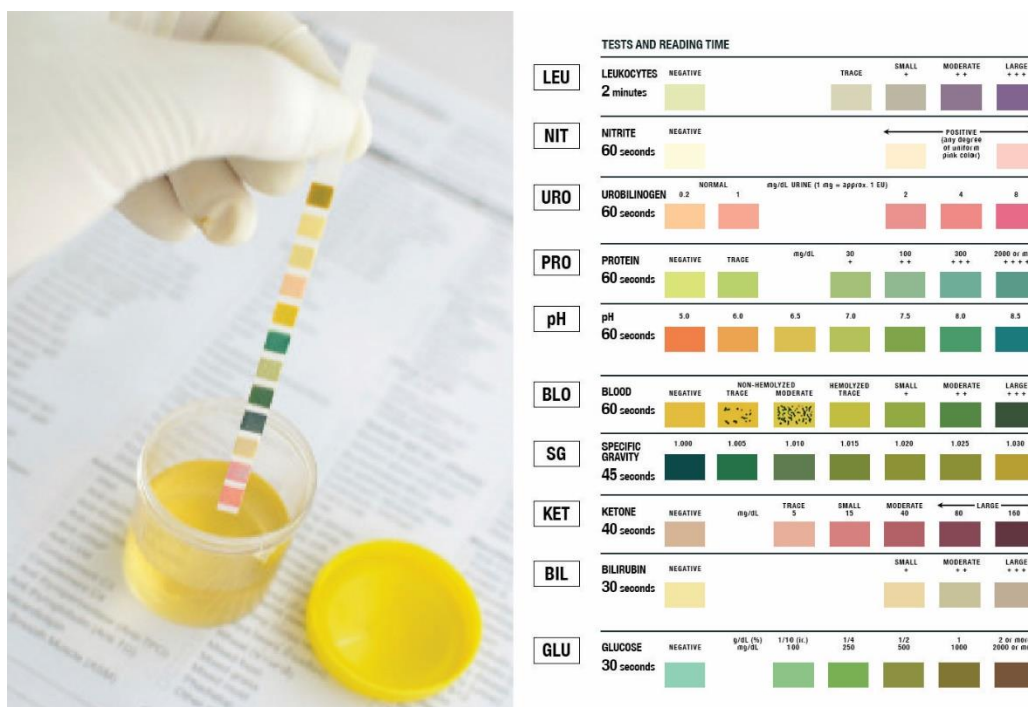
Figure 1.2 Multi-parameter dipstick use and color chart

Therefore, in most cases, people use commercially available test strips implementing chemical assays as a rapid and economical method for the early detection of urological diseases. [9, 10, 11] Chemical assay is primarily applied to inspect and quantify certain parameters related to specific diseases (such as nitrite and leukocyte esterase related to UTIs, blood and albumin implying kidney damage, etc.) in the urine sample. Dipstick technologies have been developed and commercialized constantly since 1950s [1] using a special strip as the carrier impregnating colorimetric chemical reagents on a test pad responsive to certain substances in the urine sample. Being rapid and cost-effective in diagnosis, urine test strips have become a reliable instrument in clinical practice and self-testing setting with the consistent improvement of color stability and gradation. Figure 1.2 demonstrates the operation of a multi-parameter test strip with a urine sample. The strip is dipped into the urine specimen for no longer than one second, and then chemical reactions occur within 1~2 minutes, changing the colors of respective pads, which can be compared to a reference chart. Though no direct diagnosing conclusions are drawn based the color comparison, dipsticks serve as the first line of screening for further uroscopy (microscopic assessment), which is suitable for early detection, treatment monitoring and patient self-testing.

1.2 Motivation of Developing an Autonomous Urinalysis Platform

It is important to note that, both the in-laboratory/hospital and the dipstick-based urinalysis require proper collection, transportation and storage of urine samples to produce reliable results. Usually, a clean-catch of midstream urine (first morning urine preferably) with cleansed external urethral meatus is necessary. Moreover, the collected urine specimen should be tested within two hours [12] right after urination to rule out any potential false results owing to the instability of the substances of interest [1].

In most cases, urine collection extremely easy, but when performed in pediatric and geriatric populations, such collection is not trivial. Both the abovementioned groups may require the caregivers' aid with urine specimen collection, which is cumbersome and inconvenient. What's worse, both populations have difficulty communicating their urinary discomfort and associated symptoms to the caregivers. Thus, a fully automated platform incorporating the existing urinalysis technology is highly desired to benefit the infant and elderly users for the prevention of serious diseases.

One typical urinary disease of great and wide interest is urinary tract infection (UTI), mostly caused by bacteria (especially E. coli) invading the urethra. UTIs are among the most common infection in the body (the most common nosocomial infection) accounting for nearly 10 million ambulatory and two million emergency department visits in the United States, women especially prone to getting UTIs. [2, 13, 14, 15] Even though most UTIs are easily treatable with antibiotics, without the identification and prescription in a timely manner, they can become a major source of additional morbidity (ascending infection, loss of kidney function, and sepsis) in preverbal children and elderly patients suffering from dementia (the two main groups using diapers and at increased risk of UTI [16], unable to discern and refer symptoms of infections). In particular, a small number of infants [17] and up to 50% of the geriatric group suffer from asymptomatic episodes of UTIs [16], which further complicates the diagnosis.

Several efforts have been devoted into the development of UTI analytical devices embedded into diapers beneficial for infants and elderly populations. Smart diaper by Pixie Scientific (http://www.pixiescientific.com/, Figure 1.3) has a colored panel (mounted in front of the diaper)

with embedded dry reagents which upon contact with urine result in discrete color changes associated with the presence of UTI biomarkers. A smartphone is needed to take a picture of the colored panel, analyze the data, and sends an alert to a doctor if a problem is detected. The microfluidic paper-based device introduced by Tao [18] is an extension of dipstick technology incorporating nitrite assay in the reagent zone on the device. These devices are not autonomous and require a timely manual inspection of the strip color in the diaper or otherwise the results are subject to undesired errors and invalidity (color fading or instability of the reagent [19]).

Figure 1.3 Pixie Scientific: Smart Diaper

In this thesis, I will first present my effort on the development of a disposable autonomous urine-activated urinary nitrite sensor, which combines a test strip containing the colorimetric reagent utilized in most conventional dipsticks, a LED/photodiode detection unit, and a Zn-Cu battery, fabricated on a hydrophobic paper substrate. This flexible device can be integrated with power management (for voltage regulation of the battery) and signal processing circuits and a wireless transmitter (such as BLE module), which could be embedded onto a diaper. The on-board battery is activated by urination, otherwise in the dormant status, awakening the sensing unit and sending the detected data to a vicinal receiver. Particularly, I will elaborate some optimization plans on the platform design for improving performance, analyze the reliability of the system correlated with its possibility as an end product. Second, I will discuss the development of two other sensing systems for measuring blood and protein in urine using similar designs, as well as the integration

of multiple sensors on one platform. After all, I will make a conclusion on the proposed diaper-embedded urinalysis platform and envisage its exertion in other healthcare applications.

CHAPTER 2.   URINE-ACTIVATED PAPER BATTERY

This chapter presents the design and characterization of a water (or urine) activated paper-based battery, providing the power source required for bio-chemical sensing and signal transmission, which are the primary functions we should have in the diaper-embedded sensing platform. The battery activated by urination is a Zn-Cu electrochemical cell fabricated on a wax paper substrate. Zn-Cu electrochemistry is chosen for the easy availability and processability of zinc and copper tapes and stability of the electrolyte chemicals enabling long shelf life. Wax paper is selected given that it is hydrophobic, inexpensive, and allows for easy integration and final heat lamination/sealing of the device.

2.1 Motivation of developing paper-based power source
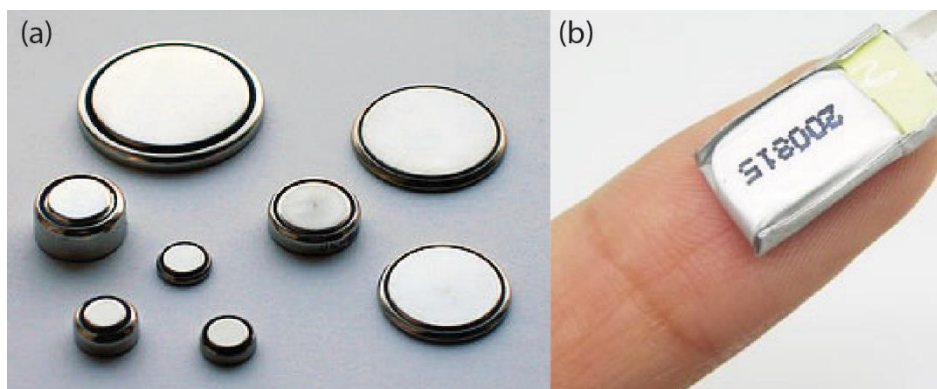
Figure 2.1 (a) Coin cells; (b) Lithium polymer battery.

There is no doubt that commercial batteries [20] of small dimensions, especially height, can be incorporated directly into the system, as long as they can provide enough power for the bio-chemical sensing and wireless transmission (high drain in a short period) within the time of interest. Figure 2.1 provides two promising candidate categories if one wants to employ commercial batteries. For example, coin cells or button cells, which are used to power small portable electronics such as watches and calculators, are available in sizes as tiny as D4.8mm×H1.6mm. The common electrochemical systems in miniature coin cells are alkaline, silver, zinc-air, lithium, and mercury (gradually dropped owing to its toxicity). Alkaline ($Zn-MnO_2$) batteries are preferred in situations where the price is considered prior to the performance. Zinc-air (metal-air) batteries

have higher capacity than other types since they use air as the cathode, while they are prone to fast self-discharge regardless of use once the seal against air is removed. Silver (Zn-AgO) performs well at the output stability. Lithium batteries use lithium instead of zinc as the anode and stand out for their high charge density, but they are usually large in diameter (20 mm), costly, and safety risky. Figure 2.1b is an example of lithium polymer (LiPo) batteries. Not to be confused with lithium batteries, a LiPo battery is a rechargeable battery based on Li-ion technology in pouch format (polymer casing rather than polymer electrolyte). It is rechargeable (not necessary for the biomedical sensing application discussed in this article), lightweight, flexible (than other types) and good in electrical performance, but usually expensive.

However, considering the needs we desire out of the on-board (in diaper) power source in the urine diagnostic application: sufficient power for biochemical sensing (including data collections, low drain over a few minutes) and wireless transmission (high drain within less than a minute), flexibility, small and thin dimensions, low cost, manufacturing compatibility with the sensing modules, preferably incorporating a urine-activation mechanism (otherwise power-intensive continuous monitoring would be necessary or a urination-driven electrical switch is required.), we decide to develop a flexible paper-based water-activated power source to be integrated into the diaper-embedded sensing system.

2.2 Review on Paper-based power source

As one of the oldest and most copious material, paper has come back into sight as the platform/skeleton for lab-on-a-chip devices in recent years essentially for the following motivations: (i) Paper is an extremely low-cost and common material; (ii) paper has an inborn capillary property due to its porous cellulose matrix, no external forces needed to move fluids within the paper; (iii) paper is flexible and lightweight; (iv) paper is disposable. Additionally, these advantages of paper as substrate have been further exploited by incorporating cutting-edge machining technologies and smart materials (e.g. piezoelectric, magnetic and optical materials). Therefore, paper will have a broad impact in many areas including point-of-care health care products and consumer/wireless electronics of immense benefit and utility especially in developing world, where biologically-derived resources are abundant whereas technological infrastructures are in scarcity.

Over hundreds of years, paper has been applied in applications apart from print industry like litmus impregnated pH strips, based on its fibrous nature, hydrophilicity and good bonding ability with many chemicals. Nowadays, enormous patterning processes have been developed by many research groups contributing to realizing lab-on-a-chip devices on paper, like photolithography [21], wax printing [22], screen printing, ink-jet printing [23] and laser treatment [24]. Along with the abovementioned techniques, numerous paper-based electronics [25] have been demonstrated, for instances, flexible field effect transistors [26], photodiodes [27], and electrowetting display [28]. The pioneering work using patterned microfluidic paper for medical diagnosis was reported by the Whitesides group [21]. They lithographically patterned SU8-soaked paper to create microfluidic channels for colorimetric glucose and protein sensing in urine. However, either the functionality or the application of the aforementioned paper devices is limited ascribing to the lack of on-board power source. For example, colorimetric devices are restricted to visual inspection though paper is a natural fit for colorimetrically biomedical/biochemical diagnosis, which is also the situation our urinary tract related disease screening platform (dipstick technology based) faces. Despite being a possible solution, the use of commercial standard batteries increases the expense, brings the difficulty of integration (either on the manufacturer side or for the user) and poses challenges in disposing the devices. Therefore, batteries or other forms of power source directly fabricated on paper are in need to provide an easy integration with paper electronics and build a low-cost, self-powered and disposable platform along with sensing components.

To date, there have been several types of paper-based energy storage devices, which can be classified into the following categories according to the operating principles [29]: electrochemical batteries [30, 31, 32], biofuel cells [33, 34] lithium-ion batteries [35] and supercapacitors [36]. For low-power (~10 µW to ~1 mW) applications such as biosensing, electrochemical batteries and biofuel cells are preferable while lithium-ion batteries and supercapacitors satisfy larger power requirement. On the other hand, lithium-ion batteries and supercapacitors have carbon nanotubes or graphene embedded in the paper during the fabrication process, which raises the cost and overshadows the use of cheap paper substrate. Aside from the enhanced cost, lithium-ion batteries or supercapacitors may contain environmentally unfriendly materials, requiring specific disposal methods. Furthermore, compared to the low power generation of microbial fuel cells (MFCs) and

the limited lifetime of enzymatic biofuel cells (EBFCs), electrochemical batteries are probably a better choice for a clean and durable energy generating a considerable power (~1 mW). Lee et. al. pioneered on fabricating a single-cell electrochemical battery activated by urine on paper [30]. They used existing laminating technology to encapsulate Magnesium strip, CuCl-impregnated filter paper and Copper layer within two plastic pouches (6 cm × 3 cm), achieving a maximum power of 1.5 mW for a few minutes. Nicole K. Thom et. al. demonstrated a microfluidic Ag-Al battery by stacking multiple layers of paper and tapes and its application in detecting β-D-galactosidase [31]. Sung-Sheng Chen et. al. introduced cellophane film as an ion-exchange membrane in their origami paper-based fluidic Al-Cu batteries to separate two electrodes and promote the stability of output, yet requiring the pre-wetting of the cellophane paper [32]. However, most reported batteries are either expensive (due to the cost of Ag) or cumbersome in fabrication or operation. We report on a rapid process of fabricating flexible Zn-Cu electrochemical batteries by laminating laser-patterned Zinc tape, Copper tape, filter papers and wax paper/tape covers, which can potentially incorporate roll-to-roll technology to scale up for mass production.
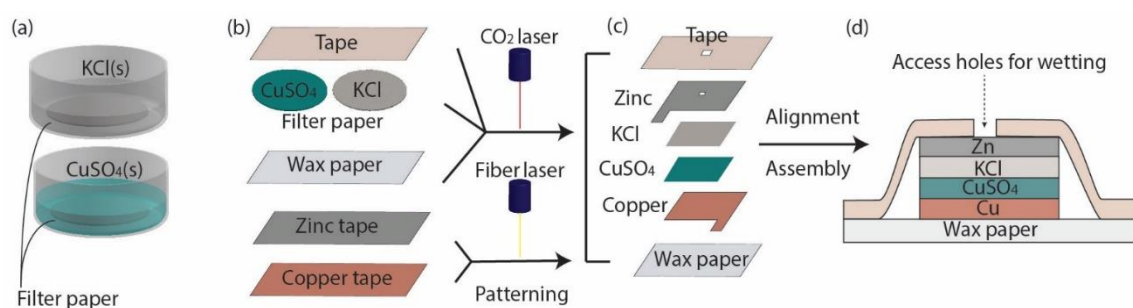
Figure 2.2 Fabrication process of the urine-activated battery. (a) Impregnating filter papers with salts. (b) Laser-defining of the wax paper substrate, the active materials and the covering tape; (c) Alignment and assembly; (d) Schematic structure of the battery.

2.3 Design and Fabrication Process

Figure 2.2 illustrates the schematic cross-section and fabrication process of a single-cell battery. The Zn-Cu electrochemistry provides a theoretical potential difference of 1.1 V per cell, (which will be elucidated in Section 2.4.1). One Zn-Cu cell is composed of two half-cells with different potentials, connected by a salt bridge. One half-cell is Cu electrode/$CuSO_4$(s) and the other is Zn electrode/$ZnCl_2$(s). The salt bridge is made of filter paper soaked with KCl to maintain the electrical neutrality within the two half-cells. Upon the wetting of the filter papers by the urine

through the windows/access-holes, the redox reactions are initiated via the moist salt bridge connecting both half-cells.

The different layers of the paper battery can be processed independently and stacked-up for assembly in the final step, Figure 2.2b. First, Whatman filter papers (Whatman, Qualitative, $\varnothing$ 90 mm, 180 µm thick) are immersed in KCl (0.1 M, 50 mL) and $CuSO_4$ (0.1 M, 25 mL) solutions, respectively, and left for desiccation[1], Figure 2.2a. Afterwards, dried filter papers along with other materials are patterned/machined using a commercial laser cutter (Universal Laser Systems, PLS6MW, 1.06 µm fiber laser in 50 watts, 10.6 µm CO_2 laser in 75 watts), Figure 2.2b. A wax paper (Reynolds Cut-Ride, 40 µm thick) is cut by the CO_2 laser into a 3 cm square substrate with surface marks matching the electrode areas for alignment. Then, copper and zinc (50 and 100 µm thick, respectively) tapes with an adhesive backing are cut into 2.5 cm squares with the 1.06 µm fiber laser to create the metal electrodes, Figure 2.2c. Using the CO_2 laser, filter papers soaked with $CuSO_4$ are shaped into corresponding squares as electrolytes overlapping the Cu electrodes while those with KCl are patterned as salt-bridge as well as the electrolytes for the Zn electrodes. A polyimide tape (VWR International) is also machined by the CO_2 laser to create access holes for allowing urine to seep into the filter papers and activate the battery. After the laser patterning steps, the battery is assembled through aligning and press-taping various layers, Figure 2.2d, and the final package is strengthened using a laminating machine (Apache, AL13P). The size of the fabricated single-cell battery is 3 cm × 3 cm. The fabrication process can be easily used to fabricate multiple parallel or series cells.

2.4 Electrical Characterization and Discussion

Various designs (stacking electrodes as in Figure 2.2d and planar geometry enabling multi-cell configuration as in Figure 2.3) were prepared and characterized for the Zn-Cu paper battery. The photographs of batteries in stacking-electrode configuration and planar multi-cell layout individually are presented in Figure 2.4.

---

[1] The concentrations of KCl(s) and $CuSO_4$(s) don't have to be 1 M as long as the dried filter papers contain reproducible average weight/area of chemicals. For example, a φ120 mm filter paper can go with 10 ml 0.89 M KCl and 10 ml 0.44 M $CuSO_4$.
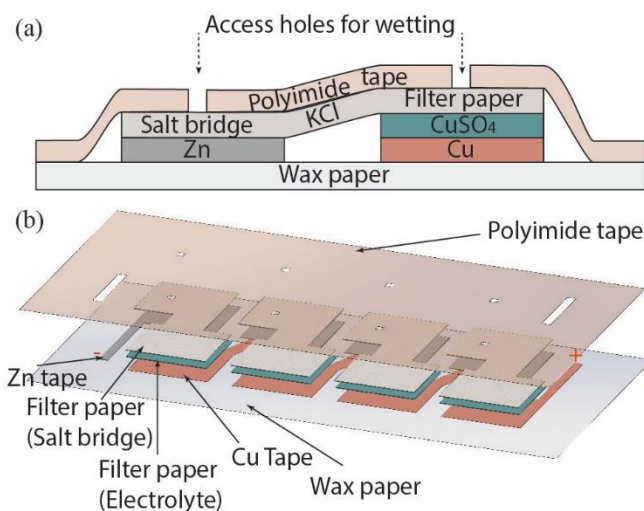
Figure 2.3 Planar design of multi-cell paper battery. (a) Cross-section view. (b) Exploded view.
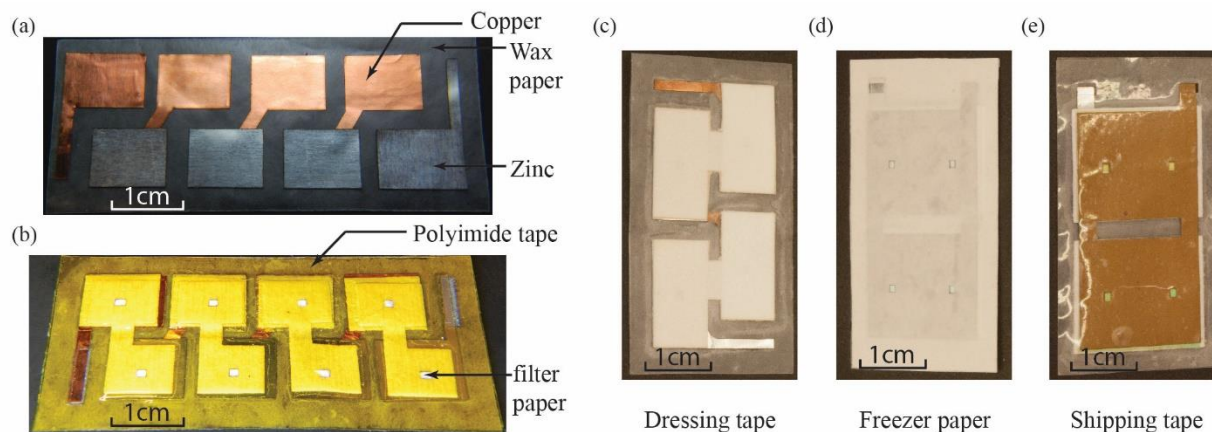
Figure 2.4 Photographs of paper batteries. (a) Patterned copper and zinc tapes adhere to wax paper. (b) A 4-cell battery packaged by polyimide tape. (c) A 2-cell battery packaged by conformable dressing tape. (d) A single-cell stacking-electrode battery packaged by freezer paper. (e) A single-cell stacking-electrode battery packaged by shipping tape.

2.4.1 Open circuit voltage and electrochemistry behind paper battery

Figure 2.5 demonstrates open circuit (OC) voltages of planar-designed batteries with different number of cells after activation. The average measured value for individual cell is 0.995±0.036 V/cell, slightly lower than the theoretical 1.1 V.
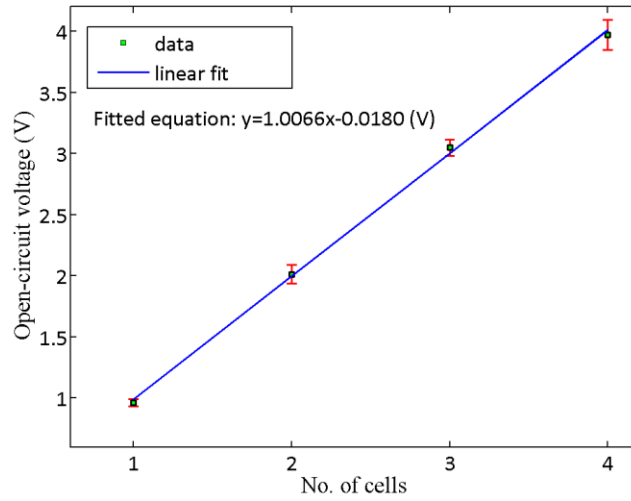
Figure 2.5 OC voltage vs. number of cells[2]

To understand what gives rise to the voltage drop, we should first inspect what factors affect electrode potential. Equilibrium electrode potential can be computed via Nernst equation (this is not a definition expression): [37]

$$U_H = U_H^0 + \frac{RT}{zF} \ln a_{M^{z+}} . \tag{2-1}$$

U_H^0 is the standard potential in a solution of their own salts with metal-ion activity 1, R is the gas constant, z is the valency of the metal ions (e.g. +2 for Cu^{2+}), F is the Faraday constant and $a_{M^{z+}}$ is the chemical activity of the potential-determining metal ions in the solution. The chemical activity can be related to the concentration of the species in the solution,

$$a_{M^{z+}} = \gamma_{M^{z+}} c_{M^{z+}} , \tag{2-2}$$

where $\gamma_{M^{z+}}$ is the activity coefficient [38], which is usually less than 1 for non-volatile solutes in aqueous solutions and approaches unity at low concentrations.

Therefore, the Zn-Cu electrochemical cell potential can be written as

---

[2] Unless specified in this dissertation, an error bar in a figure represents the sample to sample standard deviation of a data point.

$$U_{Cell} = U_{Cell}^0 + \frac{RT}{2F} \ln \frac{a_{Cu^{2+}}}{a_{Zn^{2+}}} = 1.1037 + 0.0296 \log_{10} \frac{a_{Cu^{2+}}}{a_{Zn^{2+}}}, (V). \qquad (2\text{-}3)$$

Note that the value of U_{Cell}^0, 1.1037 V is obtained by calculating the difference between zinc and copper standard electrode potentials (-0.7618 V and 0.3419 V) [39], which are measured respectively by connecting the half-cell electrodes in standard conditions (1 M concentration, 1 atm, 25 °C) through a salt bridge to a standard hydrogen electrode. As is seen from Equation 2-3, the second term leads to the deviation from the standard cell potentials. Impurities in these chemical cells and the reaction temperature (21~24 °C) lower than standard (25 °C) might contribute partly to the 0.1 V loss though at a very low level (<1%) in this scenario, so we need to take a closer look on the potential-determining metal ions.

The Cu^{2+} concentration can be estimated based on the loaded $CuSO_4$ amount and the activation water volume, which is around 0.8 M. However, we don't have any Zn^{2+} in the other half cell initially. In this case, the zinc electrode is unpoised (electrochemical equilibrium for the electrical double layer [37] around the electrode surface is not well defined by Zn/Zn^{2+} redox reaction but easily affected by other ions in the solution, if there are not enough zinc ions in the solution). It also means probing the cell potential will disrupt the old equilibrium as Zn dissolution rate increases with non-ideal current flow ($\approx$ 1.1V/10MΩ (input impedance of the used voltmeter) $\approx$ 100 nA) such that Zn^{2+} concentrations in the double layer and the solution will increase drastically. Hence, Nernst equation cannot be used to predict the cell potential, since it only applies for well-defined equilibrium electrode potential. Despite lacking information of Zn ion concentration, we could still make a rough estimate with increased dissolved Zn (note that other ions in the solution like K^+ are still affecting the electrochemical equilibrium and the electrode potential). Tentatively, I choose the effective zinc concentration, including influence from other ions in the solution, as 0.0001 M based on the lower detection limit of a Zn ion-selective potentiometric sensor [40]. Then, $a_{Zn^{2+}}$ is about 0.0001 and $a_{Cu^{2+}}$ is about 0.4*0.8=0.32, so the deviation term in Equation 2-3 would be 0.1038 V and the cell potential is 1.21 V. This is contradicting the measured voltage 0.99V. Even taking the activity of K^+ at 0.9 M in the battery as the value of $a_{Zn^{2+}}$ stills results in 1.09 V (>0.99 V) by calculation. Therefore, there exist other sources of the offset between experiment and theory and we might as well hypothesize that the second term doesn't cause much deviation from

standard equilibrium potential 1.10 V. Excluding the resistive loss over the negligible internal resistance (~1 kΩ, refer to section 2.4.2) compared to the input impedance of voltmeter (>10 MΩ), two possible candidates are overpotential and migration of copper ions.

Overpotential is termed for the difference between the working potential and the Nernst equilibrium potential, as to an electrode with net external current instead of in thermodynamic equilibrium. It may include transfer overpotential, concentration overpotential and resistance polarization. [37] Transfer overpotential is primarily to overcome the electric field on the electrode surface to transfer charge carriers (ions and electrons) between metal and solution, to produce an external current. On one electrode, the relationship between the external current density i and the transfer overpotential ΔU near Nernst equilibrium can be expressed as Butler-Volmer equation

$$i = i_0 \left[\exp\left(\frac{zF\alpha^+}{RT} \Delta U \right) - \exp\left(-\frac{zF\alpha^-}{RT} \Delta U \right) \right],$$ (2-4)

where i_0 is the exchange current density at the equilibrium potential and α is the charge transfer factor generally around 0.5. Taking Zn/Zn^{2+} electrode into consideration, again, i_0 is unknown dependent on the experimental environment, but we might estimate it as the value for zinc corrosion in acidic solution [41], 1×10^{-7} A/cm^2. Approximately the electrode area is 1 cm^2, so i is 100 nA/1 cm^2 = 1×10^{-7} A/cm^2. From 2-4, we can obtain that $\Delta U \approx 0.0126$ V, which agrees with the statement in [37] that transfer overpotential is low for dissolution and deposition of most metals. Similarly, for Cu/Cu^{2+} electrode, the exchange current density is approximated 5×10^{-5} A/cm^2 [42], so that $\Delta U \approx -0.0003$ V, where the negative sign means the net external current is from solution to electrode. As a result, the total transfer overpotential for the ~100 nA measurement current is estimated to be -0.0129 V, contributing partially to the voltage drop from the standard cell potential 1.10 V to the measured 0.99 V. Concentration overpotential and resistance overpotential represent the potential difference brought by the depletion of charge carriers/reactants on the electrode surface and the resistive loss in the current circuits, respectively. These two may not apply in the situation of low-level measurement current and early stage of activation on the battery.
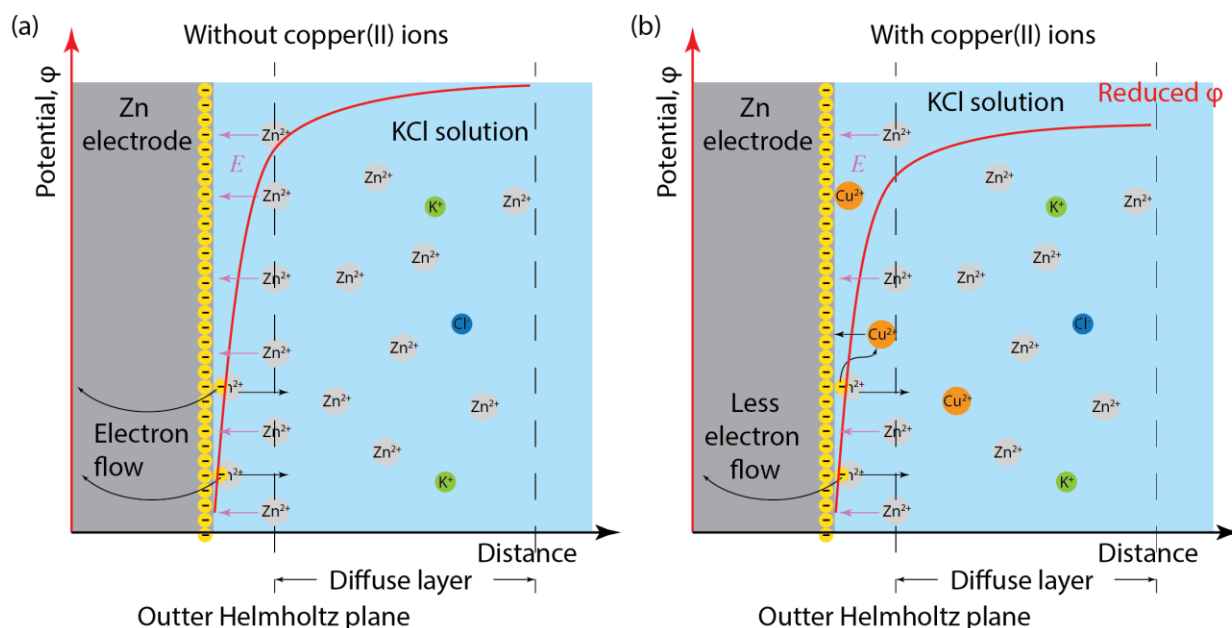
Figure 2.6 Schematic representation of an electrical double layer and the potential development across it at the Zn electrode/KCl solution interface in the condition where the KCl solution (a) doesn't contain Cu^{2+} and (b) contains Cu^{2+}, respectively.

The other conceivable cause is migration of copper ions through the salt bridge. Although the majority of copper (II) ions are in the vicinity of copper electrode initially, they will diffuse and deposit onto zinc electrode spontaneously given the stronger electronegativity of copper than zinc. This undesirable copper deposition at zinc electrode steals some portion of the electrons donated by the dissolved zinc ($Zn - 2e^- \rightarrow Zn^{2+}$), which should otherwise flow into the voltmeter, as is demonstrated in Figure 2.6. The current or electron flow shunting ascribed to this undesirable copper deposition induce a reduction in the measured OC voltage, since the digital voltmeter is getting smaller current that is proportional to measured voltage. It might be analogized to resistive loss from the perspective of working electrode overpotential since effectively measured current will be lessened. From the aspect of electrochemical equilibrium, copper deposition reduces or screens the negative surface charge density on the zinc electrode, thus reducing the electrical double layer potential difference based on Bockris/Devanathan/Müller (BDM) model [43], which is in fact the zinc half-cell potential by physical nature, also in Figure 2.6.

However, there still exist two concerns: 1. how many Cu^{2+} is present near the zinc electrode through diffusion from $CuSO_4$ reservoir? 2. how much potential drop will Cu^{2+} contribute? As to

the first concern, we may consider applying Fick's laws of diffusion to a simplified one-dimensional physics model from Figure 2.3a. Upon activation/adding water into the electrolyte reservoir, the copper ion concentration c at position x and time t can be described by

$$\frac{\partial c(x,t)}{\partial t} = D_{Cu^{2+}} \frac{\partial^2 c(x,t)}{\partial x^2} , \tag{2-5}$$

where $D_{Cu^{2+}}$ is the diffusion coefficient of Cu^{2+} in the solution. We may look into the concentration at the edge of KCl reservoir about 2 mm away from $CuSO_4$ reservoir, within the timeframe of 100 second (scale of the activation time for planar battery design to maximize OC voltage) to evaluate average Cu^{2+} level over the entire zinc electrode. The boundary condition can be approximately $c(0, t)$=1 M for origin x=0 chosen at the margin of $CuSO_4$ reservoir near the salt bridge as in Figure 2.3. Then, the solution is written as

$$c(x,t) = c(0,t) erfc(\frac{x}{2\sqrt{D_{Cu^{2+}}t}}) , \tag{2-6}$$

where erfc is the complementary error function. Substituting x=2 mm, t=60 s and $D_{Cu^{2+}}$ [44]into Equation 2-6, we have that the concentration over the zinc electrode at time point of 100 second is about

$$c(x = 2mm, t = 60s) = 1 \times erfc(\frac{0.2cm}{2\sqrt{7.3 \times 10^{-6} cm^2 / s \times 100s}}) \approx 1.66 \times 10^{-7} M \tag{2-7}$$

1.66×10^{-7} M Cu^{2+} seems to be not insignificant regarding influence on the electrical double layer potential difference. Yet, the magnitude of the influence is what the second concern I raised above is asking about. To my best knowledge, I haven't found any specific numerical model to quantify the potential drop of a Zn/Zn^{2+} electrode aroused by Cu^{2+} ions of a specific concentration in the electrolyte, but it might be experimentally analyzed and confirmed as follows.
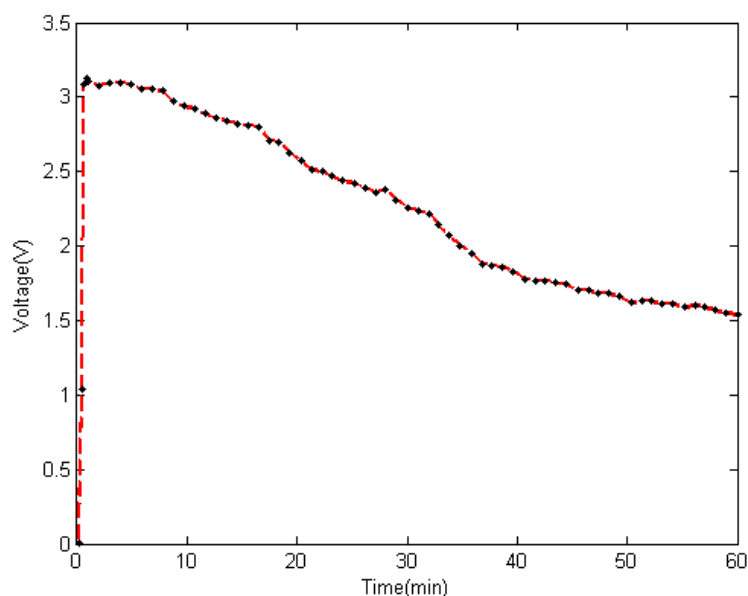
Figure 2.7 One-hour continuous measurement of a 3-cell planar paper battery

To eliminate or minimize the Cu^{2+} influence on Zn electrode, a 4 cm long, 1.5 cm wide filter paper (Whatman G1, 180 μm thick) salt bridge containing the same concentration (weight ratio) of KCl is used to connects two 50 ml of 1 M $CuSO_4$ and 1 M KCl solutions, the cell potential is measured to be 1.11V, which lasts longer than 1 hour. In this experiment, the sufficient large volume of KCl electrolyte for zinc electrode is more robust against copper ion diffusion within a certain duration, while in a compact paper battery, the electrolyte volume is only 0.2~0.3 ml, even comparable to the salt bridge (filter paper) loading capacity. The 0.1 V difference between the two scenarios may support the assertion that migration of copper ions is the dominant factor for the discrepancy of the measured cell voltage (0.99 V) in contrast to standard cell voltage. Besides, either half cell has a gradually decreasing potential due to the migration/deposition of copper ions (at Cu electrode) and the generation of solvated zinc ions/copper deposition (at Zn electrode), respectively, according to Nernst equation 2-3 along with the foregoing analysis on Cu^{2+}-affecting electrical double layer potential development at Zn electrode. The continuous OC voltage decline is observed in experiment and shown in Figure 2.7 taking a 3-cell battery OC voltage (declining from 3.18 V to 1.58 V in an hour) as an example, in which, likewise, copper migration/deposition at Zn electrode should be playing the main role.
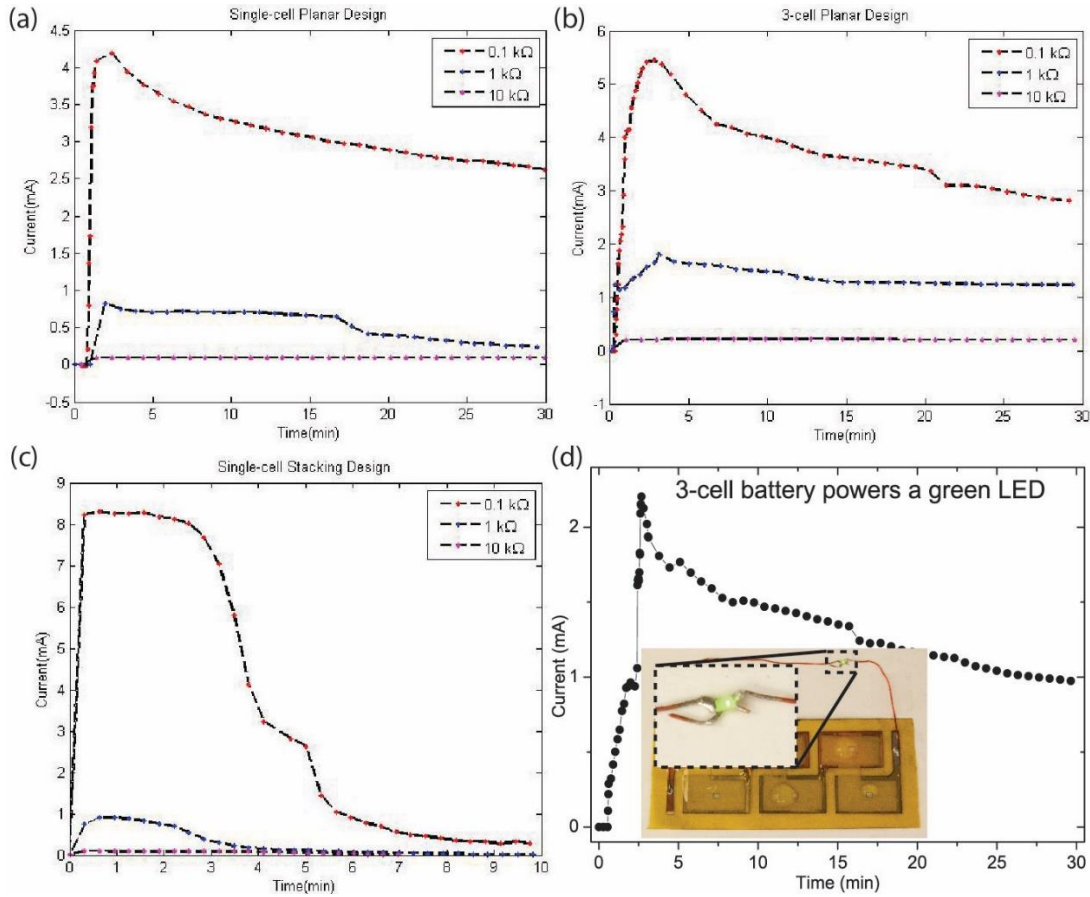
Figure 2.8 (a) Current vs. time for single-cell planar design battery with different loads. (b) Current vs. time for 3-cell planar design battery. (c) Current vs. time for single-cell stacking design battery (d) characterization and (d-inset) photographs of a 3-cell battery powering a green LED.

2.4.2 Battery performance and design consideration

Figure 2.8a-c shows the performances of 3-cell and single-cell batteries using both planar and stacking designs under different loads. Table 2.1 summarizes the power performance results. On the average, it took about 1~2 mins for planar-design batteries to maximize their output after activation. With a heavy load (R_L=0.1 kΩ), the 3-cell battery (electrode area of 16 mm $\times$ 8 mm per half-cell) provided a maximum current of 5.4 mA, which gradually dropped to 2.8 mA within 30 mins. The same design provides more stable currents for lighter loads, 1.24 mA for R_L= 1 kΩ and 0.20 mA for R_L=10 kΩ. The power performance (Table 2.1) indicates that the internal resistance of a 3-cell planar paper battery is around 1 kΩ. The single-cell planar geometry battery with larger electrode area (24 mm $\times$ 24 mm) displayed inferior performance (power output per unit area per cell) with a maximum power density (at 3 min) of 0.130 mW/cm^2, less than that of a

3-cell battery. This implies that in planar geometric designs, the lateral transportation of ions between Zn and Cu electrodes limits the performance. Overall, the power performance for planar layout batteries is not attractive for the proposed application (the LED and photodiode consumes around 1~2 mW) if including power consumption of interface circuits and the wireless transmitter. That being said, planar batteries are still suitable for some low-power uses such as indication. Figure 2.8d-inset shows the photograph of a 3-cell battery activated by deionized (DI) water to power a green LED (LG L29K-G2J1-24-Z, OSRAM). The current through the LED was measured at the same time, Figure 2.8e. It took around 2 mins for the output current to rise to the peak value 2.2 mA upon the addition of DI water onto the access holes at 30 secs. Afterwards, the current gradually declined to 1mA after about 24.5 mins.

Table 2.1 Paper battery characterization for different geometric designs and number of cells

	Power @ 3min (mW)			Power density @ 3min (mW/cm^2)		
$R_L(k\Omega)=$	0.1	1	10	0.1	1	10
1-cell planar	1.63	0.57	0.094	0.130	0.046	0.008
3-cell planar	2.94	3.10	0.40	0.383	0.404	0.052
1-cell stacking	5.43	0.116	0.067	0.943	0.020	0.012

The one-cell configuration stacking design with the same electrode area (24 mm × 24 mm) was also investigated (Figure 2.8c). It takes less than 20 seconds for a stack-design battery to maximize its current output. In the extreme case, this cell can supply approximately 6.9 mW (8.3 mA for RL=0.1 kΩ). At the time scale of our interest (3 min), allowing the system to perform the nitrite measurement and send the signal to the caregiver, single-cell stacking design is able to supply a power density of 5.43 mW for R_L=0.1 kΩ (Table 2.1). The high-power output only lasts for 3 mins, which is due to the fast and irreversible migration and deposition of Cu^{2+} onto the Zn electrodes through the filter paper salt bridge (Figure 2.2d).

Since the single-cell stacking design provides the best power performance in a small footprint despite it being slightly thicker (650 μm against 550 μm for planar design) and having a shorter activation period (~10 seconds), it was chosen for the integration into the sensing platform. Nonetheless, the characterized single-cell battery size (24 mm × 24 mm) may need to be

augmented for larger power output, depending on the power requirement from the whole electronic system. Detailed discussion on determining the size of the battery will be unfolded in Section 4.1.2.

CHAPTER 3. COLORIMETRIC NITRITE SENSING ON PAPER PLATFORM

This Chapter basically illustrates the importance of monitoring urinary nitrite, reviews existing technologies of measuring nitrite, and in the end depicts the system architecture and working mechanism of the proposed paper-based colorimetric nitrite sensing platform. Also, the characterization of the system and some preliminary experimental results are presented as well as discussion on the system performance.

3.1 Introduction to urinary nitrite

Urinary nitrite, produced by nitrate deforming bacteria (e.g. E. coli.), is one of the most important surrogates [45] implying a bacterial UTI, since it is absent in bacteria-free urine and around 50% to even 90% (favorably with first morning urine) of bacterial UTIs are detected with nitrite test. [1] Thus, it is of a high interest to choose nitrite (specifically for UTIs) as the beginning parameter that the smart diaper urinary tract disease sensing platform includes before future development.

It is crucial to note that the urinary nitrite concentration cannot be correlated to the severity of the UTI, and that the absence of nitrite doesn't fully reliably exclude the existence of UTIs, given that microbial count and nitrate intake can vary or even the infective microbe doesn't generate nitrite. [1, 45, 46] Therefore, supplementary diagnostic parameters such as leukocytes (or leukocyte esterase) and blood tests [45] are beneficial.

3.2 Nitrite detection technologies review

Dipstick implementing colorimetric nitrite assay (e.g. Griess reagent [47, 48, 49]) is one of most commonly used technologies to detect nitrite, especially urinary nitrite, with a practical detection limit of 0.5 ppm. [1] The test principle is typically the reaction of nitrite with sulfanilamide to form a diazonium compound, which undergoes a coupling with the other reagent (e.g. N-(1-Naphthyl)ethylenediamine) to give a pink or red azo dye. The color intensity can then be compared to a reference chart for the estimation of the nitrite concentration.

From a broader perspective, nitrite detection technologies can be classified into colorimetric, electrochemical, spectrophotometric, column/capillary and biosensing methods based on the test principles [50, 51]. Colorimetric techniques are based on color changing chemical assays as mentioned before: in the mainstream the Griess test forming an azo dye. Aside from visually inspecting the dipstick test results, there are also other routes taking use of the colorimetric nitrite assays: camera-assisted coloration analysis [18, 52] (e.g. Smart Diaper by Pixie Scientific) and spectrophotometry either in transmission [53] or reflection [54, 55] (e.g. Urisys 1100® from Roche) fashion. Comprehensive discussion about this branch pertaining to this dissertation is introduced in the following subsections.

Current electrochemical detection techniques [56, 57, 58] are mainly rooted in amperometric or voltammetric measurement through nitrite oxidative/reductive processes, which, though would be more sensitive compared to dipstick, suffer from poor portability owing to the instrumentational requirements (e.g. bulky potentiostats) and electrode fouling [58]. Potentiometric [59, 60, 61, 62] nitrite detection relies on nitrite ion selective electrode (ISE), which usually contain a PVC membrane embedding nitrite-selective ion-exchangers or ionophores, generating a potential responsive to nitrite concentration in the surround aqueous environment, similar to the mechanism of electrochemical cell. Potentiometric measurement is often favored owing to its promising miniaturization capability and procedurally simplicity, which shares the same me however still need improvement on its detection limit (typically $>1\sim10$ µM, equivalent to $0.05\sim0.5$ mg/L), susceptibility to environmental interferences, potential drift and unstable reference potential. [51] In addition, the fabrication of the electrodes for nitrite electrochemical sensors (including Pt, Ag, ISE) could be very costly. Bio-sensing [63] nitrite detection is a sub-branch of electrochemical technology, which has been attracting increased interest ascribed to the supposed higher selectivity and specificity of biological recognition. However, it is encountering similar concerns as other electrochemical technologies, i.e. robustness, shelf life, electrode contamination, etc.

Spectrophotometric detection basically translates the nitrite concentration information into correlated optical signals, which is usually performed in clear aqueous environment and can reach a very low detection limit. It can again be divided into fluorimetry [64] (dissolved nitrite affects fluorescence intensity), chemiluminescent detection [65], Raman/UV spectrometry [66] (using

photons to strike nitrite and measuring the scattered light), UV-vis spectrophotometry (absorption of a monochromatic light by nitrite ion), colorimetric spectrophotometry [53, 67] (combining colorimetric assays and optical measurement). Most of them are highly restricted within laboratory setting and due to the cumbersome flow-injection setup, the need for large sized pumps and spectrometers, instability of reagents and susceptibility to interfering species. Column/capillary [68] (or ion chromatography, liquid chromatography and capillary electrophoresis) techniques benefit the analysis of complex media, complements for the spectrophotometry, but are not transferrable into portable (diaper-embedded) devices at the current stage due to the strict instrumental and operational demands.

Considering the pros and cons of the available technologies, along with the goal we want to achieve (a diaper-embedded autonomous UTI sensing platform), colorimetric spectrophotometry is the most promising method. The principal reasons are: (i) colorimetric nitrite assays are robust, low cost and haven been ubiquitously used in the world; (ii) dipsticks are flexible and thin; (iii) the spectrophotometric measurement can be conducted using inexpensive commercial miniaturized photodiodes and LEDs, which has already been investigated in some microfluidic researches and adopted in company products (e.g. Marine Nitrite Ultra Low Range Checker® HC - HI764 by Hanna instruments); (iv) the operation procedure is convenient so that it can be designed easily into an autonomous fashion; (v) the matrix of dipsticks, paper, is the niche as the autonomous sensing initiator because of its porous nature enabling urine capillary flow; (vi) also, porous paper can filter insoluble substances in urine, lessening the influence on absorbance measurement.

One major limitation of colorimetric technologies is its time-sensitivity. Bacteria can multiply in urine over time, converting nitrate to nitrite. The aqueous colorimetric reagent could change color itself when exposed in the air. Water evaporates from the urine gradually, affecting the color intensity to be measured, especially for dipstick test. Most griess reagent protocols suggest read the photometric data within 30 minutes. Moreover, it is usually advisable to record the results right after 2 minutes in dipstick use instructions. These issues won't cause any significant problems in manual detection scheme, but will be troublesome in an automated sensing configuration, like the Smart Diaper from PixieScientific. Fortunately, they can be avoided with the integration of the

urine-activated battery presented in Chapter 2, since the measurement window can be fixed and controlled with the urination activity triggering the battery activation.

3.3 System Architecture and Operation

To perceive how a urine-activated battery intrinsically capture the perfect diagnosis timing without other extra urination monitoring mechanisms, Figure 3.1 previews the schematic diagram of the entire UTI screening system comprising of a paper-based Zn-Cu electrochemical power source, a nitrite detection unit (green LED/sampling strip/photodiode), and associated circuitry (a boost DC-DC converter, a low-power sensor interface, and a BLE module). The battery and sensor are fabricated on a hydrophobic wax paper substrate, with the active areas, openings, and conductive traces (copper tapes) defined by laser engraving. The ICs, LEDs, and photodiodes are soldered onto the conductive traces.

Figure 3.1 Schematic of the autonomous diaper-embedded urine-activated UTI screening system.

The device stays in a dormant state until wetted by urine, after which the on-board Zn-Cu paper battery is activated (redox reactions are enabled through moist salt bridge and two half cells), turning on the rest of the sensing system including the LED/photodiode detection unit.

Simultaneously, the test strip samples the urine for the presence of nitrite which reacts with Griess reagent and changes the white strip to pink (the complementary color to green, thus impeding the transmission of green light). The intensity of the transmitted light through the sampling strip and hence the photocurrent in the photodiode are a function of nitrite concentration. The photocurrent is subsequently converted into a pulse width modulated (PWM) waveform via the sensor interface. In the end, The BLE module digitizes the PWM data using a 40 kHz in-built counter and transmits it to the mobile device of a nearby caregiver.

In Chapter 3, we will mainly focus on the characterization and discussion of the nitrite sensing module, leaving the issues related to integrated platform to be addressed in Chapter 4

3.4 Optical Colorimetric Sensing Module

As is discussed in the prior section, there are mainly two modes of spectrophotometry: transmission and reflection, both quantitatively analyzing light absorption by colored compound in the analyte with respect to a certain wavelength. Reflectance measurement (e.g. Urisys 1100®, Roche) has a relatively higher detection limit since the reflected light usually doesn't get absorbed through the entire thickness of paper strip containing the analyte of interest. [69] Also, the larger footprint in a reflection mode layout of light emitter and detector would likely demand higher volume of sample. Therefore, a transmittance-based sensor is preferred and explored in this dissertation.

Conventionally, a bulky, weighty and costly spectrophotometer is utilized to generate an absorbance spectrum of the substances, which generally requires specialized operational skills and knowledge for interpretation of results. There have been some efforts in developing portable and miniaturized photometric analytical devices using off-the-shelf light emitting components (e.g. LEDs) and light detectors (e.g. photodiodes, phototransistors, image sensors or cameras) [52, 70, 71] at the expense of reduced monochromaticity (broader light source bandwidth) and thus reduced resolution. Most of the efforts are limited to absorbance measurement in channels of glass-, silicon- or polymer- (such as PDMS (polydimethylsiloxane) and PMMA (polymethyl methacrylate)) based microfluidic devices for in-laboratory flow injection analysis (FIA), which typically involves external active pumping of liquid analytes. In some work [72], passive fluid transporting means

relying on capillary penetration is introduced to guide analyte liquid to the colorimetric/photometric detection zone, enabling automated diagnostics. However, most of the diagnostic platforms are in rigid substrate, not suitable for lightweight wearable applications. Hence, we may want to examine a paper-based microfluidic platform as our desired photometric sensor medium where porous paper can also function as the matrix for dry assay reagents. There exist few studies into the transmittance-based absorption through paper-based colorimetric assays. One pioneering attempt in this direction is from Whitesides group [69], in which optical model of filter paper is discussed and protein assay light transmission is characterized using a customized hand-held optical colorimeter as a proof of concept. Yet, there are a few defects of this device, limiting its application: (i) capillary property of filter paper is not exploited to automate the assay; (ii) tedious and complicated procedures of running the assay, drying the assay paper and rewetting it with refractive index-matching oil and inserting into the colorimeter are unfriendly to general users; (iii) the device is still oversized and far from wearable. Therefore, my dissertation is devoted to putting forward a fully-autonomous (only one step of providing the liquid analyte is needed, in the diaper scenario by urination) flexible platform, with which light absorption data throughout the measurement period (before and after the reaction) is collected for noise reduction, and no separate control zone or index-matching oil (in Whiteside group work) is necessary.

For fulfilling this purpose, the structure of the colorimetric optical nitrite detection module is demonstrated in Figure 3.2, with all the components integrated onto the hydrophobic wax paper substrate (the same substrate also incorporates the battery, not shown in the schematic). The wax paper substrate and a conformable dressing tape (60 μm, OpSite Flexifix, Smith & Nephew) are patterned using the CO_2 laser (the latter is used for covering and passivation). Both the wax paper and the tape incorporate holes for light transmission and alignment. Conductive traces (copper tapes) are defined using the fiber laser, providing electrical connection and soldering joints for the green LED (572 nm, LG L29K-G2J1-24-Z, Osram) and photodiodes (540 nm, TEMD5510FX01, Vishay). For final assembly, the paper substrate, metallic layer, and covering tape are laminated. Prior to use, the substrate is folded along the dash line with the aid of alignment holes (Figure 3.2a) such that the LED and the active photodiode overlap and align.
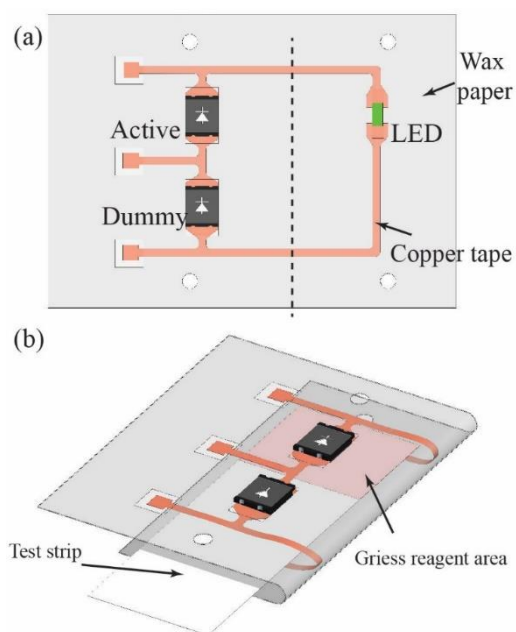
Figure 3.2 Nitrite sensing schematic. (a) Top view of the device in the unfolded configuration. (b) Perspective view of the device in the folded (in use) shape.

Before folding, a sampling strip containing the "Griess reagent", e.g. p-arsanilic acid and N-ethylenediamine dihydrochloride (N.E.D.), is intercalated in between the LED and photodiode (Figure 3.2b). The reagent strip can be fabricated by soaking a filter paper into a methanol solution of p-arsanilic acid and N.E.D. (200 mg: 40 mg in 20 mL), followed by drying and trimming into proper sizes. There are also many other choices for Griess reagent [19], for example, a mixture solution of 50 mM sulfanilamide, 10 mM N.E.D. and 330 mM citric acid in methanol [18]. Additionally, the strip is enclosed by dressing tape to be isolated from electronic components and meanwhile to prevent overflow (unrestricted flow out of the strip), evaporation and contamination, Figure 3.3. A very tiny pinhole ($< \varnothing$ 0.5 mm) might be opened at the end of reagent zone for ventilation and thus facilitating fluid flow in the packaged strip,
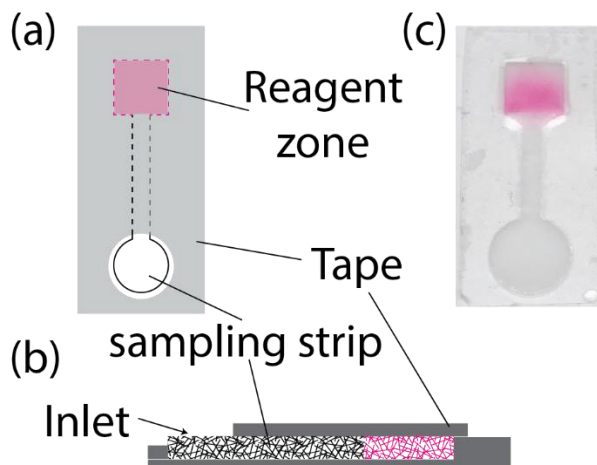
Figure 3.3 Packaged reagent strip: schematic of (a) top view and (b) cross section; (c) photograph of a packaged strip after nitrite assay

The urinary nitrite diazotizes p-arsanilic acid to couple with N.E.D. and form a pink azo dye, intensity of which is a function of nitrite concentration. The green light emitted from the LED is absorbed by the colored strip matrix, lowering the photocurrent in the photodiode. As shown in Figure 3.2, two photodiodes are used, one of which is active (exposed to the reaction region) while the other acts as a reference (not exposed to the light). The reference photodiode contributes to the charging capacitance required for PWM operation while simultaneously compensates the potential leakage current of the active one, thus suppressing the noise and enhancing the performance.

3.5 Optical Model and Characterization of Sampling and Test Strip

The choice of the sampling strip substrate (Figure 3.3) containing the Griess reagent is one of the important factors affecting the sensitivity and detection limit of the system. The substrate needs to be hygroscopic to wick the urine to the reaction zone between the photodiode/LED pair. Simultaneously, it should be as uniform as possible such that it introduces the least process variations. In addition, the substrate should be colorless or white to prevent unnecessary interference. The most commonly used porous cellulose paper (e.g. filter paper) seems to be a competitive candidate. Since the porous substrate is also supposed to be the region where Griess reaction and light absorption measurement takes place, a bit more thought should be added in this aspect.

Spectrophotometric quantification of the concentration of colored compound (nitrite-induced red pink dye in our case) has been extensively adopted and studied. Its mechanism is primarily that the amount of light absorption through the sample is corrected to the dye concentration and the correlation relationship can be calibrated and reproducible. Usually, the sample under test is a colored clear solution or liquid, while in our case it soaks porous paper substrate, which imposes light scattering and alters the eventual measured light signal. Therefore, we need to establish the optical model of the filter paper-based test strip to quantitatively analyze light absorption therein.

3.5.1 Reflection loss

First, when light enters the cellulose paper substrate, reflection occurs and leads to some loss of the light intensity. The transmittance (the ratio of transmitted power) at the interface between two media of different refractive indices (n_1 and n_2) is given by [73]

$$\begin{cases} T_{\perp} = \dfrac{\sin 2\theta_1 \sin 2\theta_2}{\sin^2(\theta_1 + \theta_2)} \\[2ex] T_{\parallel} = \dfrac{\sin 2\theta_1 \sin 2\theta_2}{\sin^2(\theta_1 + \theta_2)\cos^2(\theta_1 - \theta_2)} \end{cases}, \tag{3-1}$$

where $T_{\perp}$ and $T_{\parallel}$ are for the cases of TE (transverse electric, i.e. its electric field being normal to the plane of incidence) polarized light and TM (transverse magnetic) polarized light, and θ_1 and θ_2 are the notations of incident angle and refractive angle respectively, as in Figure 3.4. They obey Snell's Law as

$$n_1 \sin \theta_1 = n_2 \sin \theta_2, \tag{3-2}$$

where n_1 and n_2 are the indices of refraction of the two media.
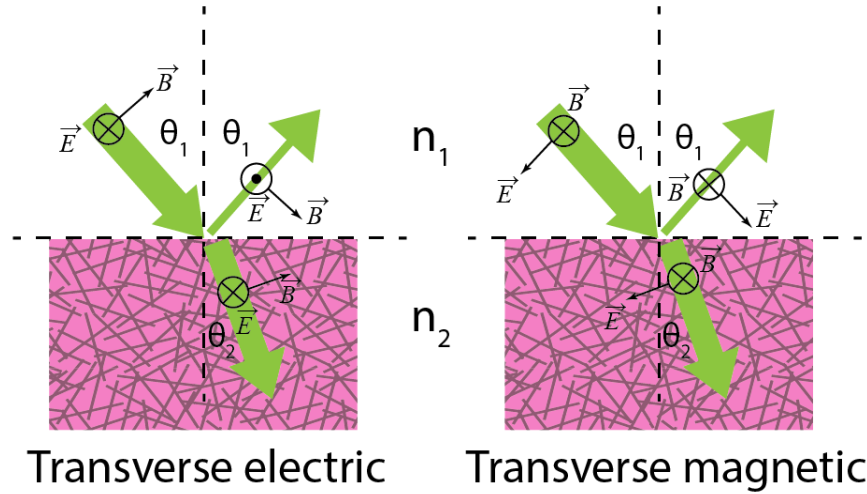
Figure 3.4 Transmission/reflection of light on the interface of two media, with respect to transverse electric and transverse magnetic field orientations of the light

To simplify the model, assume that incident light is perpendicular and then (3-1) becomes a degenerate form

$$T = T_{\parallel} = T_{\perp} = \frac{4n_1 n_2}{(n_1 + n_2)^2}, \tag{3-3}$$

where $T_{\perp}$ and $T_{\parallel}$ are the same since the TE and TM light beams are not distinguishable in this scenario. It is obvious from (3-3) that when the degree of mismatch between n_1 and n_2 increases, the reflection loss will be higher (smaller T).

Considering that the paper is not a homogeneous medium and the influence from the filling material (air in dry state, urine or water in wet state) should be included, its effective refractive index [74] can be estimated as

$$n_2 = \sqrt{\phi n_{cellulose}^2 + (1-\phi) n_{(air \rightarrow water)}^2}, \tag{3-4}$$

where the index of refraction of cellulose $n_{cellulose}$ is 1.53~1.62 [75], that of air is about 1, that of water is 1.333 and ϕ is the volume fraction of cellulose fibre in paper. It indicates that the transmittance changes with the hydration state (dry versus wet) of filter paper and local variation of volume fraction ϕ will contribute to the measurement noise. n_1 is the refractive index of air for unpackaged filter paper or of dressing tape if the reagent strip is packaged. The simulated lumped

transmittance according to (3-3) and (3-4) with reflection on both surfaces is plotted in Figure 3.5 with respect to ϕ varying from 0 to 1, where $n_{cellulose}$ is selected as 1.58. Meanwhile, the simulation results for dressing-tape-packaged filter paper considering the additional external reflection on air-tape interface is also included, where the index of refraction of dressing tape material, polyurethane, is chosen as 1.86 [76].
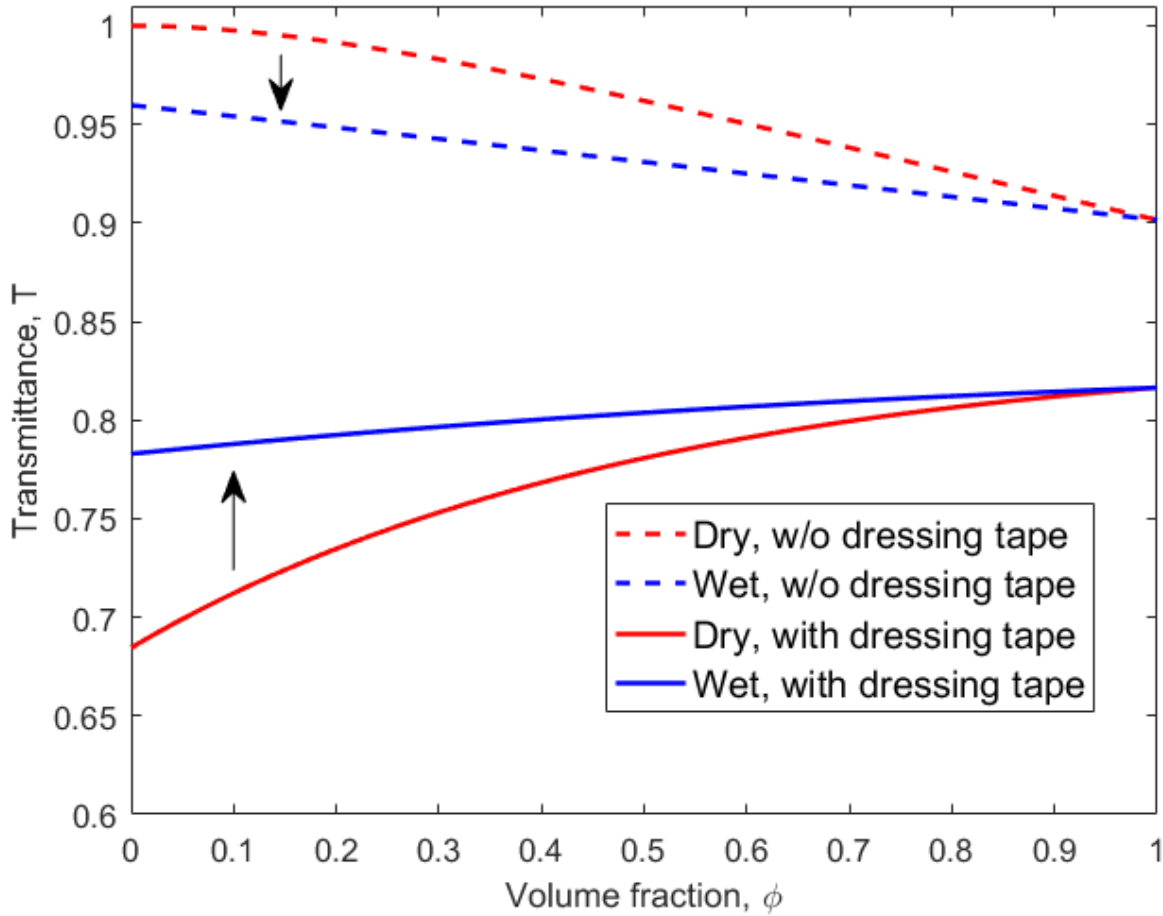
Figure 3.5 Transmittance simulation for paper in dry/wet states and with/without packaging tape

From the results in Figure 3.5, we can tell that a larger ϕ (more cellulose in filter paper) renders less disparity in transmittance between dry and wet states, regardless of dressing tape encapsulation. However, it is colorimetric nitrite assay related liquid filling the cellulose network not cellulose itself that is contributing to the desired signal, so a larger ϕ might not be wanted. Tape packaging indeed brings higher reflection loss (Figure 3.5) and relative transmittance change $\frac{T_{Wet}}{T_{Dry}}$ between dry and wet states (Figure 3.6), thus making transmitted light through filter paper

more sensitive to local ϕ variation, but the dressing tape is still kept since it provides better control over the light path length in the dyed liquid soaking the filter paper, as well as isolation of analyte from other components in the system.
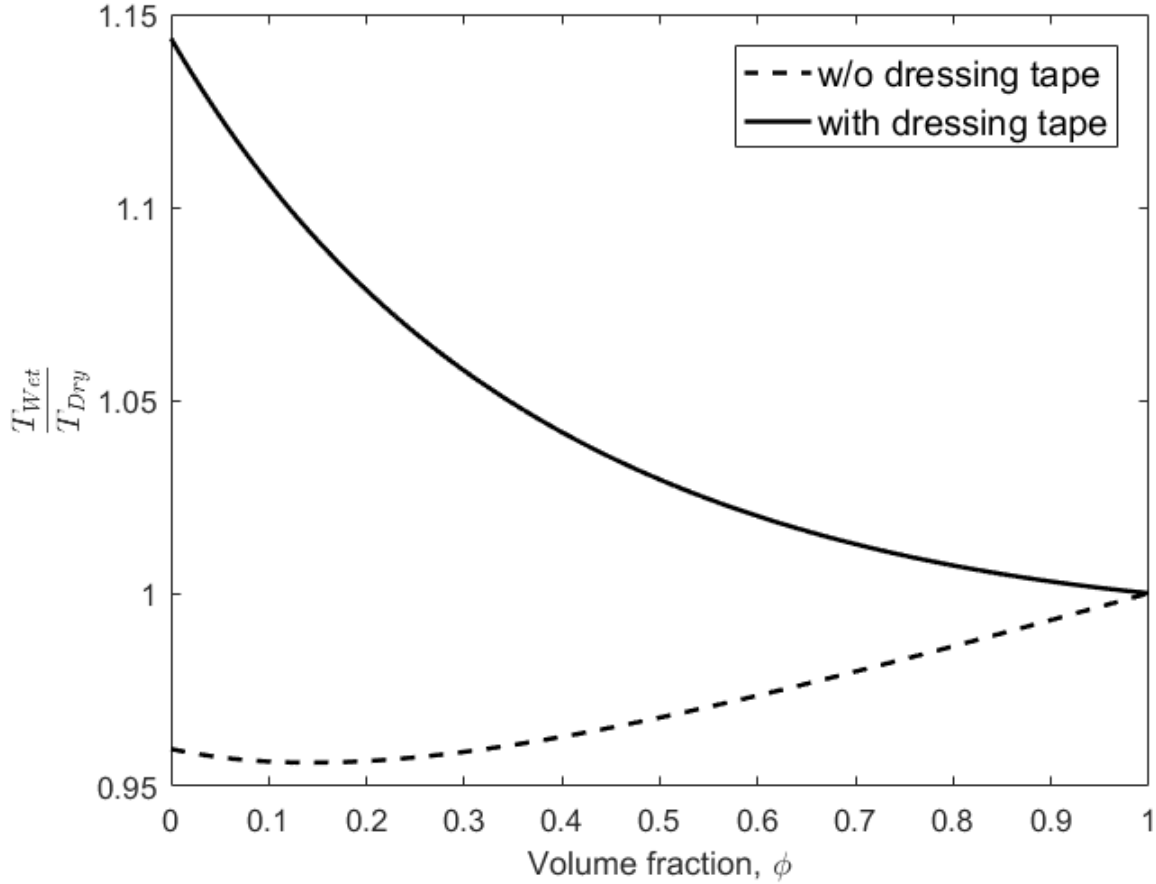
Figure 3.6 Relative transmittance versus volume fraction for with and without tape packaging

3.5.2 Absorption through cellulose paper

The propagation of light through paper is subject to attenuation caused by absorption of the dye (produced in the colorimetric nitrite assay) and scattering of the cellulose network, as shown in Figure 3.7. It can be described by Beer-lambert Law [77]:

$$I_{out} = I_{in} 10^{-\alpha_{scatter} z} 10^{-\varepsilon c z_{liquid}}, \tag{3-5}$$

where I_{out} and I_{in} stand for the irradiances (radiant power per unit area, sometimes named intensity) of light entering and leaving the dyed urine-filter paper network, $\alpha_{scatter}$ is the attenuation coefficient incurred by paper scattering and absorption, z is paper matrix thickness, ε is molar

absorptivity, c is dye concentration and z_{liquid} is thickness of dyed solution. Ideally (for fully wet packaged paper without trapped air bubbles), $z = z_{liquid}$. It is then obvious that, the term $10^{-\varepsilon c z_{liquid}}$ is ascribed to dye absorption.
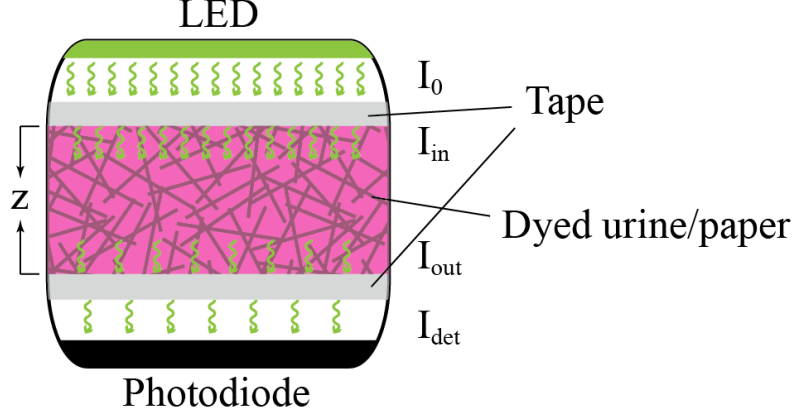
Figure 3.7 Illustration of light irradiance change in a packaged strip after assay

Overall, the detected light signal incorporating interfacial reflection loss and attenuation loss is

$$I_{det} = I_0 T_{lumped} 10^{-\alpha_{scatter} z} 10^{-\varepsilon c z_{liquid}} , \tag{3-6}$$

where I_{det} and I_0 are the irradiances of light detected by the photodiode and emitted from the LED respectively. Meanwhile, T_{lumped} represents the superimposed transmittance including all the air/tape and tape/paper interfaces.

Then, detected optical signal is converted to photocurrent in the diode by

$$i_P = R_\lambda A I_{det} = R_\lambda A I_0 T_{lumped} 10^{-\alpha_{scatter} z} 10^{-\varepsilon c z_{liquid}} , \tag{3-7}$$

where R_λ is responsivity (conversion effectiveness of radiant power into electrical current) of the photodiode, and A is the light-sensitive area of the photodiode.

3.5.3 Signal normalization

From Equation (3-7), it seems enough to figure out a method of extracting the photocurrent signal. However, we need to keep in mind that this diaper-embedded sensor is intended for one-time use considering the embedding location and the irreversibility of Griess reaction. Correspondingly, process variations in LED brightness (I_0, ±11% for the selected LED), photodiode responsivity

(R_λ), effective area (A, also affected by assembly variations), filter paper thickness (z), its equivalent scattering coefficient ($\alpha_{scatter}$) and so on, will introduce sample-dependent interference with the urine nitrite induced signal, making it indistinguishable at low levels.

In a prior publication [78], Seo *et. al.* proposed an on-line sensor normalization method where a differential measurement between for dry reagent strip and for wet reagent strip (after reaction with urine analyte) is normalized as

$$PW_{diff,norm} = \frac{PW_{dry,ref}}{PW_{dry}}(PW_{dry} - PW_{wet}) = PW_{dry,ref}(1 - \frac{PW_{wet}}{PW_{dry}}), \quad (3\text{-}8)$$

where $PW_{dry,ref}$ is a constant, and PW_{dry} and PW_{wet} are pulse width readings converted from the photocurrent sensed for dry reagent strip and for wet reagent strip respectively. The relationship between pulse width and photocurrent will be briefly summarized in the following section (3.6). This is an effective way of mitigating the interference from process variations, but theoretical proof is missing to explain why it works well. Therefore, starting from Equation (3-7), I want to derive an analytical form for the normalized signal, in which dry strip measurement serves as the sample-dependent offset in the same manner as in Equation (3-8).
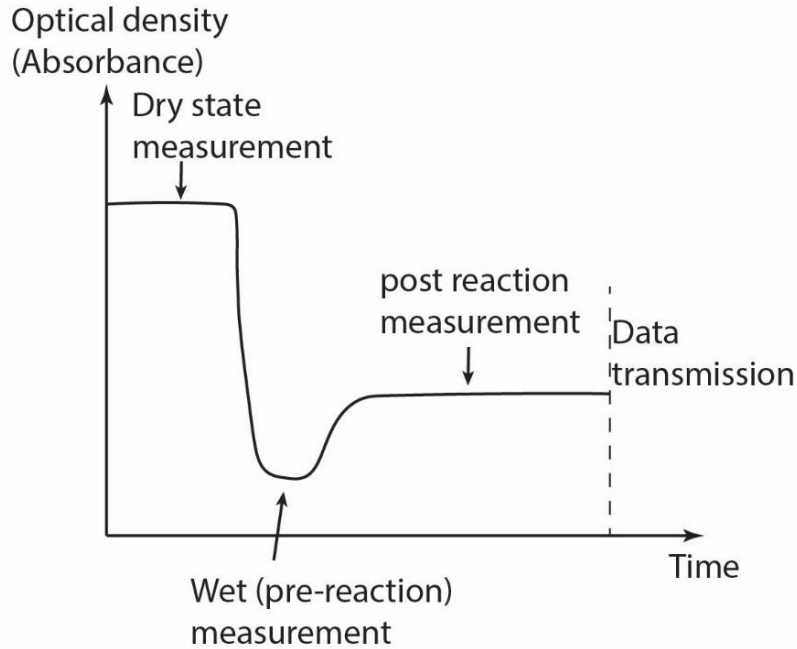
Figure 3.8 Dynamics of measurement signal

The trend of light absorption in the detection region can be illustrated in Figure 3.8. At the beginning, the detection region is dry and there is no dye absorption contributing to light irradiance loss, but the paper cellulose matrix scattering is more intense due to larger refractive index mismatch between air and cellulose matrix since scattering can be viewed as a series of reflection incidences [69] on air-cellulose boundaries until the light beam traverses the paper and gets captured eventually by the photodiode. In this stage, we can get dry-state photocurrent measurement as

$$i_{P,\,\text{DRY}} = R_\lambda A I_0 T_{lumped,\,\text{DRY}} 10^{-\alpha_{scatter,\,\text{DRY}}z}, \tag{3-9}$$

where $T_{lumped,DRY}$ and $\alpha_{scatter,DRY}$ are the transmittance and paper attenuation coefficient as in Equation (3-7) but when the detection region is dry. As urine analyte reaches the detection region, the refractive index mismatch between urine and cellulose get smaller and thus more light get transmitted through region strip, so we will see an abrupt drop of the light absorption (or absorbance), even though urine itself absorbs light to some degree. As Griess reaction proceeds over the detection region of the reagent strip, pink color dye forms and contributes to light absorption, gradually approaching a plateau[3], from which we can get wet-state measurement as

$$i_{P,\,\text{WET}} = R_\lambda A I_0 T_{lumped,\,\text{WET}} 10^{-\alpha_{scatter,\,\text{WET}}z} 10^{-\varepsilon c z_{liquid}}. \tag{3-10}$$

Hence, we can get a normalized signal by taking the ratio 3-11of wet-state and dry-state measurements,

$$\frac{i_{P,\,\text{WET}}}{i_{P,\,\text{DRY}}} = \frac{T_{lumped,\,\text{WET}}}{T_{lumped,\,\text{DRY}}} 10^{-(\alpha_{scatter,\,\text{WET}} - \alpha_{scatter,\,\text{DRY}})z} 10^{-\varepsilon c z_{liquid}}. \tag{3-11}$$

In this way, we eliminate R_λ, A and I_0, which significantly relieve (ideally rule out) interferences from photodiode, LED and assembly process variations. Given that the differences on T_{lumped} and $\alpha_{scatter}$ between dry state and wet state are mainly determined by refractive indices change from air to urine, rather than by urine nitrite concentration c, therefore for each individual sensor, we can approximately take the terms on the left of $10^{-\varepsilon c z_{liquid}}$ as a constant coefficient, such that we

---

[3] The U-shape valley before the plateau in Figure 3.8 is not a general case. Whether a local minimum will be witnessed is affected by urine nitrite concentration, strip thickness and reaction rate.

only need to take photocurrent measurement both when the detection region is dry and when the reaction levels off.

There is obviously another method of normalizing the signal by adding a control region without Griess reagent along with a control photodiode/LED pair, which has been proposed by Whitesides group in their protein sensor [69]. Similarly, we can get the control wet-state measurement, and normalize the signal as

$$\frac{i_{P,\,\text{WET}}}{i_{P,WET}^{control}} = \frac{R_\lambda A I_0 T_{lumped,\,\text{WET}} 10^{-\alpha_{scatter,\,\text{WET}} z}}{R_\lambda^{control} A^{control} I_0^{control} T_{lumped,\,\text{WET}}^{control} 10^{-\alpha_{scatter,\,\text{WET}}^{control} z^{control}}} 10^{-\varepsilon c z_{liquid}}. \qquad (3\text{-}12)$$

It is believed to significantly diminish variations in T_{lumped} and $\alpha_{scatter}$ added by urine sample properties (color, cloudiness, composition like nitrite concentration), which has not been coped with in Formula (3-11), at the cost of extra photometric components and a larger footprint. However, it brings back the sensor-dependent variations in R_λ, A and I_0, which experimentally seemed to be a major source of interference (discussed in the following sections). To resolve this issue, dry measurement of the control region is also needed, so the normalized signal will be

$$\frac{\dfrac{i_{P,\,\text{WET}}}{i_{P,\,\text{DRY}}}}{\dfrac{i_{P,\,\text{WET}}^{control}}{i_{P,\,\text{DRY}}^{control}}} = \frac{T_{lumped,\,\text{WET}} T_{lumped,\,\text{DRY}}^{control} 10^{-(\alpha_{scatter,\,\text{WET}} - \alpha_{scatter,\,\text{DRY}}) z}}{T_{lumped,\,\text{DRY}} T_{lumped,\,\text{WET}}^{control} 10^{-(\alpha_{scatter,\,\text{WET}}^{control} - \alpha_{scatter,\,\text{DRY}}^{control}) z^{control}}} 10^{-\varepsilon c z_{liquid}}. \qquad (3\text{-}13)$$

That would provide better precision over the normalization method in Formula (3-11) which however simplifies the sensor architecture design and still achieves sufficient precision for our UTI screening application. Thus, I will be focusing on presenting the results and discussion pertaining to one photodiode/LED pair for detection region only, which can be extended to incorporate control region for higher precision and detection regions tailored for other biomarkers.

3.5.4 Absorbance characterization results

Figure 3.9 shows the absorption spectra (400-700 nm, Molecular Devices VersaMax Microplate Reader) of test strips (disks made from Grade 1 filter paper, 6 mm diameter) loaded with the Griess

reagent and 3 µL NaNO₂ solutions in various nitrite concentrations. As can be seen, the absorption peak for the pink azo is around 545 nm and increases at higher nitrite levels. This spectrum validates the use of green LED (peak at 572 nm) and photodiode (peak at 540 nm) to provide the highest sensitivity. (As to why absorbance-based measurement is preferred at peak wavelength, refer to [79].)
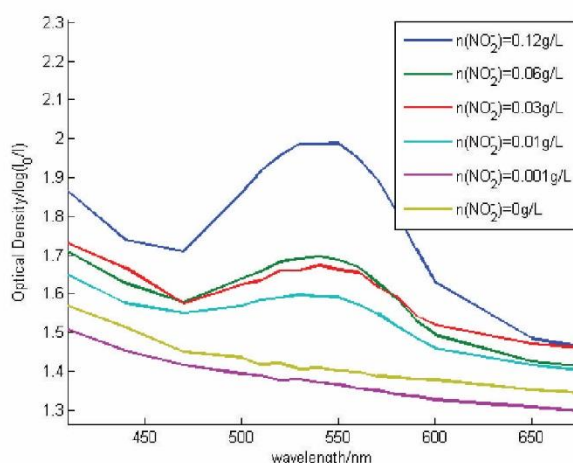
Figure 3.9 Absorption spectrum of a 180 µm thick filter paper with Griess reagent exposed to different concentrations of nitrite solutions.

Apparently in Figure 3.9, there exist strip sample-dependent offsets in absorbance. For example, the measured absorbance for $c(NO_2^-) = 0g/L$ is bigger than that for $c(NO_2^-) = 0.001g/L$. Additionally, the experimental procedure also adds errors because the solutions are dropped into the wells one at a time and the Microplate Reader can only do end-point measurements instead of sweeping the spectrum, which prolongs the process and causes offsets from sample to sample and from wavelength to wavelength (water evaporation and pigment instability). That being said, the process variations in reagent strips can still be evaluated by microplate reader measurements, which is also a proof-of-concept experiment for the absorbance-based sensor.

First, the process variations in absorbance when filter paper is in dry state, are characterized, with the results presented in Figure 3.10. Three different types of filter papers are investigated, and their relevant specifications are tabulated in Table 3.1. (Grade 113 filter paper is not investigated into due to its creped surface.) Noticeably, thicker paper has higher absorbance, and all types of papers

have a bump around 500 nm in their absorbance spectra, which may be related to the molecular structure of filter paper composition material (cellulose principally).
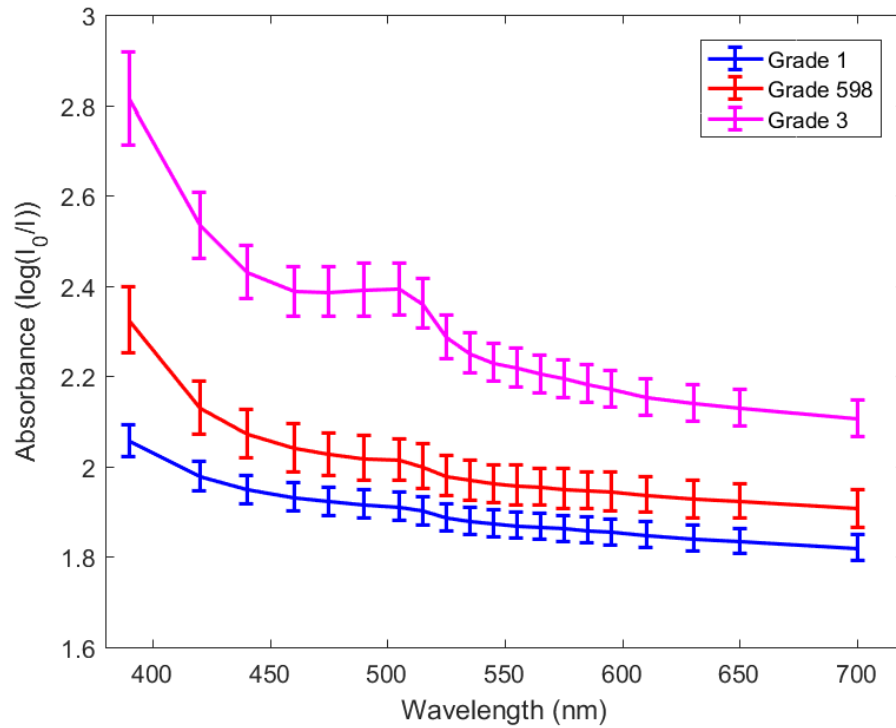
Figure 3.10 Dry paper absorption spectrum

Table 3.1 Typical properties of filter papers

Grade #	Thickness (μm) [80]	Particle retention (μm) [81]	Water flow rate (ml/min) [80]	Absorbance log(I_0/I) at 545nm
1	180	11	57	1.8222±0.0288
113	420	30	774	N/A
598	320	8-10	medium to fast [81]	1.9109±0.0414
3	390	6	28	2.1791±0.0425

Recall that

$$i_{P,\,\mathrm{DRY}} = R_\lambda A I_0 T_{lumped,\,\mathrm{DRY}} 10^{-\alpha_{scatter,\,\mathrm{DRY}} z}. \tag{3-9}$$

The absorbance measurement results represent the magnitude of $\log(T_{lumped,DRY} 10^{-\alpha_{scatter,DRY} z})$, as in Table 3.1 (the blank plate absorption at 545 nm, 0.0515±0.0051, has been subtracted). Here

$T_{lumped,DRY}$ is for the situation without dressing tape packaging. The standard deviation (SD) of the absorbance reflects the inhomogeneities in the filter papers.
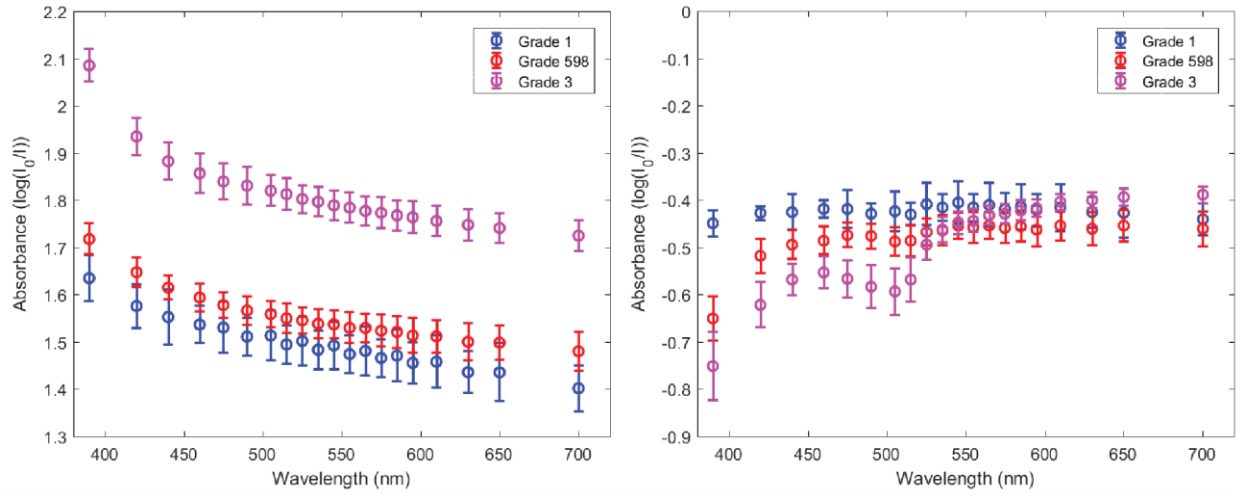
Figure 3.11 Wet paper absorption spectrum for $c(NO_2^-)=0$ without (left panel) and with (right panel) dry measurement normalization

Accordingly, absorbance of the reagent strip in wet state without nitrite, $c(NO_2^-)=0$, is also measured, and the results are illustrated in Figure 3.11. To compare among filter papers in different thickness, 20 μL instead of 3 μL water is added to soak the entire paper disk. The plot on the left panel represents the signal described as

$$i_{P, \text{WET}}\big|_{c=0mg/l} = R_\lambda A I_0 T_{lumped, \text{WET}} 10^{-\alpha_{scatter, \text{WET}} z},$$ (3-14)

while the plot on the right panel is for the ratio of (3-14) and (3-9), or equivalently the coefficient term irrespective of nitrite concentration in (3-11). An obvious change between the two plots in Figure 3.11, is that the absorbance difference among three different types of filter papers is smaller in the normalized signals. What is more, the SDs (at 545 nm) for all filter paper gauges are slightly improved from 0.0506 (Grade 1), 0.0289 (Grade 598), 0.0304 (Grade 3) to 0.0458, 0.0281, 0.0242, reducing the influence of the variations in $T_{lumped,WET}$ and $\alpha_{scatter,WET}$.

Similarly, the normalized absorbance data is obtained at various nitrite concentrations (0, 0.5 mg/L, 1 mg/L and 5 mg/L), to verify the absorbance-based sensing mechanism within the range of interest (0-5 mg/L). The results are plotted in Figure 3.12, in which normalized signals are drawn

in solid lines while the unnormalized wet-state measurement data are painted in dashed lines. In all three graphs, the characteristic curves are translated such that the Y-axis value is 0 at 0 nitrite concertation, for the ease of comparison. From the results, we can tell that I_{DRY} normalization compensates sample-dependent absorption offset from paper scattering, accomplishing lower detection limit [4] and 3~10% less SDs (on average). There exists deterioration at some concentrations, partially aroused by experimental defeats (like long process induced uneven signal shift), implying that the relative changes between $T_{lumped,DRY}$, $\alpha_{scatter,DRY}$ and $T_{lumped,WET}$, $\alpha_{scatter,WET}$ are not constants and may still vary among strips made from even the same piece of filter paper. Another observation is that thicker paper provides better performance in terms of limit of detection: 3 mg/L for Grade 1 paper while 1.3 mg/L for Grade 3 paper, which is consistent with (3-11).
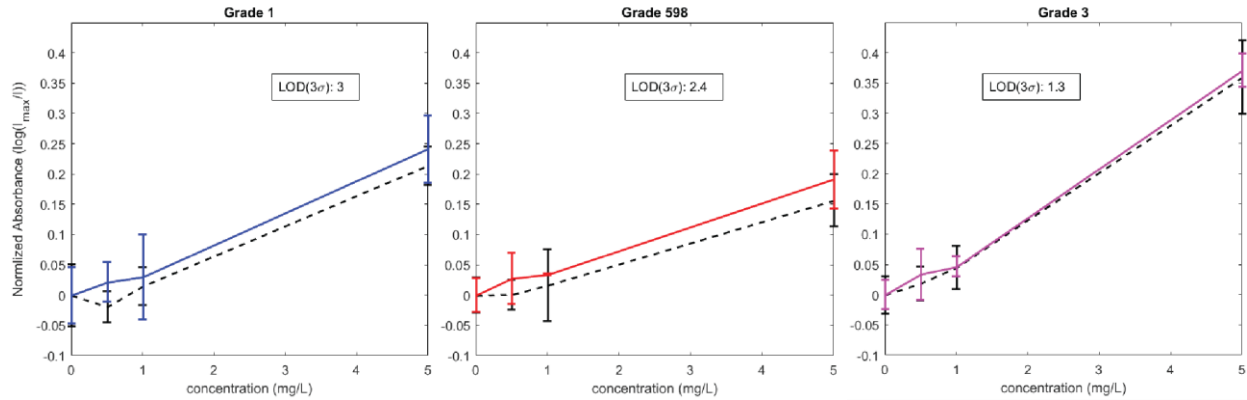
Figure 3.12 Normalized absorbance vs. nitrite concentration calibration curves for Grade 1, 598, 3 filter papers. In all three subplots, solid line stands for $\log(I_{DRY}/I_{WET})$, and dashed line stands for $\log(I_0/I_{WET})$, where I_0 is the blank plate reading of the microplate reader.

Taking into account the experimental defeats mentioned above, it still seems to be very promising to use the absorbance-through-paper method for approaching the practical urinary nitrite detection limit 0.5 mg/L (identical to 0.5 ppm). It will be revealed in the following sections that the nitrite detection limit could be further confirmed at <0.6 mg/L in a sensing module excluding the experimental defeats related to the Microplate Reader measurement. It will also be seen how the

[4] The coincident elevation of the slopes for all grades in Figure 3.12 should be ascribed to the limited sample set (only 4~5 samples are examined for each condition), considering that in no way could dry-state measurement produce a nitrite concentration related signal.

electronic component process variations (R_λ, A and I_0) can be effectively and remarkably compensated for, which is not a major hindering factor in the Microplate Reader (better monochromaticity and consistent photodetector performance) instead.
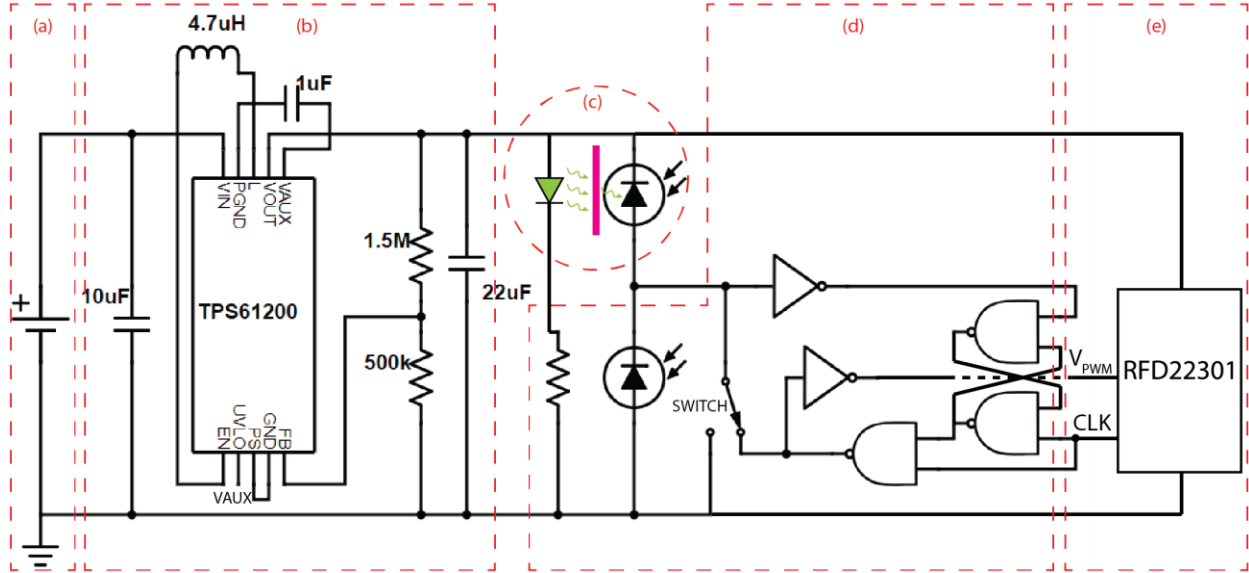
Figure 3.13 Block diagram of interface circuitry for nitrite sensing platform. (a) Urine-activated battery; (b) DC-DC voltage regulator; (c) colorimetric nitrite sensor; (d) sensor interface with PWM modulation; (e) BLE module.

3.6 Interface Circuitry

Seo *et. al.* [78] introduced a power efficient yet accurate sensor interface using PWM operation and a wireless transmitter via a Bluetooth low energy (BLE) module as shown in Figure 3.13. For the PWM operation, two photodiodes are connected in series and the parasitic capacitors of the two photodiodes serve as charging capacitors. The dummy photodiode at the bottom, which is sheltered in the sensor module, not only contributes to the charging capacitance (~1 nF), but also compensates for the dark current[5] of the active (for sensing the detection region) one. Because the dark current of a photodiode is insensitive to its bias voltage, the two photodiodes almost have identical dark currents and thus the output node, V_O, is less affected by the balanced dark current. The dummy (or reference) photodiode can go along with other electronic components as a reusable module, while the sensing photodiode/strip/LED should work as a disposable unit. The SR latch based PWM circuit converts the V_O to a series of pulses, the width of which is inversely

---

[5] The total current in a photodiode is the sum of its dark current and photocurrent.

proportional to the photocurrent in the active photodiode (assuming its dark current is canceled out by the reference diode).

$$T_{Pulse\ Width} = \frac{\beta}{i_P}.$$

(3-15)

Derivation of this proportional relationship is elaborated in [78]. If we combine (3-11) and (3-15) to eliminate i_P, we can see that (3-8) and (3-11) are equivalent with a few transformations. As of now, the theoretical proof for why Formula (3-8) works well has concluded. Then, the PWM signal is digitized by the BLE module using its 40 kHz built-in counter and transmitted to a nearby BLE capable mobile device. This scheme does not require an ADC, significantly improving the power efficiency and reducing the complexity of the system.

Apart from the interface circuits for the sensor output signal, a DC-DC boost converter (TPS61200 from TI, power conversion efficiency between 50% and 60%, line and load regulations are both 0.1%-Typ. and 0.5%-Max.) boosts and regulates the supply voltage of the urine-activated Zn-Cu paper battery from 1 V to 2 V and provides 0.5 mA biasing current for the green LED, 0.08 mA for the PWM sensor interface, and 6 mA for the BLE module in the transmission mode. This power management circuit is indispensable for feeding a stable current to the LED and a constant biasing voltage to the photodiode, since the output of paper battery declines and fluctuates severely within a relatively short term as opposed to commercial batteries. To reliably satisfy the power requirement, the size of the paper battery is optimized at 3.2 cm × 2.2 cm (Section 4.1.2).

3.7 Sensor Calibration

3.7.1 Process variability

Here I want to revisit the formula for the normalized signal for the sensor module and discuss sources of process variations and noises:

$$\frac{i_{P,\ \text{WET}}}{i_{P,\ \text{DRY}}} = \frac{T_{lumped,\ \text{WET}}}{T_{lumped,\ \text{DRY}}} 10^{-(\alpha_{scatter,\ \text{WET}} - \alpha_{scatter,\ \text{DRY}})z} 10^{-\varepsilon c z_{liquid}}.$$

(3-11)

Any sources of process variations or noises that might alter the parameters in Formula (3-11) will cause variation of the collected pulse width data. The following items should be the main responsible process variations:

(a) Inhomogeneities in the paper strip, affecting $T_{lumped}, \alpha_{scatter,} z \ (or \ z_{liquid})$.

(b) Chemical reaction kinetics, manifesting as spatially varying and time-dependent dye concentration, c(x, y, z, t).

(c) Residual air trapped in the paper not filled by liquid, affecting $\alpha_{scatter}, z_{liquid}$.

(d) LED/strip/photodiode alignment. LED is a point not collimated light source, so light beams in different directions will experience different reflection loss and absorption depths before reaching the photodiode. This will eventually result in non-linear deviation from the Beer-Lambert relationship [79], and we may use an effective z and add a constant in the exponential term in (3-11) to represent the lump sum for a fixed alignment and dye concentration even though the deviation of absorbance versus dye concentration still holds. Then, no wonder will the effective z be altered by the alignment/orientation of sensor components.

(e) Ambient light and stray light interference, which may add light beams that may or may not go through the detection region. It should be prevented as much as possible in sensor architecture design and packaging.

(f) Process variations and thermal noises in electronic components, such as dark current mismatch, threshold voltage variation of gates and so on. A detailed report on noises in electronics was presented in [78].

3.7.2 Deviation from Beer-Lambert Law, detection range and limit of detection

Besides the process variations discussed previously and thermal noises that will cause deviation from the ideally linear absorbance-analyte concentration relationship, Beer-Lambert Law itself has limitations on its application of relating optical constants (such as the attenuation constant) of materials to the light transmission measurement by the said formula (3-7).

First, a LED is a polychromatic light source with a continuous spectrum, so is the pink azo dye absorptivity. In this case, Beer-Lambert Law no longer strictly holds and deviation from the ideal linear relationship between absorbance and dye concentration may be magnified with a rigorously

varying dye absorptivity spectrum given a polychromatic light source [53, 79]. Including other elements that are contingent on the wavelength of radiation, formula (3-7) can be modified to integrate the photocurrent per unit wavelength over the relevant spectrum:

$$i_P = A \int_0^\infty R(\lambda) I_0(\lambda) T_{lumped}(\lambda) 10^{-\alpha_{scatter}(\lambda)z} 10^{-\varepsilon(\lambda)cz_{liquid}} \, d\lambda. \qquad (3\text{-}16)$$

Second, when the dye concentration exceeds a certain level, the solute molecules begin to interact with their neighboring molecules and thus no longer independently contribute to light absorption, which is the premise of Beer's Law. According to [79], 0.01 M is usually taken as the analyte concentration boundary for the independency assumption to break down, which, however in a porous paper matrix, might be much lower.

In addition, dye concentration would also alter the index of refraction of the liquid, which apparently affects light transmittances on the interfaces and thus scattering in the paper. In fact, the refractive index also changes the absorbance though not to a significant extent. Exact solution of light propagation explicitly incorporating the influence of refractive index need to be based on Maxwell's equations and consider interference effects from multiple reflections at interfaces [82].

So far, we can see that as the urine nitrite concentration goes up, $i_{P,\,WET}$ decreases by $10^{-\varepsilon cz_{liquid}}$ until it is limited by noise current or beyond linear range of Beer-Lambert Law, which sets the upper limit of the detection range of the sensor .

On the other hand, when the nitrite concentration approaches zero (negative sample), $i_{P,\,WET}|_{c=0}$ is the brightest irradiance level detected by the photodiode (typically, $i_{P,\,WET}|_{c=0} > i_{P,\,DRY}$). Since the photocurrent is reciprocally converted to pulse width as in equation (3-15), the same amount of photocurrent change at the lower nitrite level would be smaller, and the detectable change is determined either noise current or digitization accuracy limited by the 40 kHz in-built counter. Therefore, the interface circuit is designed such that $i_{P,\,WET}|_{c=0}$ and $i_{P,\,DRY}$ are in proper operation range of both the photodiode and the digitizer. The limit of detection of the sensor is then when $\Delta i_{P,\,WET}|_{c=0}^{c=LOD}$ is comparable to baseline noise, process variation and digitizing accuracy, whichever is the worst.

3.7.3 Sensor calibration and characteristic curve

The sensor calibration[6] setup is illustrated in Figure 3.14. A sensor (as in Figure 3.2, 3.2 cm $\times$ ~4 cm folded in use) is connected to a PCB module (Figure 3.14b) housing all the other circuit components (DC-DC converter, sensor interface and BLE transmitter) and shielded in a black box (and/or protected with black vinyl tape, Figure 3.14c), protected from ambient light interference. A mobile device (tablet or phone, Figure 3.14a) is paired via BLE link, displaying the real-time measurement results. After each measurement cycle, dry-state (pulse width) measurement PW_{dry}, and wet-state measurement PW_{wet}, are extracted from the recorded data in the mobile device.
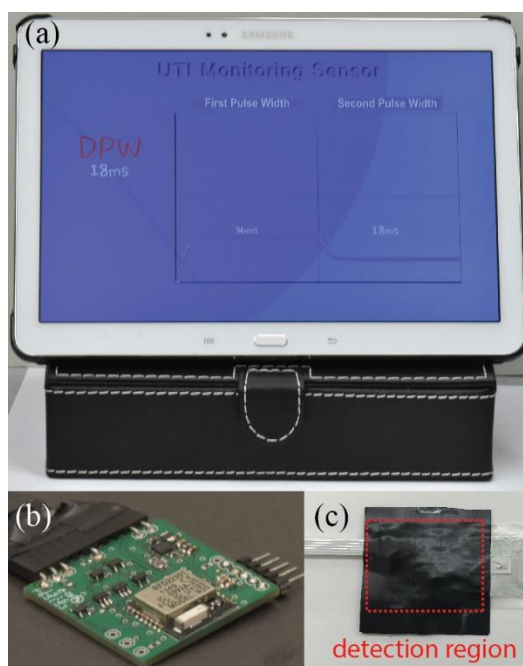
Figure 3.14 (a) Mobile app displaying measurement results real-time. (b) PCB board containing power regulation module, PWM conversion interface and BLE module, used for connecting to the nitrite sensor module. (c) Nitrite sensor module shielded by black vinyl tape over the detection region while exposing the urine inlet.

Typical time series plots for a 0 ppm nitrite solution (negative sample) is demonstrated in Figure 3.15. Compared to the dry-state signal SD seen in Figure 3.10 is less than 7% with Microplate Reader measurement, it is now very straightforward to observe the process variations in R_λ, A and I_0 (we can see at least 14% variation with the 5 sensors), which may arise from electronic

---

[6] For all the sensor tests, we prepare the detection region of the reagent strips using the pad (~350 µm) peeled off Nitrite Test Strips (#2745425) from HACH®.

component manufacturing, or sensor assembly (alignment and orientation of components, distance between photodiode and LED, etc.) process, particularly the latter. Fortunately, the signal normalization method we proposed in (3-11) works very well to mitigate this type of variation. In Figure 3.15, the wet-state signal of the sensor with the lowest dry signal (~30 ms pulse width) is also much lower than the rest four sensors. The normalized signals for the five sensors are listed in the inset of Figure 3.15, though some level of distribution is still ineluctable, since relative changes between $T_{lumped,DRY}$, $\alpha_{scatter,DRY}$ and $T_{lumped,WET}$, $\alpha_{scatter,WET}$ are not constants and variation in paper thickness exists as well.
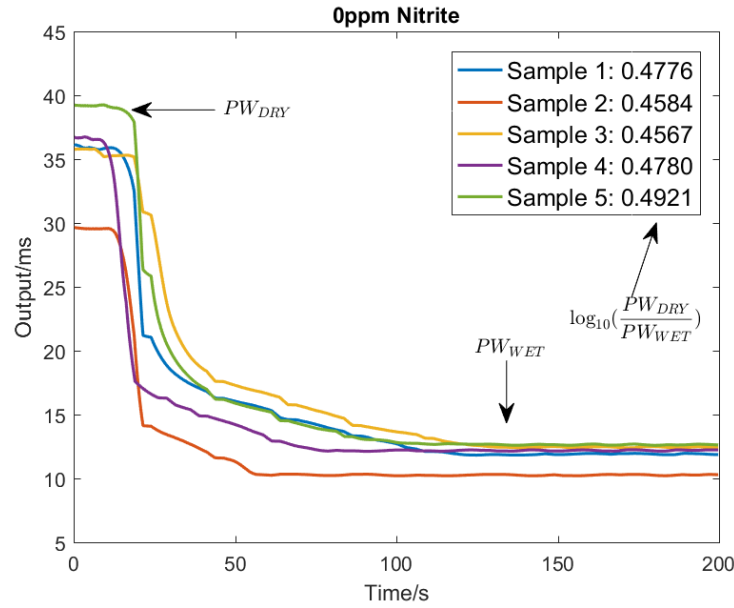
Figure 3.15 Time series plot of 5 sensors for 0 ppm nitrite solution

Typical time series plots for various nitrite concentrations are summarized in Figure 3.16. Notice that each different nitrite concentration is tested with a distinct sensor, since a single sensor cannot be used twice owing to the irrevocable Griess reaction. The right panel of Figure 3.16 is the same measurement results as the left panel but with longer duration exhibited in the plot. Accordingly, the normalized signals are tabulated in each inset. The left panel uses wet-state signals at 2.5 minutes where stabilizing trend is witnessed globally, while the right panel takes wet signals from around 5 minutes to ensure further stability. (Keep in mind that the Griess reaction product passing long duration might lose diagnostic significance.) The results are also plotted as the calibration curves in Figure 3.17, in which the trend is basically linear in the range of 1~8 ppm. Leveling off is seen at both ends, in the lower range due to digitizing and computing loss while for the higher

concentrations ascribed to the deviation from Beer-Lambert Law, Section 3.7.2. Thus, the detection range would be 0~10 ppm. It is seen that the calibration curve based on the longer reaction time will be beneficial for the detection of higher nitrite concentration, while for the lower range, 2.5 minutes from taking dry measurement as close to common dipstick suggestion (2 minutes) is enough. Another important observation is that SDs for higher concentrations in the calibration curve is also larger, since the photocurrent is very small relative to noise current for a high nitrite level and any variation will be exaggerated by the reciprocal Pulse width modulation and normalization.
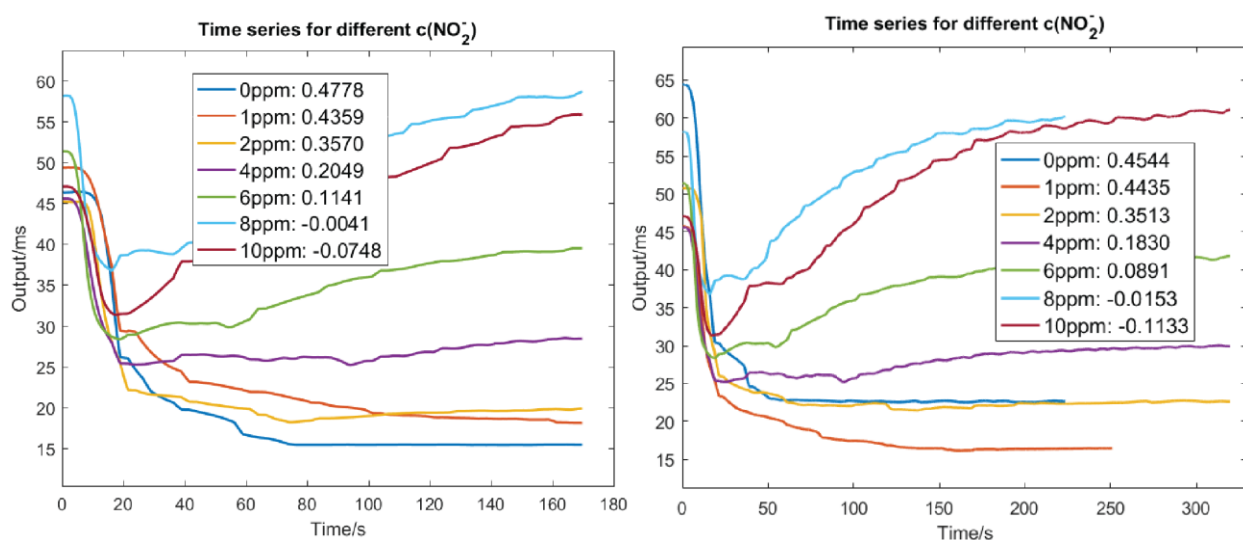
Figure 3.16 Time series plots and calibration values for different nitrite concentrations
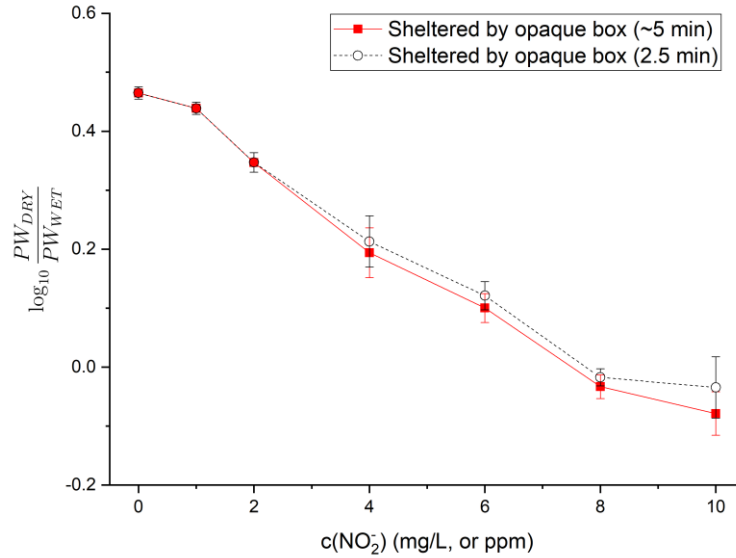
Figure 3.17 Calibration curves using long- and narrow- window wet state signals

3.7.4 System packaging influence

Here I want to discuss a bit about the influence of sensor (or system) being protected with black vinyl tape, Figure 3.14c) before I jump into the next chapter for system integration of reliability. The goal of using black vinyl tape is to explicitly to prevent ambient light interference, which is difficult to remove by normalization or other methods of compensation. The comparison of a sensor in various settings only doing dry-state measurement is shown in Figure 3.18. Obviously, the sensor without any protection (purple) experience the worst light interference from its surroundings, while a much more stable signal (yellow) is obtained when it is sheltered within a opaque Aluminum box (higher pulse width expected due to less ambient light captured). On the contrary, the sensor (black v.s. red, cyan v.s. green[7]) protected and packaged by the black tape is able to get signals of good quality without the necessity of a shielding box. The noticeable difference is that shorter pulse width (correspondingly brighter light sensed by the photodiode) is obtained in a black tape protected sensor. One reasonable explanation is that the stiff vinyl black tape packaging reduces the gap between the LED and the photodiode compared to only securing the edges of the folding architecture in Figure 3.2 and reflects the green light that will otherwise leave in different directions, thus providing a higher baseline input signal.

---

[7] 1 mA is the electric current in the LED instead of the 0.5 mA as is always the same case previously.
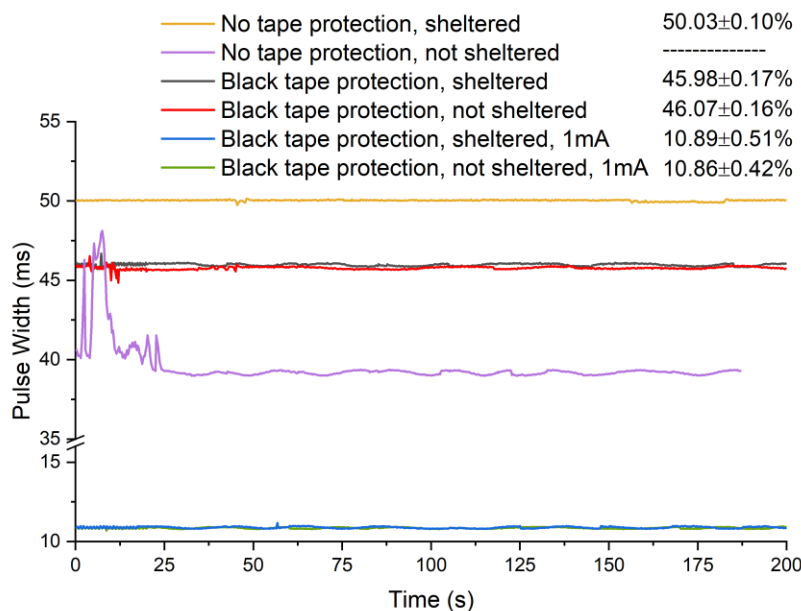
Figure 3.18 Dry state light absorption measurement under various conditions
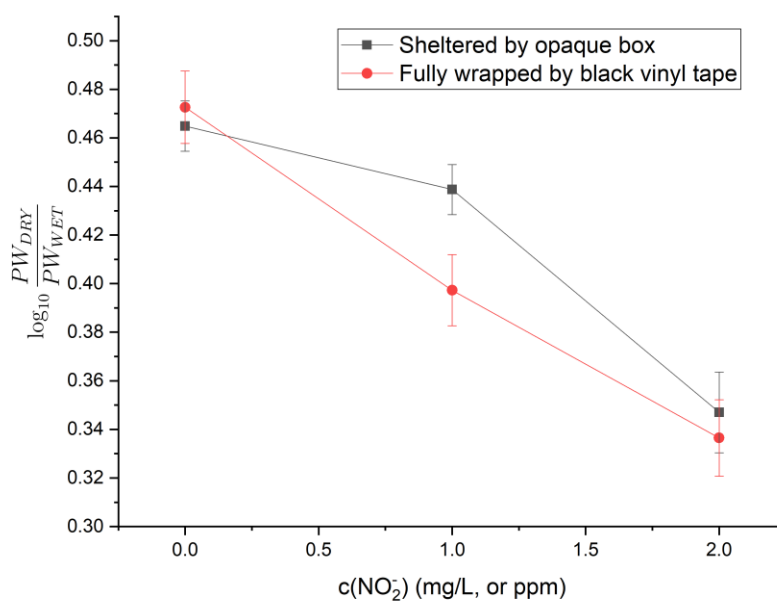
Figure 3.19 Calibration curves in low range (0~2ppm) for sensors with and without black tape protection

Accordingly, black tape protection reduces ambient light interference and consequently improves linearity in lower range and thus the detection limit (1.1ppm → 0.6ppm) of the sensor.

3.7.5 Reagent strip thickness influence

Since clinically any level of detection of nitrite is positive, the aim of the optimization on the detection limit would be as high as possible to reduce the false negative rates. According to Formula (3-11), one of potential methods to improve the sensitivity and detection limit of the sensor is to use thicker paper containing the Griess reagent. However, there exist concerns that thicker paper would introduce larger scattering and respectively larger noise. We investigated into doubling the thickness of the strip by stacking two layers together and providing 1 mA current for the LED such that the irradiance level is bright enough to propagate all the way through.
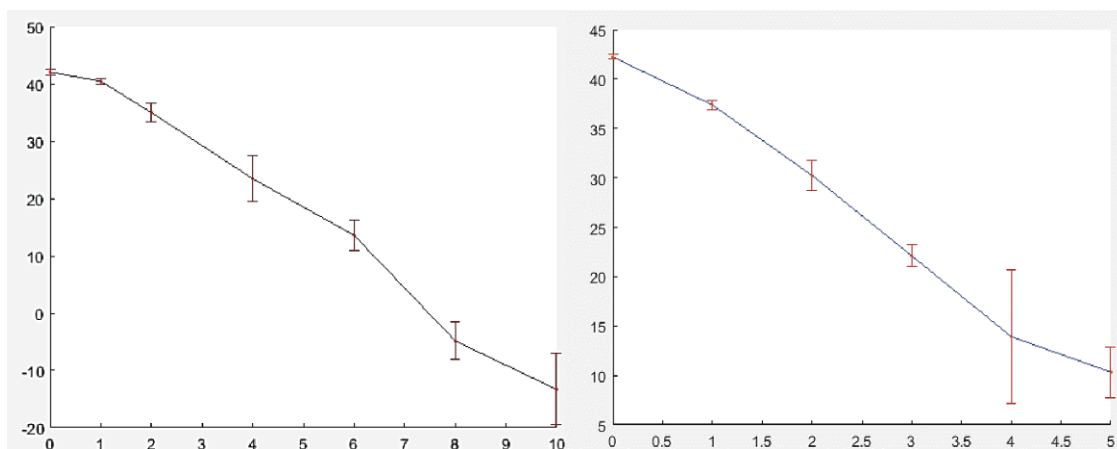
Figure 3.20 Calibration curves of differential pulse width versus nitrite concentrations for (a) 0.5 mA LED current and 350 µm test strip and (b)1 mA LED current and 2×350µm test strips.

Table 3.2 Sensor performance in different settings

Setting	LOD	Range
0.5mA, 350µm	0.6ppm, 1.1ppm (w/o black tape)	0~10ppm
1mA, 350µm	1.2ppm	N/A
1mA, 2×350µm	0.1ppm, 0.4ppm (10sigma)	0~5 ppm

Results are plotted in Figure 3.20 (the left panel for the 1-layer strip while right panel for 2-layer strip) and summarized in Table 3.2. It is apparently demonstrated that a thicker strip (700µm instead of 350µm) would greatly improve the limit of detection however at the cost of a shrunk detection range. A control test (2nd row in Table 3.2) by just increasing the LED current couldn't not achieve the similar improvement.

CHAPTER 4.   SYSTEMIC INTEGRATION AND RELIABILITY

The two separate modules (paper battery and nitrite sensor) have been described extensively in the previous chapters, but a urine sampling mechanism to justify the autonomous capability of the sensing platform seems to be missing. Besides, it also remains to be tackled that how to fabricate and package the platform, how the platform will be embedded in a diaper, and that whether the performance will be affected by the systemic integration and deployment into a diaper. In this chapter, I will discuss over these important issues as meticulously as I could, to make the conclusions or suggestions meaningful for those who want to scale the manufacturing or commercialize this technology.
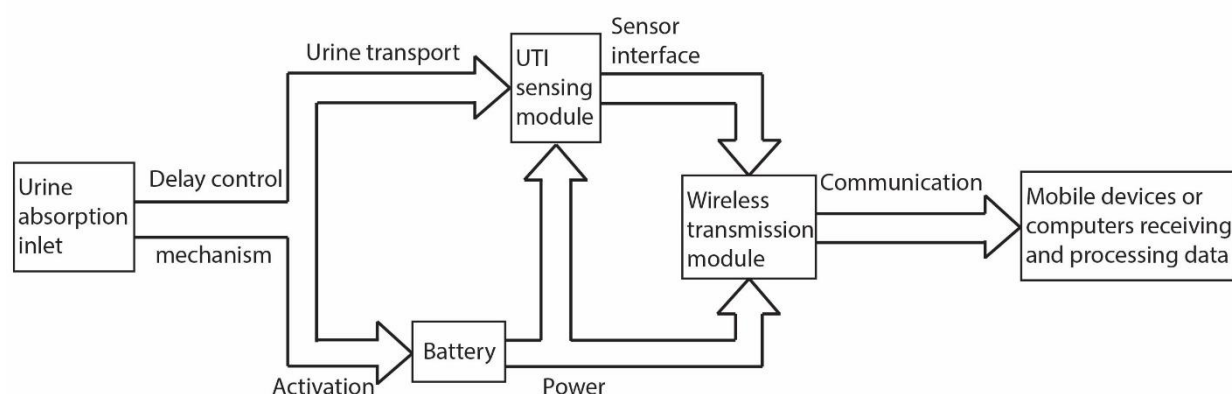
Figure 4.1 Illustration of working flow of the sensing system

4.1 Systemic Integration Design

4.1.1 Design constraints and embodiment

To ensure that the system can work in a fully autonomous fashion, it need further smart and seamless integration of the paper battery and the sampling/test strip, which should at least satisfy that the battery gets activated prior to sensor functioning (to catch dry state measurement) and meanwhile the battery lasts long enough for the sensor to collect sufficient data including wet state measurement (preferably > 2mins) of the sensing strip, as part of the operation flow of the system in Figure 4.1. The former is basically controlled by fluidic transport design to delay the arrival of urine at the detection region of the sensing strip, while the latter is by increasing battery size to

keep it running longer before the depletion of Zn electrode (refer to Section 2.4.1). Briefly, the timing constraint for the system is

$$t_{activation} < t_{arrival} < t_{activation} + T_{battery\ life} - \Delta t_{wet\_measurement}\ , \qquad (4\text{-}1)$$

where $t_{activation}$ is the activation time of paper battery (or equivalently the entire system) since urination, $t_{arrival}$ is delay from urination until urine arrives at the detection region of the sensing strip, $T_{battery\ life}$ is the duration of battery in the worst case satisfying the power requirement of data collection and transmission and $\Delta t_{wet\_measurement}$ is duration of interest for wet state measurement of the detection region of the sensing strip after it becomes wet. Specifically, dry state measurement length $\Delta t_{dry\_measurement}$ is

$$\Delta t_{dry\_measurement} = t_{arrival} - t_{activation} > 0, \qquad (4\text{-}2)$$

Consequently, we can get from the second '<' sign in inequality 4-1 that,

$$\Delta t_{dry\_measurement} + \Delta t_{wet\_measurement} < T_{battery\ life}\ . \qquad (4\text{-}3)$$

Intuitively, it is desirable to have as long $\Delta t_{dry\_measurement}$ and $\Delta t_{wet\_measurement}$ as possible, but in practice they are limited by the lifetime of paper battery, which is obviously not expected to be too powerful. Empirically, $\Delta t_{dry\_measurement}$ in the range of 10~20 seconds should provide sufficient information for the dry state of the sensing strip, and $\Delta t_{wet\_measurement}$ in the range of 2~3 minutes [1] is suitable for development of nitrite-specific colorimetric reaction and quantification of light absorption characteristics of the wet state. Before the urine-activated batteries dies and one full measurement period ends, data collection in the sensor module and transmission in the BLE module are conducted alternatively every 30 seconds.

In a nut shell, the integrated system should be designed such that both (4-2) and (4-3) hold and $T_{battery\ life}$ should be greater than 2.5~3 minutes.

An embodiment of such design is portrayed in Figure 4.2. In this embodiment, the entire system has only one main window for urine, while other area of the system should be well packaged and isolated from the environment by waterproof film or tape. A layer of filter paper collector alike a

vacuum sweeper is fixed inside the external package, connecting all the battery urine-absorbing windows and the circular inlet of the sensing strip (Figure 4.2a, b). When urine gets absorbed by the device through the only main window (Figure 4.2c, e), which is centered among all the urine-absorbing windows for the battery (this main window is preferred to be large to allow the ease of absorbing urine, which will be discussed in more details later in Section 4.2.1), urine will first be transported into each the battery urine-absorbing window via the filter paper collector, before it arrives at the sensing strip inlet the battery (the top bottom corner of the collector in Figure 4.2b-c). The urine-absorbing sensing strip packaged by hydrophobic transparent seals (preventing the wetting of strip before battery activation) is consisted of a circular inlet (radius r), a transporting path (length d, width w) and a squared-shaped (length s) detection region (Figure 4.2d). The upside of the inlet is exposed to the end of the urine-absorbing filter paper collector and the detection region is aligned between the photodiode and the LED (as in Figure 4.2b, c and e). By designing the geometry of the sensing strip, especially the transporting path, to control the delay from the strip inlet to the square-shaped detection region, it can be guaranteed that the battery is activated before the urine arrives at the square-shaped detection region, which satisfies the first constraint (4-2) and in turn tunes $\Delta t_{dry\_measurement}$ at the same time. In regard to the second constrain (4-3), the solution is to straightly lengthen the battery, which is not really attractive. In consequence, we need to find out the smallest form factor for the paper battery that still supplies ample power.
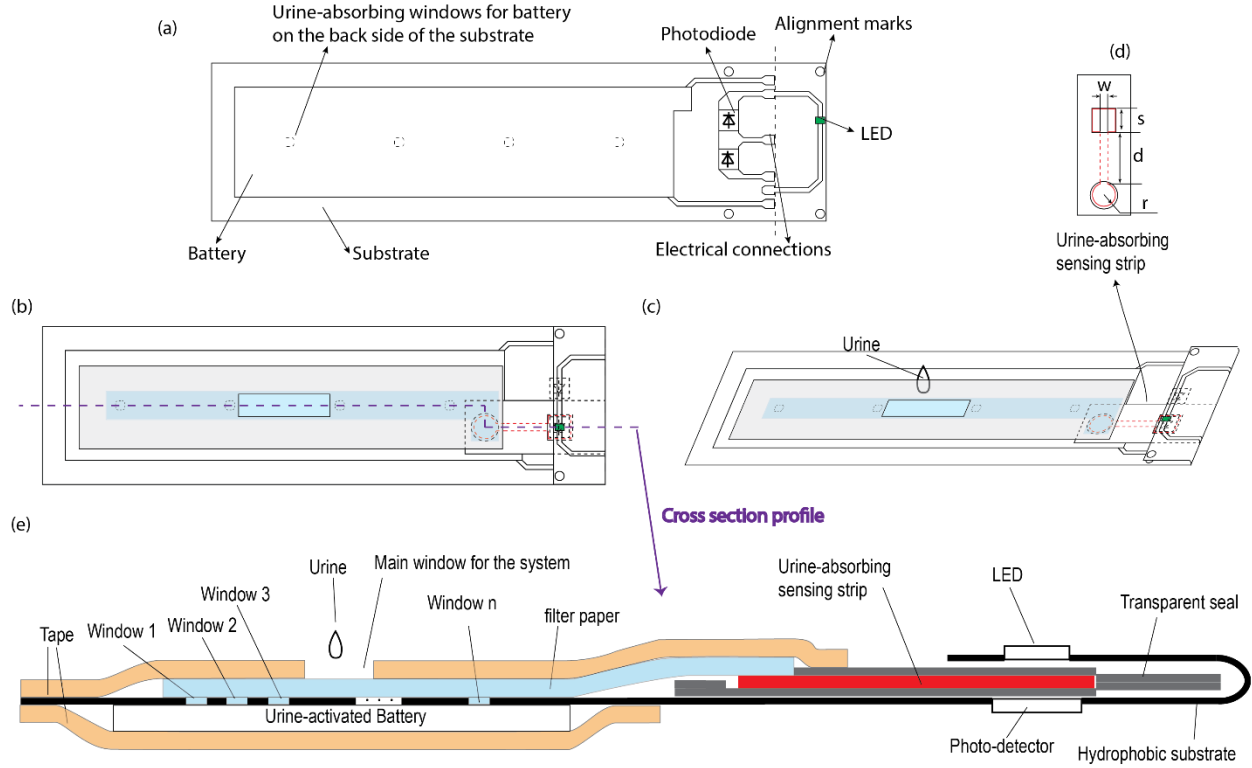
Figure 4.2 (a) UTI sensor layout without urine flow guiding paper and top packaging layer (top view). (b) UTI sensor folded in use. (c) Perspective view of the UTI sensor in use. (d) Layout of the sensing strip. (e) Cross-section of urine transporting path of activating the battery and entering the test strip.

4.1.2 Paper battery specifications: dimensions, activation time and duration

Having decided on the single-cell stacking design (Section 2.4.2) for the paper battery to provide the best power performance, we still need to determine its dimensions, which should be neither too small (lacking power) nor extravagantly huge (wasting space and materials).

From Section 3.6, we know that the voltage regulator need to supply 6.508 mA current at 2V, which consumes about 23.7 mW given that its efficiency is 50%~60%. More accurately, the power demand on the urine-activated paper battery can be probed by using a wall-plugged power supply instead to operate the sensing system at a series of working voltages ranging from 0.5 V to 1.0 V, and monitoring the current I_{IN} and thus power consumption $P_{REQUIRED}$ (Figure 4.3). From the results, we can basically affirm that the urine-activated paper battery must maintain a power output level of $P_{REQUIRED}$, 21~24 mW, for at least 2.5 minutes, to make the sensing platform function.

What is more, the conversion efficiency drops as the input voltage decreases. The dynamic process is that, with the increment of the active area of the paper battery since urine activation, its power capability (maximum current output level) gets boosted with an equivalently decreasing internal resistance, which in turn increases V_{IN} for the boost converter and reduces the power requirement of the system (Figure 4.3). Once the power capability of the battery achieves the power requirement, the entire system starts to function. V_{IN} keeps climbing until it hits a certain value corresponding to the lowest battery internal resistance and transitions to fall. As the active region of the urine-activated battery depletes gradually, its power capability degrades with an equivalently growing internal resistance, before it eventually can't keep up with the consequently increasing desired power in Figure 4.3, when the system comes to a halt and one sensing activity ends.
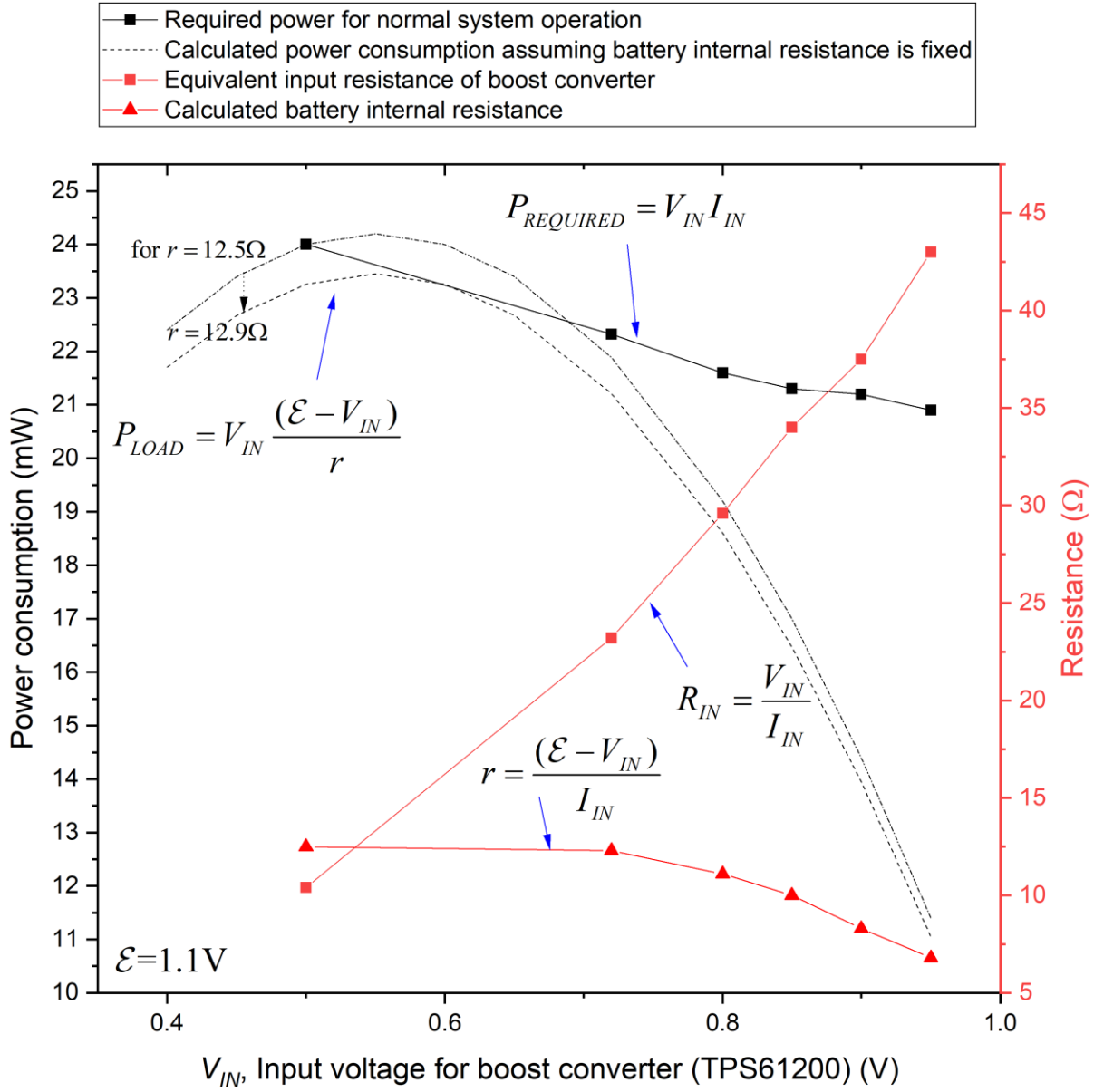
Figure 4.3 Power consumption (left axis) and equivalent input resistance (right axis) of the entire system versus input voltage for the DC-DC boost converter (or the working voltage of battery)

To quantitatively analyze the requirement on battery, we might tentatively apply a DC battery-load circuit model. First, besides the required power for load, $P_{REQUIRED}$, we can also calculate the equivalent input resistance of the system, R_{IN}, looking from the input of the boost converter (Figure 4.3), and equivalent battery internal resistance r, with respect to the input voltage V_{IN}. It is not difficult to find that battery internal resistance increases with V_{IN}. In fact, their positions should be

reversed in cause and effect, but V_{IN} is chosen as X-axis for the ease of connecting battery internal resistance r (inversely representing its power capability) and required power consumption for the system, $P_{REQUIRED}$. Moreover, r is apparently approaching an extreme around $V_{IN}=0.5$ V. Approximately, we can deduce that

$$r = \frac{\mathrm{E}e \cdot V_{IN}}{I_{IN}} = \frac{\mathrm{E}e \cdot V_{IN}}{P_{REQUIRED}} V_{IN} \le \frac{1}{21mW} \frac{(\mathrm{E}e \cdot V_{IN} + V_{IN})^2}{4} \approx 14.4\Omega , \qquad (4\text{-}4)$$

where $\mathcal{E}$ is the OC voltage or electromotive force of paper battery, set as 1.1 V. Given that $P_{REQUIRED}$ doesn't change significantly with the efficiency of boost converter falling within 50~60%, the equal sign holds or approximately holds when $V_{IN}=0.55$V. Furthermore, when V_{IN} decreases to approach 0.55V, $P_{REQUIRED}$ grows slowly away from 21 Mw. Hence, r should be smaller than a value smaller than 14.4 Ω.

Based on the characterization of single-cell stacking battery (Section 2.4.2), we can estimate that the internal resistance for a 24 mm $\times$ 24 mm battery is around 20 Ω within the first 3 minutes when powering a 0.1 kΩ load. If we consider the OC voltage of the paper battery as 1.1 V, then the largest power the system is able to extract from the battery would be only 15.1 mW when the load equals 20 Ω, because the maximum power P_{MAX} a load can extract from a battery with OC voltage $\mathcal{E}$ with internal resistance r is

$$P_{MAX} = \frac{\mathrm{E}^2 e}{4r}\epsilon. \qquad (4\text{-}5)$$

To more precisely determine the largest permittable r (equivalently the smallest required power capability) for the battery, sweep r and plot load power consumption P_{LOAD} (as described in Figure 4.3) versus V_{IN} until the curve P_{LOAD} - V_{IN} is tangent to the curve $P_{REQUIRED}$ - V_{IN}. From Figure 4.3, it is expected internal resistance of paper battery, r, doesn't exceed 12.9 Ω, the extreme point corresponding to the 0.6 V input voltage case for the boost converter, in which R_{IN} is 14 Ω, because if r is higher than 12.9 Ω, the boost converter will see an input voltage lower than 0.6 V, thus requiring power higher than 23.3 mW due to a reduced efficiency as in Figure 4.3, but unfortunately a 1.1V battery with 12.9 Ω internal resistance can only supply its load 23.4 mW at most, based on Equation (4-5). Hence, it literally means that, with a nominally 1.1 V battery, the

boundary or "turn-on" (the lowest normal working) input voltage for this sensing system should around 0.6 V, lower than which the system is not likely to be in steady operation state.

Overall, it means that, we would probably need to extend the battery size. That being said, the internal resistance of urine-activated battery is not a constant value, and it is affected by the battery current output. A higher current drawing might exploit the power capability of urine-activated battery and diminish the self-discharging effect of copper migration (Section 2.4). Therefore, it is relevant to test urine-activated batterie of various dimensions on a ~30 Ω load, to characterize its power capability and capacity on a load close to the system. The results are presented in Figure 4.4 (discharging profiles over time for batteries of three different dimensions), and Figure 4.5 (discharge capacity profile versus battery voltage, and against electrode area). The test results are all under the load of a parallel of a 33.2 Ω resistor and a 4.7 µF capacitor, which is typically used at the input of the boost converter to filter noise from the source.

In Figure 4.4, all three differently sized batteries activate in about 5 seconds, and it can be seen that the 22×22 mm^2 (more compact than the one 24×24 mm^2 characterized in Section 2.4) battery supplies an output beyond 21.5 mW for 5.4 min, while the other two gauges for 8.9 min and 13.9 min respectively. Integral is done on Figure 4.4 to get the energy consumption (discharge capacity) for the batteries, and it is plotted against battery voltage in the top panel of Figure 4.5. Using the threshold voltage level in Figure 4.4, we can rate the discharge capacities for batteries of different sizes, bottom panel of Figure 4.5. The areal capacity density is 44±6 mW·min/cm^2. Even though battery internal resistance changes over time and then the load-consumed power follows slightly (in the range of 21~24mW), we may still be able to use the results in Figure 4.5 to estimate the working duration of a battery and to assist the geometric design of the urine-activated battery. For example, the rated capacity for the 32×22 mm^2 battery is 200 mW·min, so it should last 8.89 min if the average power consumption is considered as 22.5 mW; similarly, 5.56 min and 14.13 min for the other two designs.
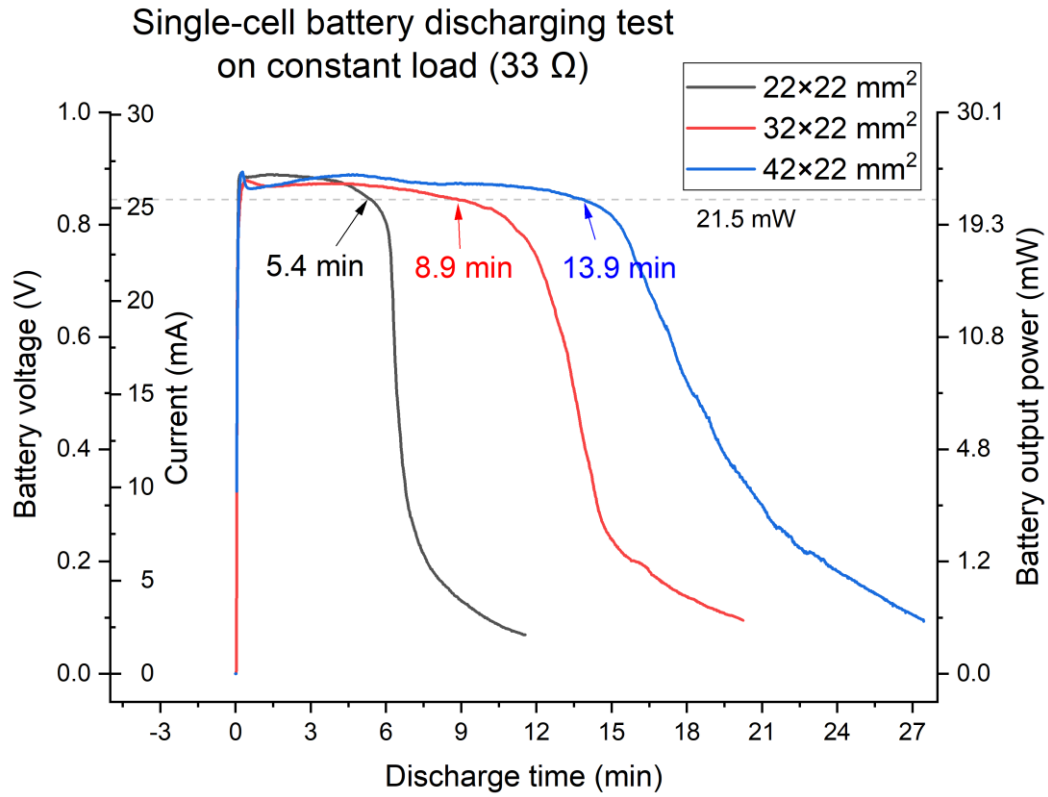
Figure 4.4 Single-cell battery discharging characteristics on a 33 Ω load with respect to 3 different electrode areas[8]

---

[8] Note that the right axis, battery power, is not in linear scale, but in correspondence to the voltage and current values on the left axis horizontally. The left axis for both voltage and current is in linear scale.
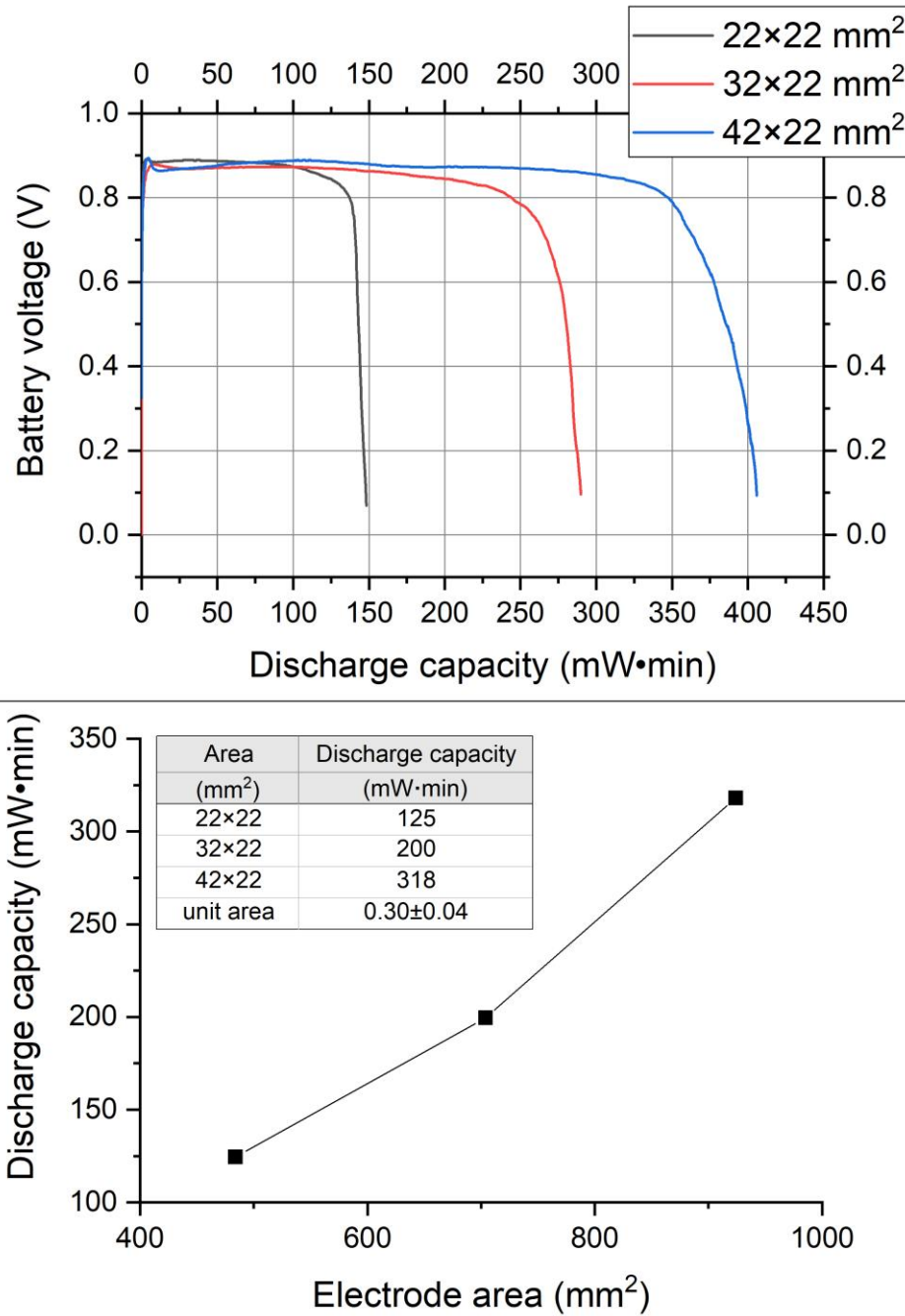
Figure 4.5 Discharge capacity profile of single-cell batteries of different electrode areas. Top panel: Cell voltage versus discharge capacity; bottom panel: Battery discharge versus electrode area.

To obtain a substantial tolerance, I prefer 32×22 mm^2 as the battery dimension, which grants plentiful power over 8 minutes while still stays compact in footprint. To warrant my choice, the duration of 32×22 mm^2 battery consistently powering the whole system, along with its activation

time, is studied with regard to different filter paper parameters for the electrolyte reservoirs. The gauges (thickness, particle retention size and water flow rate) for different filter paper grades are summarized in Table 3.1. Particle retention size is related to the pore size of filter paper while water flow rate is affected by both pore size and porosity of filter paper. The results are presented as a double-Y column chart in Figure 4.6, where in the X-axis "Grade #" means a layer of Grade # filter paper is used as KCl electrolyte reservoir for Zn electrode while a layer of Grade 3 filter paper is as $CuSO_4$ electrolyte reservoir for Cu electrode; "2×Grade 3" means one layer of Grade 3 filter paper is used as KCl electrolyte reservoir for Zn electrode while the other layer of Grade 3 filter paper is as $CuSO_4$ electrolyte reservoir for Cu electrode. All the electrolyte-loaded filter papers are prepared with the same weight of KCl (s) or $CuSO_4$ (s) in a 32×22 mm^2 through soaking and drying.

All the battery samples for different electrolyte reservoir categories under test survive for longer than 6 minutes. Also, the trend of increasing duration is seen as the electrode reservoir thickness reservoir is thicker between two electrodes, primarily ascribing to slower copper ion migration induced Zn electrode exhaustion (Section 2.4.1). Among all, "2×Grade 3" has the largest duration since a thicker $CuSO_4$ reservoir also makes longer path for the evenly distributed $CuSO_4$ in it to traverse to Zn electrode surface. Notwithstanding, the change between the duration of Grade 113 (10 min, which has a large standard deviation 5.6 min) and others is not very statistically significant even though Grade 113 is the thickest filter paper in the Whatman^{TM} range. It is most likely because Grade 113 filter paper has a creped surface and thus poor uniformity so that the effective Zn electrode area is prone to variation. In the same plot, activation times of all batteries samples are within the range of 5~7 seconds, except for that of "2×Grade 3" (27~57 seconds). Its thickest profile (2×390 μm), finest particle retention size (6 μm) and slowest filtration rate (28 ml/min) might be responsible for the abrupt rise.
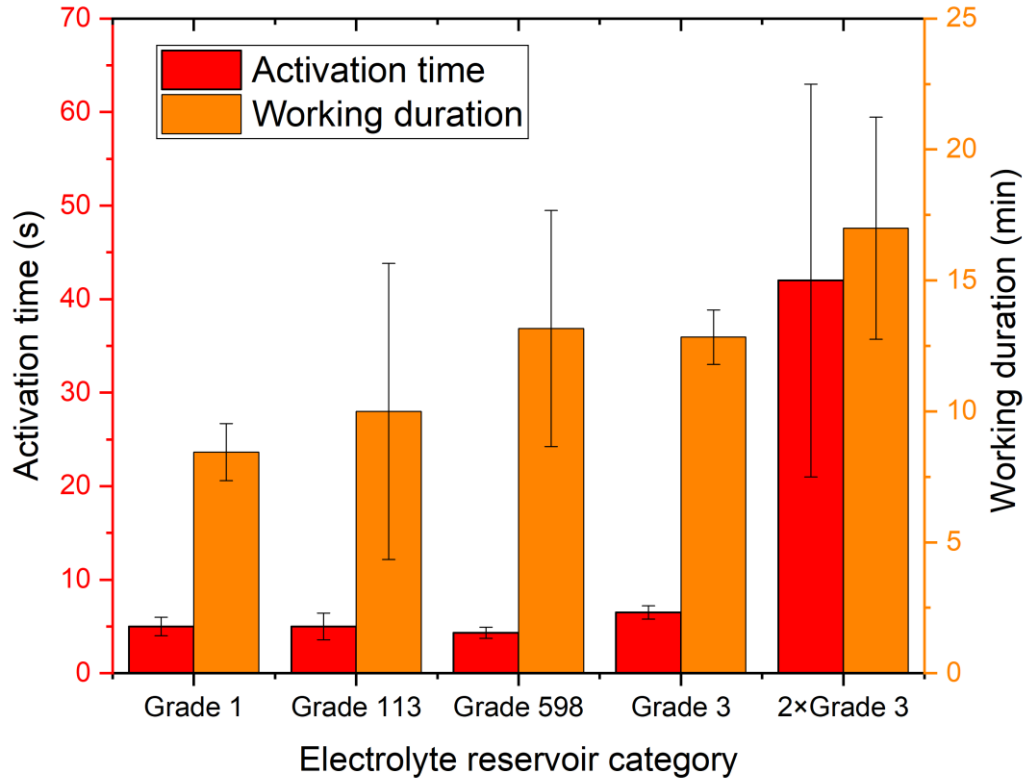
Figure 4.6 Activation time (left axis) and working duration (right axis) of urine-activated battery with varying electrolyte reservoir loading filter paper category. ("Grade #" means a layer of Grade # filter paper is used as KCl electrolyte reservoir for Zn electrode while a layer of Grade 3 filter paper is as $CuSO_4$ electrolyte reservoir for Cu electrode; "2×Grade 3" means one layer of Grade 3 filter paper is used as KCl electrolyte reservoir for Zn electrode while the other layer of Grade 3 filter paper is as $CuSO_4$ electrolyte reservoir for Cu electrode.)

Altogether, I opt for 32×22 mm^2 (active area) sized battery with the most widely used Grade 1 filter paper as electrolyte reservoirs (for KCl and $CuSO_4$) for the integrated sensing system. As a consequence, we will have

$$\begin{cases} t_{activation} = 5 \pm 1 \; s \\ T_{battery\;life} = 8.44 \pm 1.09 \; min \end{cases}. \tag{4-6}$$

The characterization result is also consistent to the rated duration 8.89 min.

4.1.3 Delay control in the urine-absorbing sensing strip

Having settled $t_{activation}$ and $T_{battery\ life}$ in (4-6), it is time to focus on tweaking $t_{arrival}$ to meet the design constraints (4-2) and (4-3), which mainly relies on properly parameterizing the geometry of the sensing strip, especially the transporting path (Figure 4.2d). For example, the currently adopted implementation ($2r$=7mm, d=10mm, w=1.6mm and s=5mm), controls the delay at 18.4±2.7 seconds (enough for the battery to generate enough power turning on measurement circuits since $t_{activation} = 5 \pm 1\,s$) in the strip transporting path. That means in this implementation, $\Delta t_{dry\_measurement} \approx 13.4 \pm 2.9\,s$ and thus we can easily get a $\Delta t_{wet\_measurement}$ larger than 3 minutes given that $T_{battery\ life} = 8.44 \pm 1.09\,min$ from (4-6).

In spite of four tunable parameters (r, d, w and s) for the sensing strip geometry, the transport path length d and width w are cast more light upon instead of the circular inlet radius r and detection region length s. Length s is expected to cover the photodiode light-sensitive (or LED light-emitting) area, but not too large, which might raise the risk of color development non-uniformity and unnecessarily increase $t_{arrival}$ or more accurately the transition time from dry state to wet state. Changing radius r won't affect $t_{arrival}$ much if r is larger than w, because the urine flow in the strip is subject to paper wet-out abundant flow [83], Figure 4.7a. An abundant flow case in the paper wet-out process refers to fluid flowing from a wider channel to a narrower channel, where the fluid flow in the wider channel performs as a non-limiting source to the subsequent narrower channel. Therefore, fluid travels as if it does in a constant-width channel with its fluidic front velocity ([83] mentions it as flow rate, which I believe is a misrepresentation) uninterrupted after the transition point in a varying-width channel. The counterpart scenario known as constricted flow is shown in Figure 4.7b, the assumption of non-limiting source is violated at the transition point when fluid flows from a narrower channel to a wider one. Due to the principle of conservation of mass flow along a channel, the fluid front velocity must decrease in a wider channel.
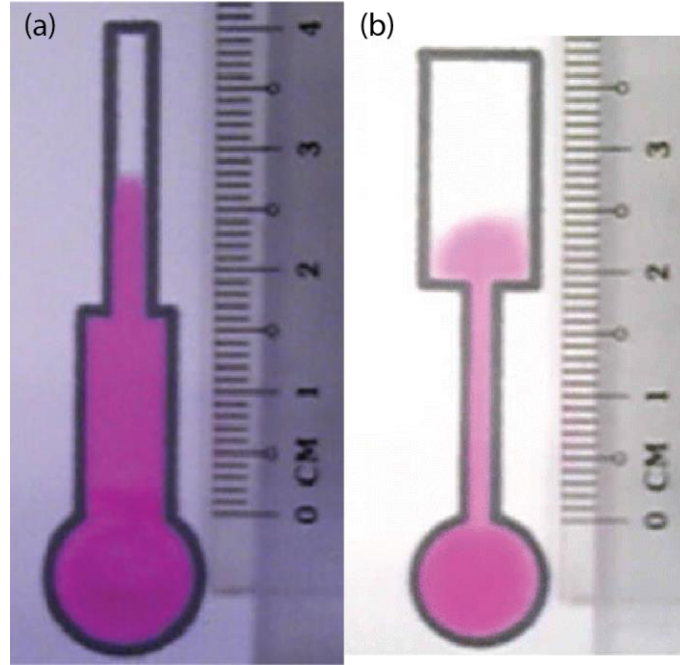
Figure 4.7 (a) Abundant fluid flow and (b) constricted fluid flow in a varying-width channel. Reproduced with permission from [83]. Copyright (2012) Springer.

The urine flow in a porous paper matrix is driven by capillary pressure while being inhibited by viscous resistance [84], and its transport dynamics in a wet-out process (from wetted area to dry area) in a one-dimensional horizontal constant-width channel can be described by Washburn's equation [85],

$$L^2 = (\frac{\gamma}{\eta}\frac{\cos\theta}{2})rt,$$

$$\text{or } t = (\frac{2\eta}{\gamma r \cos\theta})L^2,$$

(4-7)

where L is the travel distance of the fluid front, γ is the surface tension of the fluid, η is the viscosity of the fluid, θ is the contact angle between liquid fluid and paper matrix (cellulose fiber), r is the average paper matrix pore radius and t stands for time. It is derived from Poiseuille's Law,

$$\frac{dL}{dt} = \frac{(\Delta P + \frac{2\gamma}{r}\cos\theta)}{8r^2\eta L}(r^4 + 4\epsilon r),$$

(4-8)

where ΔP stands for the sum of all the influencing pressures acting on the fluid along the distance excluding the capillary pressure, $\frac{2\gamma}{r}\cos\theta$, and ϵ is the coefficient of slip, which is usually taken as

zero for liquids wetting the capillary (no-slip condition). ΔP usually includes atmosphere pressure and hydrostatic pressure, but may be neglected in capillaries where surface tension dominates ideally.

Depending on the equation mentioned above, we know that $t_{arrival}$ is supposed to change quadratically with the transport path length d, i.e. $t_{arrival} \sim d^2$, but regardless of width w, as long as its inlet is fed by a non-limiting fluid reservoir. The delay in the sensing strip is characterized with respect to varying d, w and packaging material (affecting the lumped contact angle θ in Equation (4-7)), to rationalize the application of capillary flow theory on my sensing platform and meanwhile to explore appropriate parameters for optimal timing control. The experiment is performed with Grade 1 filter paper patterned and packaged[9] as in Figure 4.2, where its circular inlet is not in direct contact with a non-limiting water reservoir but connected by a segment of buffering filter paper (not drawn) while the circular inlet itself is covered by dressing tape (OpSite Flexifix, Smith & Nephew). Only the buffer paper is exposed to the non-limiting reservoir, which is close to the embodiment setting (Figure 4.2). Accordingly, the $d{\times}w$ sized bridge linking the circular inlet to the square region is sandwich-packaged by air/wax paper (as a reference set), dressing tape (sticky side)/wax paper and dressing tape (sticky side)/shipping tape (non-sticky side, 3M 142 Scotch[TM]) for comparison. The delay is chosen between the moments of buffer inlet contacting non-limiting fluid reservoir and fluid arriving at the square region. The results are summarized and shown in Figure 4.8.

---

[9] For a packaged paper path, a ø 0.5 mm pinhole is drilled on the package near the end of the path, which is a vent for balancing the air pressure.

- air/wax paper, w=1.6mm
- dressing tape/wax paper, w=1.6mm
- dressing tape/shipping tape, w=1.6mm
- dressing tape/shipping tape, w=3.2mm

Equation	$t_{arrival}=t_0+kd^2$, (seconds)			
Weight	Instrumental			
Curve color	black	red	blue	green
t_0	3.24	3.09	5.65	7.52
k	0.0509	0.0412	0.119	0.108
Pearson's r	0.991	0.967	0.999	0.997
R^2	0.982	0.935	0.999	0.994
Adj. R^2	0.976	0.913	0.998	0.992

Dash lines are fitted curves
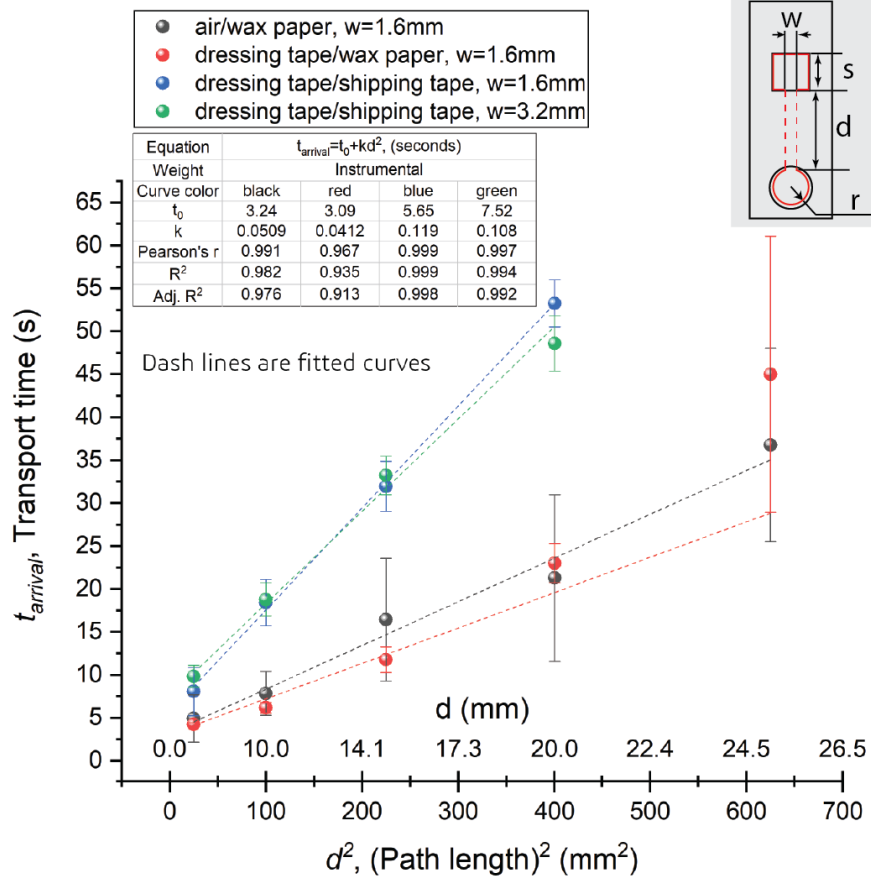
Figure 4.8 Transport delay against path length for urine sensing strips of different packaging configurations and path width w. Inset: notations of the urine sensing strip geometry design.[10]

The advancements of fluid (water) fronts for blue ($w=1.6$ mm) and green ($w=3.2$ mm) datasets are showing a great consistency, which proves that paper path width w is not impacting the delay significantly. All four sets of data comply with quadratic relationship, but the coefficient of $t_{arrival}$ with respect to d, $\frac{2\eta}{\gamma r cos\theta}$, varies among them. Specifically, fluid flows relatively faster in the bridge packaged by air/wax paper and dressing/wax paper than by dressing/shipping tape. When Washburn developed the equation, he assumed fluid flows inside capillary tubes. However, in this case, the variation of the coefficient is owing to surface tension between fluid and packaging materials (wax paper, dressing tape, or shipping tape), which introduces a countering pressure in ΔP, if we look back on the derivation equation (4-8). Hence, we need to correct the coefficient

---

[10] The four columns of parameters from left to right for fitted curves correspond to the datasets in the legend from top to bottom, in the color order of black, red, blue and green.

$\frac{2\eta}{\gamma r cos\theta}$ to $\frac{4\eta}{2\gamma r cos\theta - r^2 |\Delta P|}$ correlated with the materials encapsulating the cellulose fiber network. Wax paper is more hydrophobic (smaller $|\Delta P|$) than the non-sticky surface of shipping tape, so the red curve is below the blue one and the green one in Figure 4.8. Another observation is that for long filter paper bridge enclosed by wax paper, the noise is getting much higher and the time delay becomes further above the fitted line since wax paper slowly assimilates water, in turn alters its surface property and deforms. As a reference experiment, air/wax paper packaging is noisy as well since the bridge is not fixed on plane while its inlet is anchored and then when fluid comes, it bends like a cantilever, introducing some negative hydrostatic pressure. Therefore, it might not make sense comparing the black and red data. The last thing to mention is that, the fitted curve is not in the form of Equation (4-7), but

$$t = kd^2 + t_0, \tag{4-9}$$

where k is the constant coefficient, and t_0 is the time lapse duration before fluid leaves the circular inlet. From the fitting parameter table in Figure 4.8, we can tell that t_0 is around 5.7~7.5 s. Since the inlet segment is also subject to the same physics except that its shape is not regular as a one-dimensional model, we may also test the $t \sim L^2$ relationship on the inlet as well. If we choose the median value for t_0 (6.6 s) and slope k (0.113 s/mm^2), the effective distance for the inlet is then calculated to be 7.6 mm, which is very close to the diameter $2r=7$ mm.

This observation brings another delay control mechanism in the situation of limited space budget– instead of varying the length d, a fixed-total-length (d) N-segment abundant-flow path can be devised with the width w_i of the ith segment smaller than that of its preceding segment (w_{i-1}), but larger than that of its subsequent segment (w_{i+1}), and meanwhile d $= \sum_{i=1}^{N} d_i$ as shown in Figure 4.9. In this scenario, each segment serves as a non-limiting reservoir for the following one and the total arrival delay can be predicted by

$$t = k\left(\sum_{i=1}^{N} d_i^2\right) + t_0 < k\left(\sum_{i=1}^{N} d_i\right)^2 + t_0 = kd^2 + t_0, \tag{4-10}$$

where the right side of the inequality is the same in Equation (4-9), indicating that this scheme provides a shortened adjustable delay for a fixed total length d. Nevertheless, it is suggested that not too many segments be created such that the last one connecting the square-shaped detection

region is too narrow for satisfying the non-limiting reservoir assumption. Even though the total delay as $t_{arrival}$ is shortened, the settling time for fully wetting the detection region (transition from dry to wet state) will be lengthened because it is a constricted flow from the last segment to the detection square and the flow rate instead of the fluid front will be coherent across the joint. (Well, an channel as wide as the square length is not expected either, which sets minimal restriction on the refluxing of dye-developed liquid.) Additionally, if someone wants to extent the delay, set the widths of segments in non-descending order, which however is not going to be predicted by the previous equations due to the violation of non-limiting reservoir but still reproducible [84]. I will leave this calibration open.
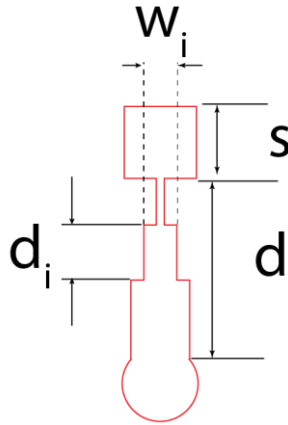
Figure 4.9 Multi-segment abundant-flow path layout

There is one important thing where I want to attract attention that even though the penetration of the fluid in filter paper can be described accurately to quantify $t_{arrival}$, it doesn't mean that wet region can't intake urine anymore or equivalently the entrapped air in the matrix has been completely replaced by urine, which affects light transmission essentially. A fully-wet paper is desired to provide reliable and reproducible light absorption signal. The dynamics of urine flow in this partially wet paper is somewhere between Washburn flow and fully-wetted flow [25], which implies that the delay of fully wetting a region is expected to be longer than $t_{arrival}$ for that region.

The foregoing discussion and experimental results can literally act as a guideline for geometric design of the sensing strip in terms of fluidic transport delay control. Evidently, packaging the sensing strip to confine urine flow is necessary, because not only does it offer good timing

controllability but also protects electronic components from the urine. Recalling that $t_{activation} = 5 \pm 1\ s$, the parameter setting ($2r$=7mm, d=10mm, w=1.6mm and s=5mm) along with dressing sticky side/shipping tape non-sticky side encapsulation controlling the delay at 18.4±2.7 s, is preferable since it implements a $\Delta t_{dry\_measurement}$ of ~10 s with a small footprint while using wax paper packaging for the same amount of delay requires double the length with poorer reproducibility. In addition, shipping tape is preferred over wax paper for its better optical property.

Someone may be pondering why I use the adhesive side of dressing tape and the non- adhesive side of shipping tape to package the strip. Why not two shipping tapes given that dressing tape is also more translucent than shipping tape? Why non-adhesive side? The answers to these two questions are more fabrication-related issues. Shipping tape is stiff, not so stretchable and conformal as dressing tape when you use it to fix a 200~400 μm thick paper, which increases the risk of delamination and unreliability. As regards why the strip is taped onto the non-sticky side of a shipping tape, it facilitates fabrication and assembly process since the exposed adhesive side can naturally keep the encased strip still in place prior to aligning LED and photodiode.

4.1.4 Fabrication and assembly process and cost estimation on the materials

Having discussed and finalized the dimensions for the urine-activated battery and the urine-absorbing sensing strip, we know that $t_{activation} = 5 \pm 1\ s$ and $t_{arrival} = 18.4 \pm 2.7\ s$. Now the following step is to use a filter paper collector exposed at the main window to fluidically couple with battery reservoir inlet and sensing strip inlet as in Figure 4.2. After that, fold the platform to align LED/detection region/photodiode and use dressing tape to secure the collector and folded structure and to insulate the system, leaving only the main window for sampling urine. The comprehensive fabrication and assembly process is illustrated in Figure 4.10.
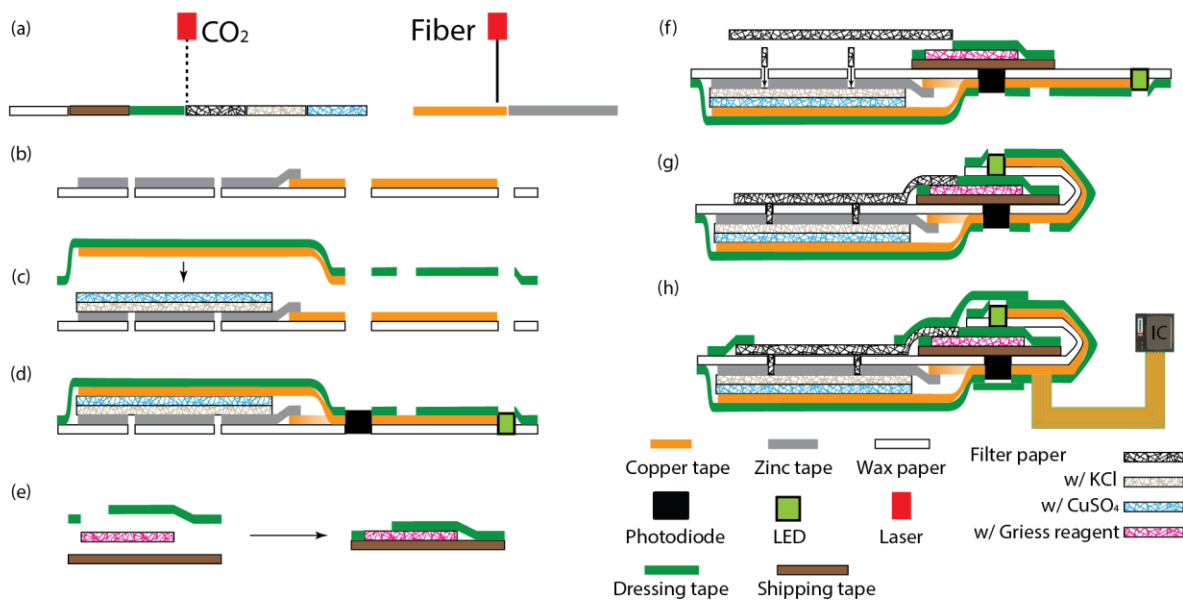
Figure 4.10 Fabrication and assembly process of the urinary nitrite sensing platform[11]

It is a sheet-to-sheet process, which can scale for mass production with appropriate manufacturing-compatible modifications. The detailed description and notes for each step in Figure 4.10 is itemized as follows:

(a) Laser patterning metallic tapes (battery electrodes and circuit connections), wax paper substrate, filter papers (battery electrolyte reservoirs, sensing strip and urine collector) and packaging tapes (dressing and shipping tapes).

My recommended laser setting (refer to Section 2.3 for its model and some specifications) is that 7/80/1000 (power/speed/PPI) CO_2 for engraving wax paper, 12.5/80/1000 CO_2 for filter paper, 12.5/100/1000 CO2 for dressing tape, 7/100/100 CO2 for shipping tape, 65/7.5/30 (power/speed/kHz) fiber for copper tape and 55/8/30 fiber for zinc tape.

Metallic sheet (particularly copper) cutting is quite sensitive to focus accuracy, so they should be fixed flat on the cutting table. Removing the copper tape backing assists heat establishment for cutting it, but it is not easy to get patterned pieces off the table. A trick might be helpful is that with its adhesive side up, fix the copper tape to the honeycomb cutting

---

[11] The transparency of the copper tape near the left foot of the photodiode has been adjusted in (d)(f)(g)(h) to show that the tape on the wax paper substrate and that from the Cu electrode are not connected on the horizontal plane.

table using a double-sided tape and then peel the double-sided tape off after laser patterning (pattern drawing need to be mirrored in this trick).

It is fine to pattern filter papers impregnated with chemicals except for sensing strips, in which laser cutting will produce brownish matters affecting the color change either physically or chemically. The patterned filter paper for sensing strips should be immersed in DI water for half an hour for those unwanted laser-cut products to be removed, while ultrasonication rinsing can expedite the process which however should be for less than 5 minutes to avoid pulping filter paper.

(b) Align-tape Zn electrode and circuit connections onto the wax paper substrate.

Some alignment-assisting marks can be written on the wax paper using $0.1/100/10$ CO_2 laser in "vect" mode without cutting through it.

(c) Align filter papers containing KCl and $CuSO_4$, Cu electrode (non-adhesive side down), and dressing tape, with the pattern on wax paper; press dressing tape to package the battery and circuit traces. The KCl and $CuSO_4$ loaded filter paper are prepared as described in Section 2.3.

This step is not trivial in manual fabrication given that no mating mechanism exists between filter papers. Small pieces of double-sided tape help. For skilled personnel, suggestion is making $CuSO_4$ reservoir area slightly larger than Cu electrode, and KCl reservoir size again slightly larger than $CuSO_4$ reservoir such that they can approximately adhere to the dressing tape.

There is an important feature that the cross-sectional view of the process in Figure 4.10 can't unveil. Since the conductive traces for connecting the battery, LED, photodiode and port for readout module are taped on the wax paper, it is not effortless to connect Cu electrode fixed onto another layer to the circuit trace especially as the non-sticky side of copper tape is against the wax paper substrate. One solution I used to employ is using a sort of anisotropic conductive adhesive transfer tape (3M 9703), which is a nice and robust interlayer via (connection). Later, I switched to the current method which is more inherent as depicted in Figure 4.11. The copper tape is cut into a rectangle along with S-shape tail that can be folded to disclose its adhesive surface of the long tail. When this already-matched copper tape and dressing tape is transferred to enclose the battery and conductive traces, the flipped tail with

its adhesive side revealed will stick to the wax paper substrate, becoming part of the traces, and the vertical via naturally forms.
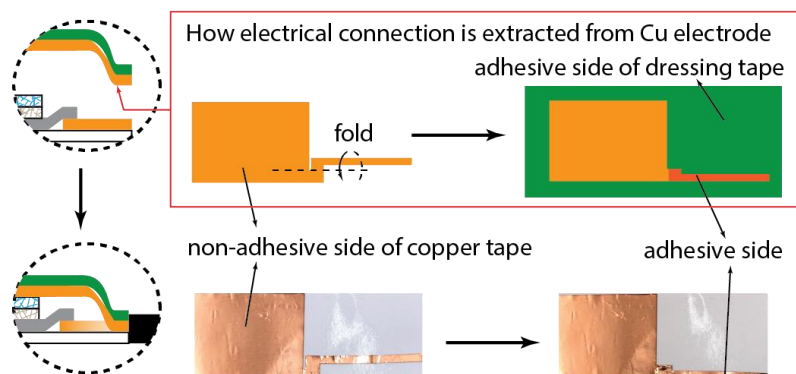
Figure 4.11 Illustration of vertical electrical via between battery Cu electrode layer and primary conductive trace layer (wax paper substrate)

(d) Laminate to strengthen the packaging (optional), and solder the photodiodes, LED, and any other components.

It may sound weird but is actually very crucial to keep the soldering behavior as reproducible as possible in manual fabrication to provide quality control on the sensor performance. The reproducibility includes the XYZ offsets of LED and photodiode with respect to the laser-defined openings on the wax paper substrate and their individual 3-dimensional angular displacements, since it absolutely affects the baseline noise level and thus the limit of detection.

(e) Align-assembly the reagent strip. The reagent loading protocol has been described in Section 3.4.

(f) Flip the device, add fluidic connections (filter paper) into the battery openings. Align the filter paper collector, the photodiode and the reagent strip, which can be taped onto the wax paper substrate bottom with the exposed adhesive (Section 4.1.3).

Fluidic connection between the collector and paper electrolyte reservoir is necessary, or otherwise there is a risk of liquid not drenching the paper matrix.

(g) Fold the device to align the LED/detection region/photodiode unit.

(h) Secure the folded architecture and urine collector with a layer of dressing tape, install or solder the interface circuit to the port and finally insulate all the active components.

Insulation is imperative, or else sensor signal fluctuates due to urine-induced capacitance/resistance change on the components as in Figure 4.12.
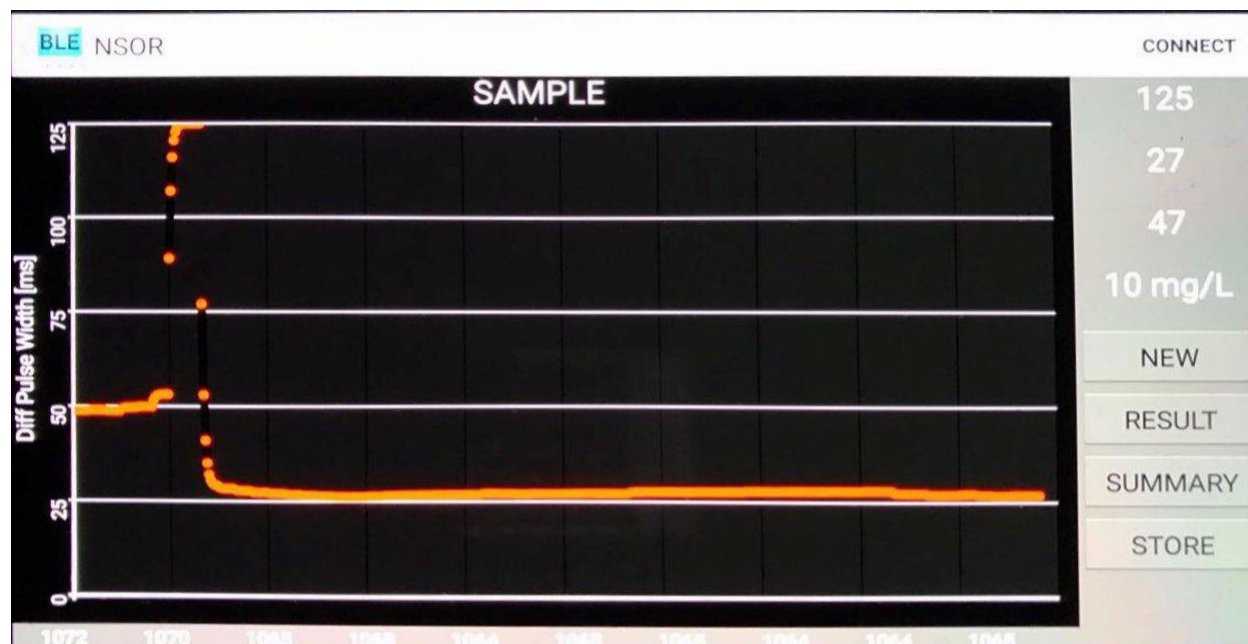
Figure 4.12 Real-time recording of the signal from an uninsulated sensor

In the final step (h), the main window is preferred to be opened above all battery inlets (inlets are created with respect to the 22×22 mm^2 battery, thus 2 inlets for a 32×22 mm^2 battery) and near the circular strip inlet, such as in Figure 4.10h instead of Figure 4.2b-c, to make the distances and thus the delays from the collector to the battery inlet and to the strip inlet the same and as short as possible. With the knowledge from previous subsection (Section 4.1.3), if the main opening is narrow and small as in Figure 4.2, it will take very long for the urine to travel from the main window to battery reservoir and strip inlet, which sort of inflates the time scale of the entire process. Though it might still work, the battery activation time will stretch and its effective duration for high power output will shrink, in particular when the device is embedded in a diaper (more extensive discussion on this situation is in Section 4.2). Anyway, it is certain unnecessary extra response time that should be eliminated. Therefore, the current implementation of the platform is illuminated in Figure 4.13, along with the cross section view of urine flow sketched schematically from its entering to until wetting detection region in Figure 4.13c. Noticeably, the noise-canceling dummy photodiode (Section 3.4) has been moved to the PCB (printed circuit board) as a reusable unit which houses all other electronic components and the BLE module. In addition, the urine

collector is not as shown in Figure 4.10 or Figure 4.2, but fluidically the right battery inlet and the strip inlet are bridged. At first sight, it appears that the exposed area is so small such that it is difficult to collect efficiently. However, it only gets rid of the preceding confined filter paper urine collector, which is replaced by diaper acquisition and distribution layer (ADL, Section 4.2) that is not confined and quickly redistributes urine over the diaper. Therefore, urine arrives nearly concurrently at the two spatially neighboring openings (only 9.3 mm apart) in Figure 4.13. Although there might be a little risk that urine doesn't infiltrate the two adjacent openings simultaneously, the fluidic bridge and the fast activation time and moderate duration of the compact 32×22 mm^2 battery guarantee that the design constraints (4-2) and (4-3) hold, which has been experimentally verified at a failure rate <5% for more than 20 tests. For batteries of other dimensions, it may not be universally true and need fine tuning on the sensing strip channel referring to the discussion in the prior section while the activation time and duration of battery are insensitive to its dimension to some degree.
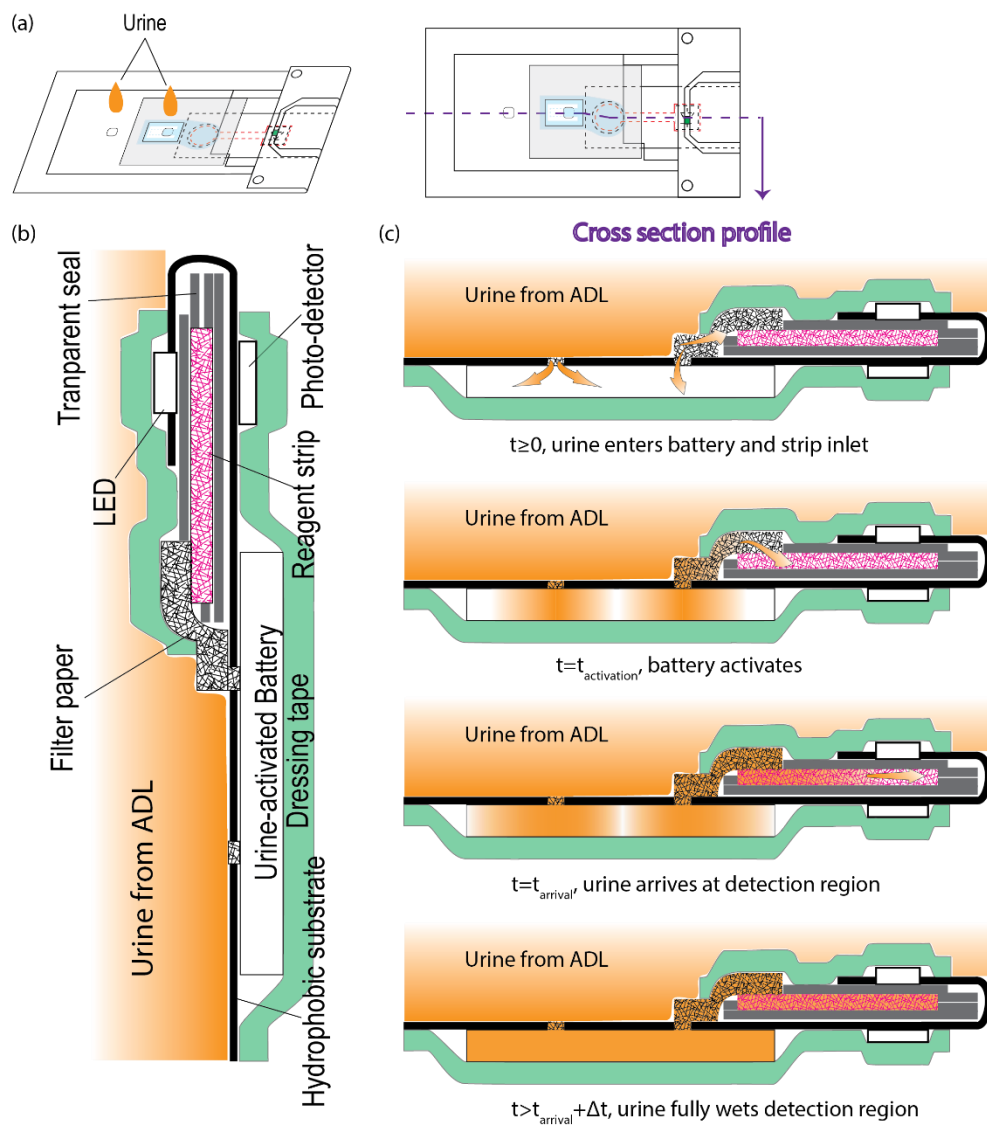
Figure 4.13 Refined design of the sensing platform and schematic snapshots of urine flow in it. (a) perspective view and top view of the refined design with dimensions determined, dummy photodiode transferred and urine collector re-defined; (b) annotations of the components; (c) schematic snapshots of urine flow in the platform.
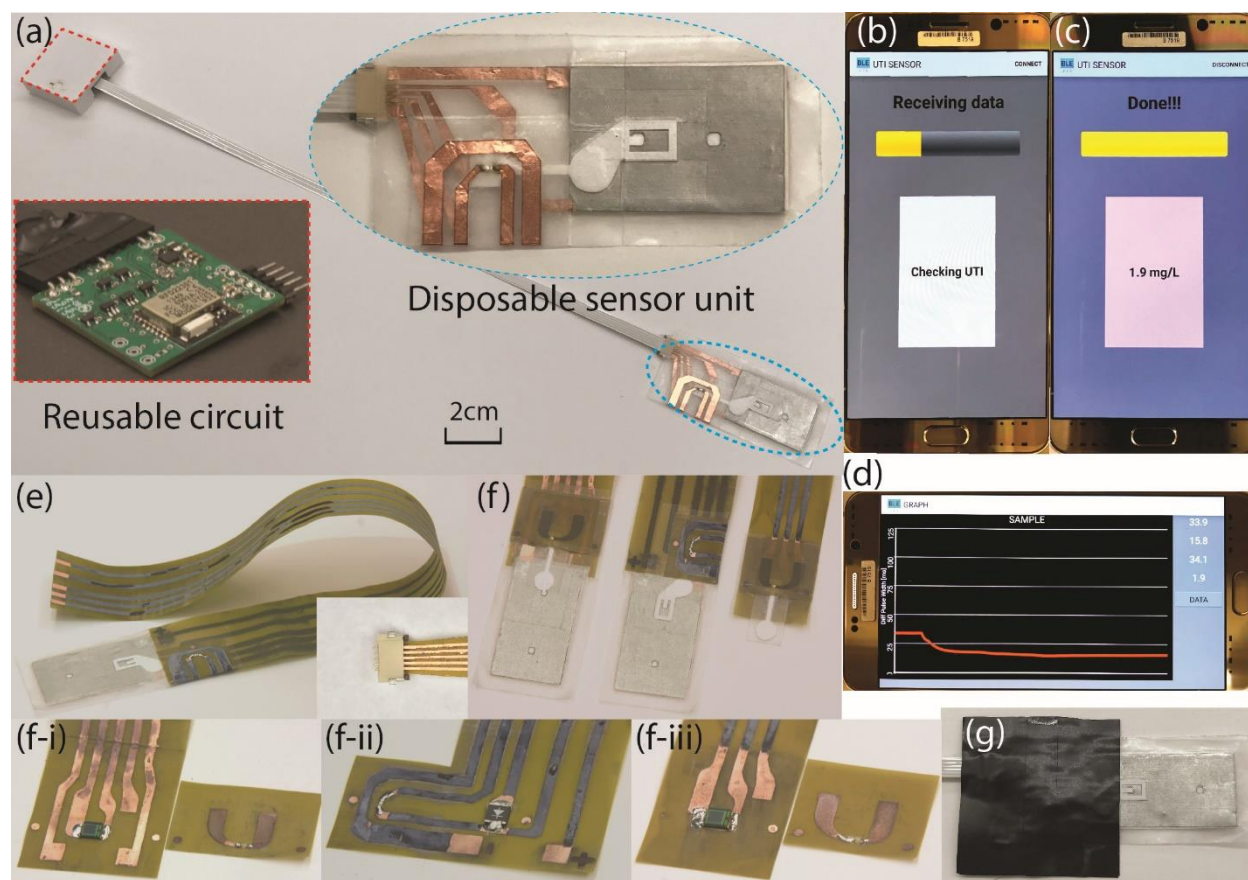
Figure 4.14 Photographs of device prototypes. (a) Disposable sensor module (top inset) and reusable interface and transmitter circuit (bottom inset) connected by a 30 cm long flexible flat cable; (b) software interface for receiving data in measurement; (c) software interface for displaying measurement result in the form of nitrite concentration; (d) software interface showing details of measurement for analysis; (e) A prototype of which the conductive traces are fabricated on wet-etched flexible copper-clad polyimide (100 µm) laminate (DuPont™ Pyralux® AP9141R); inset showing the port end being clipped by a 5-position 1 mm pitch flexible flat cable (FFC) connector; (f) sensor module end made from (f-i) attaching LED layer and photodiode layer using conductive adhesive, (f-ii) folding to align LED and photodiode on the same substrate and (f-iii) removing the urine-activated battery in case of using a commercial battery on the PCB board; (g) black vinyl tape applied surrounding the sensing region to block ambient light.

Photographs of prototypes and software are demonstrated in Figure 4.14. The implementation in Figure 4.14a is adapted to a "7" shape (similar to Figure 4.14f-iii) prior to folding to a rectangle such that a flexible flat cable (FFC) connector could be installed at the shorter edge for hooking a FFC. The folded device has a dimension of 6.7 cm × 3.2 cm and an average thickness <1.7 mm (<2.5 mm at the thickest place). The circuit module including the reference photodiode on a PCB is housed in a 3D printed box for the prevention of environmental light interference. Likewise, the

flexible sensor module should also be protected by black opaque tape such as in Figure 4.14g. Figure 4.14b-c is the illustration of the software user interface for receiving data and indicating measurement results. Figure 4.14d is the plot of recorded and received light absorption measurement over time. As in this example, the dry measurement duration (X-axis value where the curve declines) is about 15.8 s consideration the fact that the entire window spans 170 s, which is in consistency with the estimate, $\Delta t_{dry\_measurement} \approx 13.4 \pm 2.9\ s$. Figure 4.14e-f is manifesting the feasibility of fabricating the circuit traces by wet etching a flexible copper-clad polyimide (100 µm) laminate (DuPont™ Pyralux® AP9141R) while the battery and sensing strip are still on paper substrate before assembly, which might improve the manufacturability of the platform considering that the flexible PCB technology has been industrially well developed. The LED and photodiode can also be soldered onto two separate layers (Figure 4.14f-i) before sandwiching the sensing strip, being fastened and electrically associated by conductive adhesive (for example the above-mentioned transfer tape, 3M 9703). A commercially battery can be seated on the reusable unit with other electronic components, leaving the sensing strip alone in the sensor module (Figure 4.14f-iii), to substitute urine-activated battery in certain settings where other long-term or high-power actions are in need.

Before I bring this subsection to an end, I am going to wrap up with an estimate on the material cost for fabricating the devices. Certainly, manufacturing cost involves direct materials cost, direct labor cost and manufacturing overhead, while here I am only focusing on the first one to my best knowledge. The expenses are based on bulk order pricing from related suppliers if available, summarized in Table 4.1. Hence, the average estimated materials for a single device will be <$2.08, and <$1.30 if the reference photodiode is removed to the reusable module. There are replacements for some parts, some of which are probably even cheaper. For example, substrate may be fabricated using polyethylene sheet (as inexpensive as $0.113/m² for 1 mil thick clear sheet) instead of wax paper. Moreover, the unit costs of dressing tape, zinc and copper tape are all from very small quantity order and thus they should scale down significantly for bulk purchasing, leaving the photodiode the primary limiting factor. The cost of connectors, flexible cable and reusable circuit module along with its housing is not included which is subject to specific choices and requires investigation. If the entire system including all the electronics is desired to be on paper substrate

and disposable, an ASIC chip design is inevitable or the materials cost will go up drastically. However, this involves a different business model, which I won't go further with.

Table 4.1 Raw materials cost estimate summary[12]

Materials (100 devices)	Cost	Materials (100 devices)	Cost
LED	$8.10	Methanol (40ml)	$0.46
Photodiode (2×100)	$156.00	p-Arsanilic acid (400mg)	$0.08
Smith & Nephew OpSite Flexifix Transparent Film (dressing tape, ~0.84 m^2)	$17.67	N-(1-Naphthyl) ethylenediamine dihydrochloride (80mg)	$0.22
Wax paper (~0.66 m^2)	$0.14	CuSO$_4$ (60g)	$2.17
Zinc tape (0.22m^2)	$10.77	KCl (37.25g)	$0.70
Copper tape (0.27 m^2)	$9.59	Total	$208.08
Filter paper (50 pieces, ⌀ 120mm)	$2.18	Total (without reference photodiode)	$130.08

In the next section, I will move on to the discussion over the practical issues about the deployment of the developed sensing platform in a diaper instead of on its own.

4.2 Deployment of the Platform in a Diaper

To make the system work properly, sufficient urine sample need to enter the system inlet to activate the battery and wet the detection region of the reagent strip such that the device is able to take measurements both when the detection region is dry and wet (note that the dry measurement is guaranteed with geometric design of the reagent strip that the battery is activated prior to the arrival of urine to the detection zone). In addition, the battery should be fully activated/wet to last long enough (>2.5 mins) for collecting data points to make a confident decision. A considerable amount of experiments (>30) have shown that 0.6~0.8 ml of water/urine is enough for activating the

---

[12] Electronics prices are based on mouser electronics, chemicals and filter papers are based on VWR, Alfa Aesar or Sigma-Aldrich, zinc tape is from PTR Holland, while others are from Amazon vendors.

system (wetting both the battery and the reagent region) and keeping the device running robustly for at least 6 minutes.

However, when it is in the setting of a real diaper, careful consideration on influence from the complex environment need to be taken for the system, compared to in an ideal case where the urine is dropped right onto the inlet. The schematic composition of a typical diaper is illustrated in Figure 4.15. A diaper or incontinence pad is usually composed of an inner liner, an acquisition distribution layer, an absorbent core and a backsheet. The inner liner sheet is usually made of non-woven polypropylene to provide a soft and uniform surface for skin contact. Beneath the inner cover is an acquisition and distribution layer (ADL), which is also typically a non-woven fabric of excellent hydrophilic property for improving fluid distribution over the absorbent core, sodium polyacrylate powder or fluff. The back sheet or outer cover is usually a layer of polyethylene film that is breathable but impervious to urine for leakage protection. [86] As regards the integration of the device into a diaper, the first question is which layer the device should be resting on. Laying above the inner lining sheet is not recommended, which introduces discomforts and needs additional mechanism to guarantee that urine enters the device. Depositing it on the ADL layer is not feasible either since urine will find it difficult to locate the device entrance without liquid redistribution. It is also obviously not wise to place the device below the back sheet given that it is leakproof. Therefore, for the purpose of ensuring the sampling of urine, it is better to put the device between the ADL layer and absorbent core layer or under the absorbent core layer as exemplified in Figure 4.16.
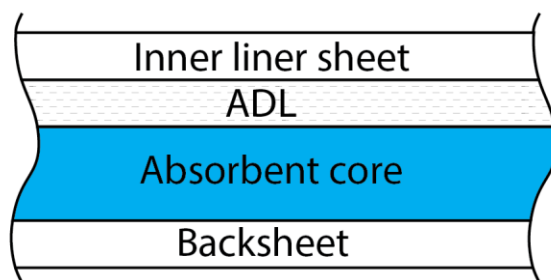
Figure 4.15 Cross section of diaper schematic structure
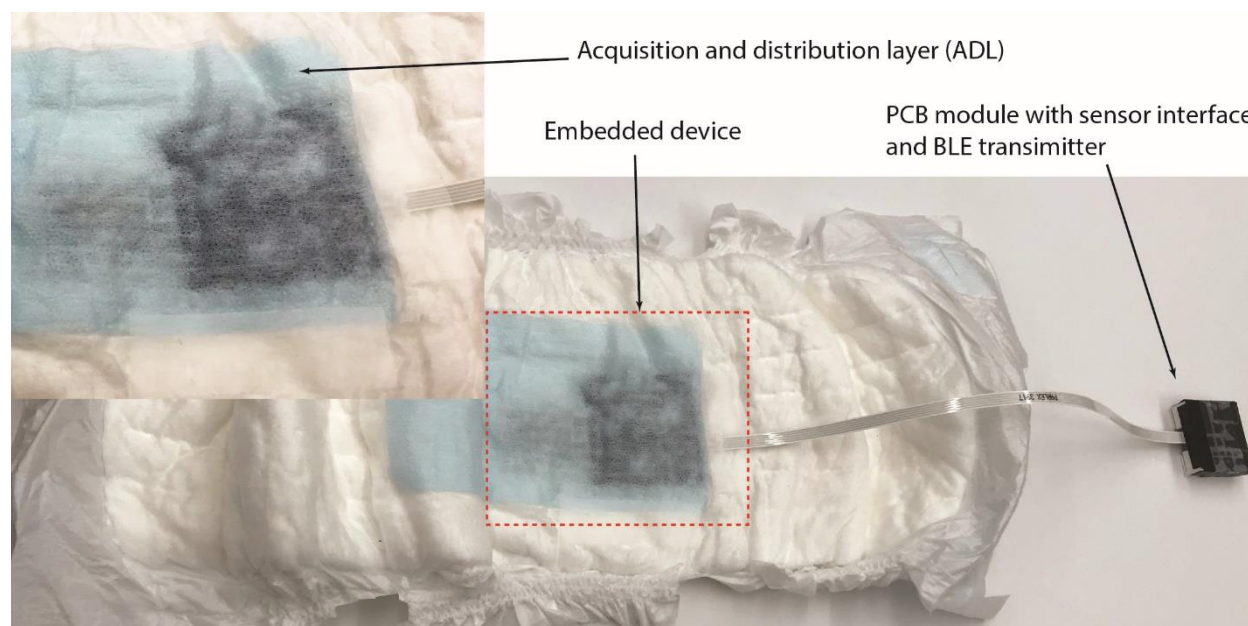
Figure 4.16 Embedding arrangement for the sensing platform

There are still concerns on how much fluid is needed to activate the electronic urinalysis system if it is integrated under the super absorbent layer, especially in an adult diaper. An adult incontinence shield may have various load capacities from 1.5 ~ 3 L [87], while the average urine volume per void is around 237ml for men [88] and similarly 257ml in women [89]. Moreover, the voiding volume decreases with age [89, 90], which might go down to 172 ml [90]. Apparently, the diaper loading capacity is designed to hold its wearer's each voided urine in most cases. Thus, it is risky for the device to catch every urination activity if it lies under the absorbent core, which is not desirable. The most significant difference in a diaper is that the device must compete with other hydrophilic materials (non-woven fabric, sodium polyacrylate fluff, etc.) to absorb urine, and that urine won't stay on the device inlet for as long as in an ideal case (standalone device positioned horizontally), no matter which layer it goes in. Experiments to quantify this influence are presented as follows.

4.2.1 Influence on activation of paper battery

Considering that the battery ($32\times22\times2$ mm^2 active area, 2-layer filter paper) needs much more urine than the detection strip (~82 mm^2, <6% of the battery urine absorption capacity), the experiments focus on the activation of batteries only. Figure 4.17a-b demonstrates the

configuration of the device being inserted between inner sheet and ADL layer. Without loss of generality, the batteries under test are 24×24 mm^2 in dimension, along with a 2×2 mm^2 inlet in the center. To activate the battery, 100 ml water is poured on top of the diaper inner sheet at a flow rate of 10~20 ml/s, which is similar to normal urination rate [91], and the output of the battery is monitored continuously with a voltmeter while being connected to a ~30 Ω load. Results in 4 different scenarios are presented in Table 4.2. In addition to embedding position in the diaper (Kroger Moderate Absorbency Belted Shields), two different packaging designs are also explored as depicted in Figure 4.17c-d: one with transport path exposed atop the battery electrolyte reservoir orifice, while the other has a waterproof tape covering the area above the battery reservoir orifice, making it around 5 mm away from the tape opening.
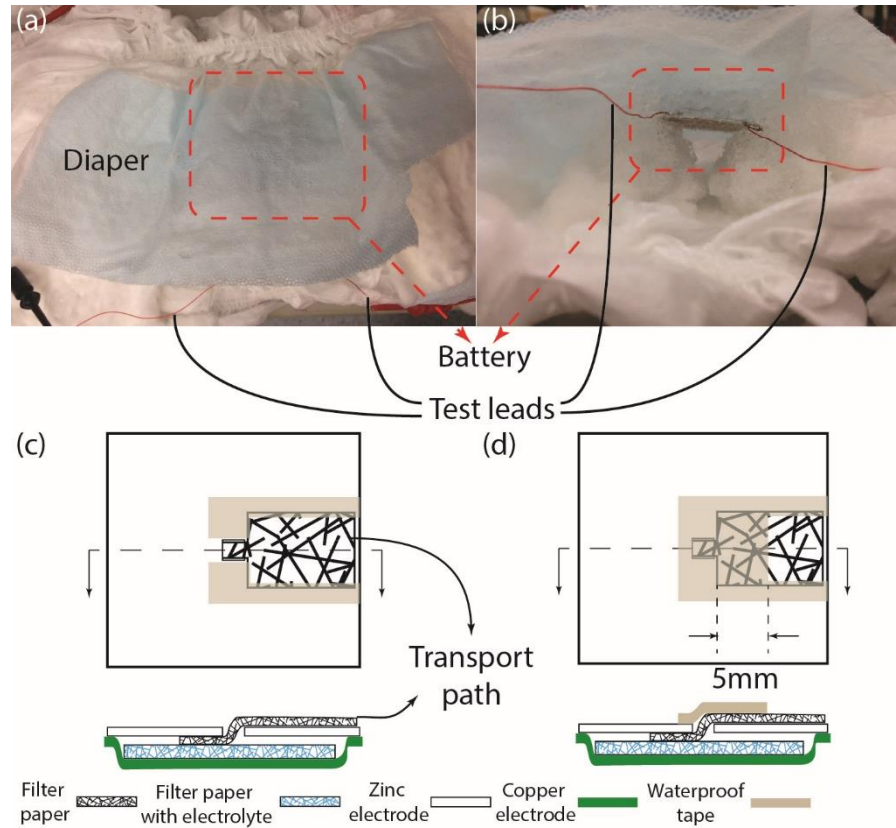

Figure 4.17 Experimental setup: (a) front view; (b) lateral view. Battery packaging design under diaper-embedded test: (c) exposed – transport path is exposed above the battery inlet; (d) covered – waterproof tape covering atop the battery inlet.

Table 4.2 Diaper-embedded paper battery test results

Activation time Duration	Exposed	Covered
Between ADL and absorbent core	<10 sec	Not activated
	6 min	
Beneath absorbent core	~10 sec	Not activated
	2 min	

In Table 4.2, "activation time" is the delay from the beginning of pouring water to the diaper inner sheet to the moment the battery output voltage rises up to larger than 0.84 V (adequate power the whole platform, Section 4.1.2), and "duration" is how long the battery stays above this level. It is obvious from the results that this urinalysis platform has a better reliability embedded in the diaper when it is placed between ADL and absorbent core and its battery inlet region is exposed for urine collection. The "covered" batteries could not be activated (or power level not exceeding the desired threshold, 8 mA) in either embedding scheme, and the "exposed" battery beneath absorbent core could not keep a considerable power output for long. The cause behind is essentially the same that not enough water enters the battery electrolyte reservoir before they are stolen by super-absorbent materials surrounding the device. In other words, it is recommended that the urine transport path be designed and the device be integrated in the diaper such that battery electrolyte reservoir gets saturated with urine as easily as possible in competence with other liquid-absorbent materials in the diaper. The straightforward solution is to make the route, that urine travels along from upon contact with the diaper inner sheet to the battery inlet, as short as possible (placing the device above instead of under absorbent core and exposing battery inlet upper area), and to make urine flow rate in the route as large as possible (tape adhesive surface is one of the impeding factors on the flow rate).

Generally speaking, a urine transport path with larger contact area for urine collection in the diaper and a bigger battery inlet would also help improve the system reliability. However, a bigger battery inlet might bring side effects under current device layout, like rapid battery electrolyte reflux out of reservoir and effective electrode area reduction. Furthermore, some may still be worried about

any potential hazards when the device is deployed too close to skin. One promising solution is creating a long but large urine transport path so that the device can be attached at the far end of the diaper while a large urine collecting pad is fixed underneath the diaper inner sheet, Figure 4.18. Importantly, the inner surface of the package for the urine transport path is better to be hydrophobic to conduct the urine at a fast rate. For instance, the urine travels faster when the filter paper is packaged with Scotch tape/wax paper other than Scotch tape/Scotch tape.
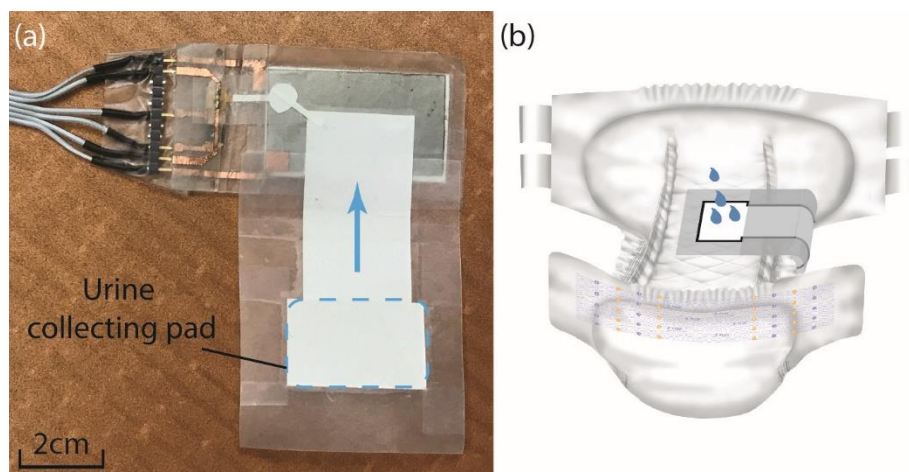
Figure 4.18 (a) Prototype photograph of a urinalysis sensing platform with a long and bendable urine transport path; (b) Schematic of bending the long transport path for device integration with a diaper.

4.2.2 Influence on the color change in the detection region

Even though the influence of device embedding position in a diaper is negligible on reliably infusing urine into the detection region on the strip, water potential (relative potential energy of water per unit volume [92]) is different for the matrix contacting the device inlet when it is placed above the absorbent core other than under it, which is mainly ascribed to different material capillary properties of ADL layer (fabric) and absorbent core (sodium polyacrylate fluff) in a diaper, thus affecting urine loading/saturation level within the reagent strip. It is expected that, the detection region is prone to getting soaked with more urine across the thickness of a packaged strip (or equivalently urine with larger effective depth for light to pass) when it is above the absorbent core, while ideally urine should replace all the air in the reagent strip especially in the detection region, given that urine with biomarker-responsive color change contributes to the wanted light absorption signal rather than the cellulose paper matrix to noise. As a Figure 4.19 shows the

photographs of reagent strip color change with its entrance exposed directly to 30 µL 1 ppm nitrite solution atop (the strip on the left in Figure 4.19) and covered by a 3cm×3cm piece cut from the diaper in Figure 4.17 before applying 10 ml 1 ppm nitrite solution (the strip on the right in Figure 4.19, diaper fragment removed), respectively. Although the color change discrepancy is not very visually significant between them, a careful inspection within the detection region could still reveal that the strip on the left is loaded with more nitrite solution than the right one, which can be quantified by light absorption measurement. Nevertheless, the offset in urine loading level should be calibratable to some extent, but it is suggested that the device be integrated right underneath the diaper ADL layer and above the absorbent core to minimize its susceptibility to urine amount.
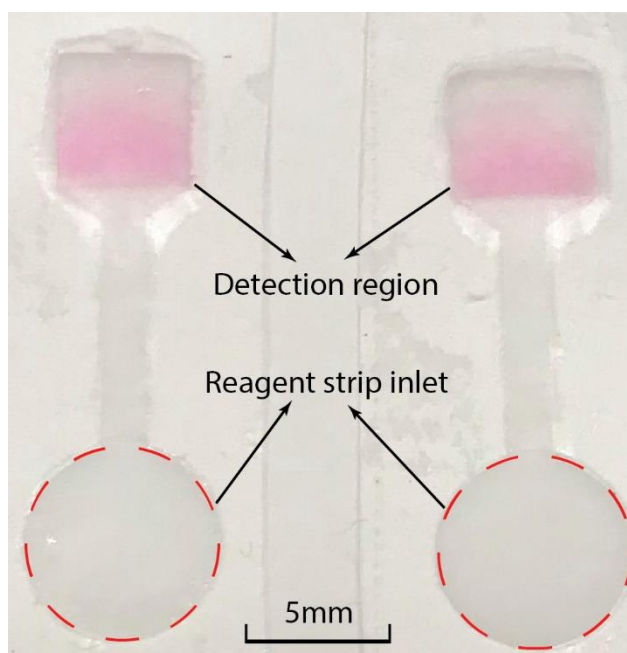
Figure 4.19 photographs of reagent strip color change: (left) inlet exposed directly to 30 µL 1 ppm nitrite solution atop; (right) inlet covered by a 3cm×3cm piece cut from the diaper in Figure 4.3 before applying 10 ml 1 ppm nitrite solution.

4.2.3 Experimental results of diaper-embedded platform
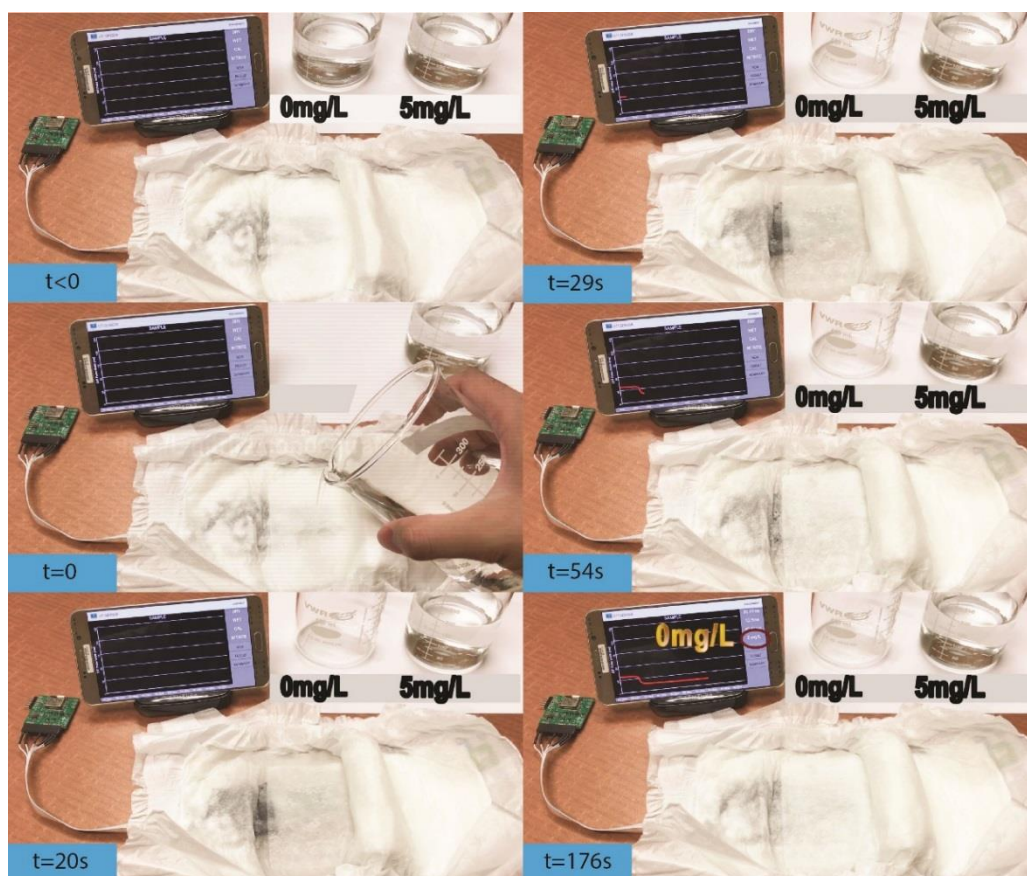
Figure 4.20 Snapshots of diaper-embedded test of integrated platform
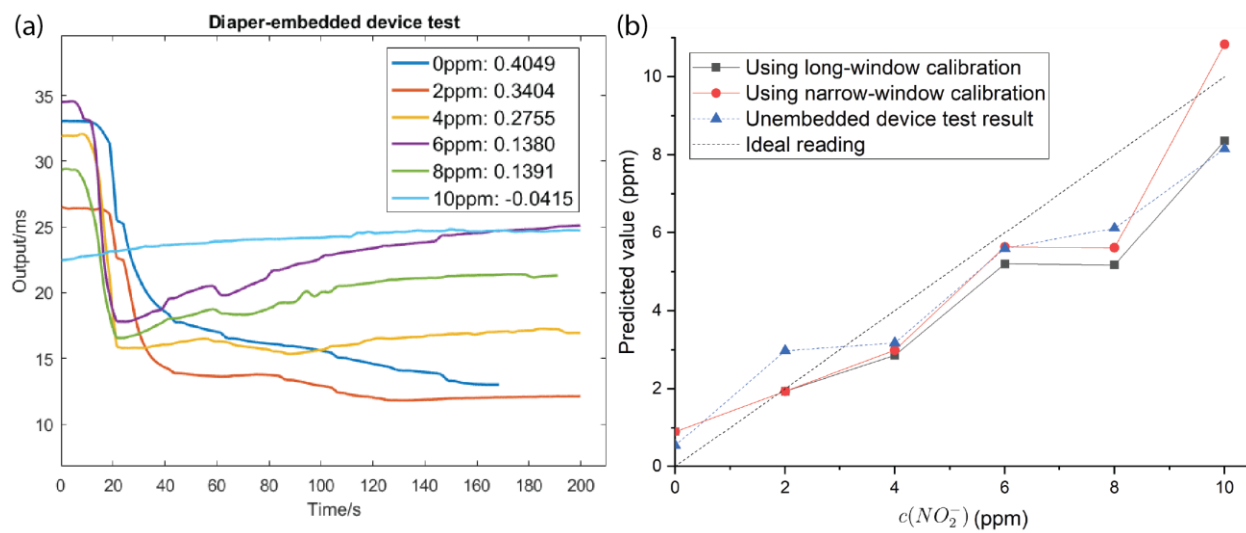
Figure 4.21 (a) Diaper-embedded test time series plot. (b) Sensor prediction results

$$\sigma_{est} = 1.834,\ 1.448$$

4.3 Comparison with other relevant systems
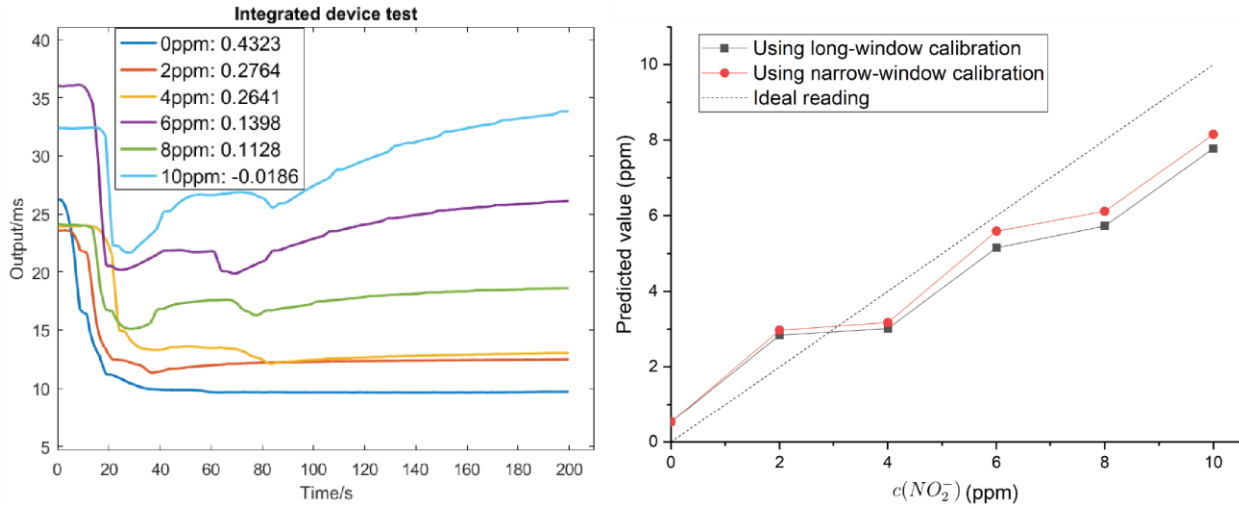
Figure 4.22 (a) Integrated device test time series plot. (b) Sensor prediction results

Mean Prediction error:

$$\sigma_{est} = \sqrt{\frac{\sum (Y - Y')^2}{N}} = 1.4579,\ 1.2267$$
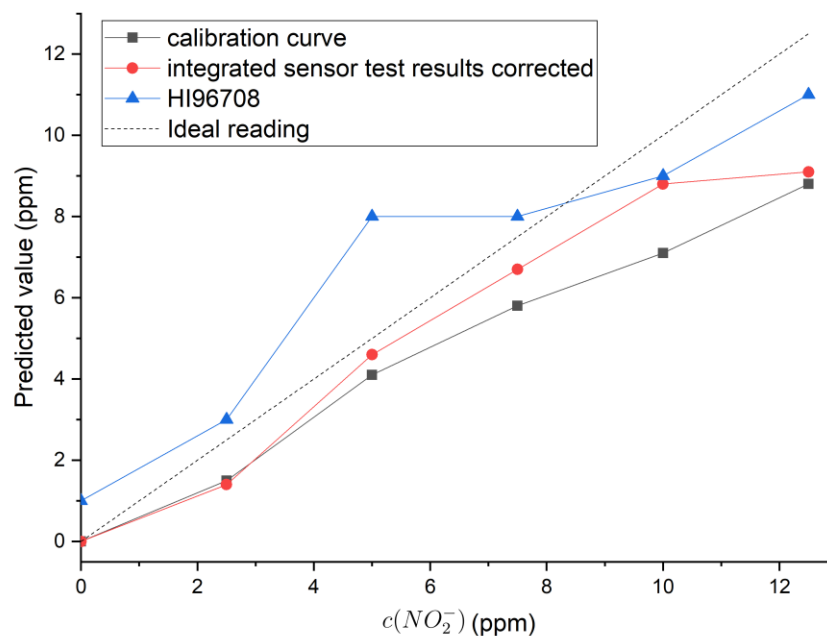
Figure 4.23 Integrated platform sensor test in comparison to commercial nitrite sensor

Table 4.3 Integrated platform sensor test in comparison to commercial nitrite sensors

Nitrite [ppm]	0	2.5	5	7.5	10	12.5	σ_{est}
Calibration curve [ppm]	0	1.5	4.1	5.8	7.1	8.8	1.81
Corrected curve [ppm]	0	1.4	4.6	6.7	8.8	9.1	0.93
HI96708 (High Range) [ppm]	1	3	8	8	9	11	1.62
HI-764 (Low Range)[ppm]	0.013						N/A
Dipstick	-	+	+	+	+	+	N/A

Table 4.4 Platform performance in comparison to other relevant products

	This work	Dipstick	Camera-assisted color analysis*
Lower detection limit	<0.6 ppm	0.5 ppm	0.5 ppm
User Intervention	None	Collect urine sample; dip; read color chart in 2 minutes	Timely photographing is necessary; need urination alerting; affected by alignment and illumination
Production Cost	Low	Very low	Low

Both collected urine and the dipsticks are time-sensitive and test has to be processed timely to be diagnostically significant. (Urine: tested within 2 hours of urination. Dipstick: read in 1-2 minutes (Most Griess test protocol suggest within 30 minutes))

CHAPTER 5.   CONCLUSIONS

In this contribution, my collaborators and I developed an inexpensive autonomous diaper-embedded urinary diseases sensing platform, as an early screening alternative to dipstick test. The platform can be a thin and conformal add-on into a diaper such that it doesn't cause discomfort.

CHAPTER 6.   FUTURE DIRECTIONS

6.1   A Multi-Parameter Sensing Platform

6.1.1   Urinary Red Blood Cell Sensing

The excretion of red blood cells in the urine (or hematuria) may be related to UTI, kidney disease, kidney stones or tumors. [1] These diseases are serious and require further diagnosis and treatment. Blood test is already widely implemented in dipstick technology, which might be compatible with the system proposed herein. The test is mostly based on the hemoglobin or myoglobin catalyzing the oxidation of a certain color indicator (for example 3,3',5,5'-Tetramethylbenzidine (TMB)) by an organic hydroperoxide (such as 2,5-dimethylhexane-2,5-dihydroperoxide). [1] Upon the oxidation, TMB changes color from greenish-yellow to greenish-blue and then to dark blue. In this scenario, a LED/photodiode module in the wavelength range of 600~700nm (red) would be appropriate for the absorbance measurement.
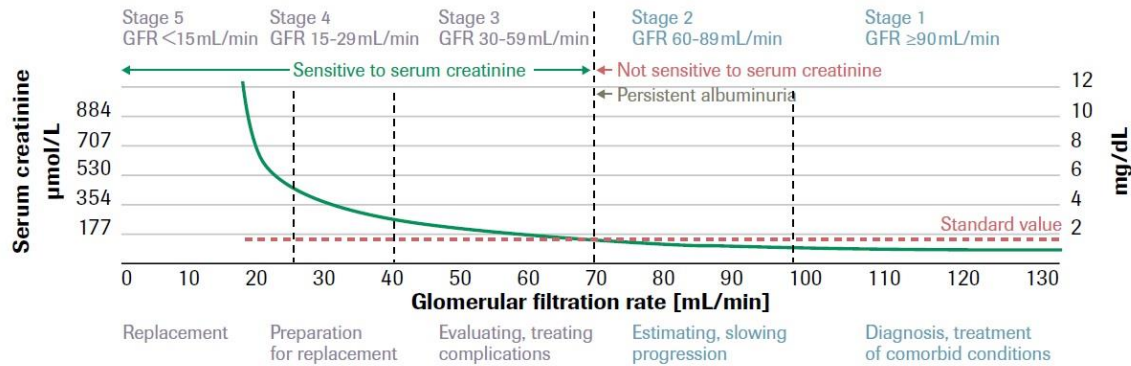
Figure 4.2 Glomerular filtration rate in correlation with CKD [1]

6.1.2   Urinary Protein or Albumin Sensing

Proteinuria refers to a condition in which there is an abnormal (usually excessive) amount of protein. It usually occurs with renal diseases, with which the patients have impaired glomerular filtration or tubular reabsorption. In the scenarios related to chronic renal diseases, symptoms often occur late or not at all while proteinuria or albuminuria is usually one of the earliest premonition, as in Figure 4.2 [1]. Older aged group (using diapers) is riskier to develop CKD compared with ordinary adults. If not treated timely and effectively, CKD can lead to kidney failure. In the

abnormal excretion of proteins, albumin takes up the largest proportion. [93] Therefore, we can choose albumin-specific colorimetric assay as the test for proteinuria or albuminuria.

Two broadly employed sulfonphthalein dyes in dipsticks are tetrabromophenol blue (TBPB, for total protein test) and 5', 5"- dinotro-3', 3"- diiodo-3,4,5,6-tetrobromophenolsulfonephthalein (DIDNTB, higher sensitivity and specificity for albumin [94]). Both of them can be measured on absorbance around the wavelength of 610 nm [94], with the color change from yellow to green in the presence of protein (albumin). Even though proteinuria is non-specific to nephropathy, it is better to aim at a detection threshold of 0.1 mg/mL for total protein assay or 0.02mg/ml for microalbuminuria [1].
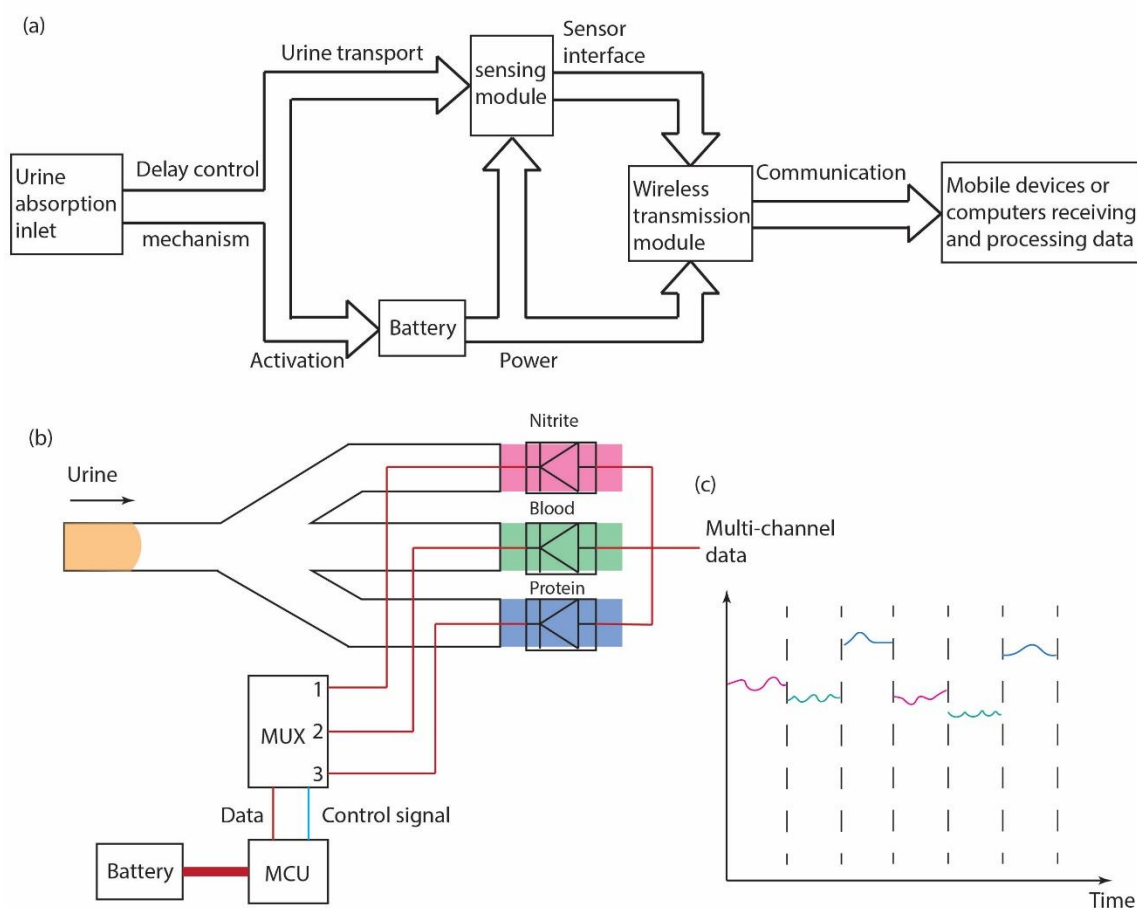
Figure 4.3 Multi-parameter sensing platform diagram. (a) System block architecture. (b) Microcontroller controlled multichannel chemical sensing scheme. (c) Multi-channel data transmission.

6.1.3 Development a multi-parameter sensing platform

A platform integrating more than just one parameter sensing mechanism is greatly advantageous, since multi-parameter diagnostic rules can improve substantially the sensitivity (how many positives can be screened out of the total positives, against false negative) without the expense of losing too much specificity (how many negatives can be correctly screened out of the total negatives, against false positive). [9, 10, 45]

I propose to incorporate a multiplexer, which can be controlled by the microcontroller that is integrated in the UTI sensing module, to periodically switch the signal channel for respective parameter sensing (e.g. nitrite, red blood cells, protein, etc.), as illustrated in Figure 4.3. In this manner, the collected data within the time window of diagnostic interest will be a multi-channel signal as shown in Figure 4.3c. This signal, which is later received wirelessly, can be decoded into multiple different signals corresponding to separate single parameters based on the known programmed timing protocol in the diaper-embedded microcontroller, and interpreted into intelligible diagnostic values on the mobile terminal or station.

REFERENCES

[1] E. F. Hohenberger and H. Kimling, "Compendium urinalysis: urinalysis with test strips," Roche Diagnostics, Germany, 2008.

[2] A. L. Flores-Mireles, J. N. Walker, M. Caparon and S. J. Hultgren, "Urinary tract infections: epidemiology, mechanisms of infection and treatment options," *Nature reviews microbiology,* vol. 13, no. 5, pp. 269-284, 2015.

[3] "2015 Kidney Disease Statistcs," 12 February 2016. [Online]. Available: http://www.kidneyfund.org/assets/pdf/kidney-disease-statistics.pdf. [Accessed 8 November 2016].

[4] "WHO | Diabetes Programme," World Health Organization, 2016. [Online]. Available: http://www.who.int/diabetes/en/. [Accessed 8 November 2016].

[5] M. Ratini, "Urine: Color, Odor, and Your Health," WebMD, 01 February 2016. [Online]. Available: http://www.webmd.com/urinary-incontinence-oab/truth-about-urine. [Accessed 13 November 2016].

[6] R. Mammadli, "Human Urine Color Meaning," Health Recovery Tips, 10 August 2016. [Online]. Available: http://iytmed.com/urine-color-meaning/. [Accessed 3 July 2018].

[7] E. V. Lerma and M. H. Rosner, "Urinalysis," in *Nephrology Secrets, 3rd Edition.*, Philadelphia, Elsevier Mosby, 2012, pp. 14-25.

[8] "Urinalysis: Three Types of Examinations - The Microscopic Examination," Lab Tests Online, 25 May 2016. [Online]. Available: https://labtestsonline.org/understanding/analytes/urinalysis/ui-exams?start=2. [Accessed 13 November 2016].

[9] R. V. Sultana, S. Zalstein, P. Cameron and D. Campbell, "Dipstick urinalysis and the accuracy of the clinical diagnosis of urinary tract infection," *The Journal of emergency medicine,* vol. 20, no. 1, pp. 13-19, 2001.

[10] H. Semeniuk and D. Church, "Evaluation of the leukocyte esterase and nitrite urine dipstick screening tests for detection of bacteriuria in women with suspected uncomplicated urinary tract infections," *Journal of clinical microbiology,* vol. 37, no. 9, pp. 3051-3052, 1999.

[11] R. K. Ditchburn and J. S. Ditchburn, "A study of microscopical and chemical tests for the rapid diagnosis of urinary tract infections in general practice," *Br J Gen Pract,* vol. 40, no. 339, pp. 406-408, 1990.

[12] A. Rabinovitch, "Urinalysis–approved guideline," in *CLSI document 29.4*, 2009, pp. 11-21.

[13] S. M. Schappert and E. A. Rechtsteiner, "Ambulatory medical care utilization estimates for 2007," *Vital Health Stat,* vol. 13, no. 169, pp. 1-38, 2011.

[14] S. Salvatore, S. Salvatore, E. Cattoni, G. Siesto, M. Serati, P. Sorice and M. Torella, "Urinary tract infections in women," *European Journal of Obstetrics & Gynecology and Reproductive Biology,* vol. 156, no. 2, pp. 131-136, 2011.

[15] P. Rui and K. Kang, "National Hospital Ambulatory Medical Care Survey: 2015 Emergency Department Summary Tables," Centers for Disease Control and Prevention, 2015.

[16] B. Foxman, "Epidemiology of urinary tract infections: incidence, morbidity, and economic costs," *The American journal of medicine,* vol. 113, no. 1, pp. 5-13, 2002.

[17] B. Wettergren, U. Jodal and G. Jonasson, "Epidemiology of bacteriuria during the first year of life," *Acta Paediatrica,* vol. 74, no. 6, pp. 925-933, 1985.

[18] C. Chen and T. Dong, "Microfluidic paper-based analytical devices for colorimetric detection of urinary tract infection biomarkers on adult diapers," in *37th Annual International Conference of the IEEE Engineering in Medicine and Biology Society (EMBC)*, Milan, Italy, 2015.

[19] J. B. Fox, "Kinetics and mechanisms of the Griess reaction," *Analytical Chemistry,* vol. 51, no. 9, pp. 1493-1502, 1979.

[20] M. Armand and J. M. Tarascon, "Building better batteries," *Nature,* vol. 451, no. 7179, pp. 652-657, 2008.

[21] A. Martinez, S. Phillips, M. Butte and G. Whitesides, "Patterned paper as a platform for inexpensive, low-volume, portable bioassays," *Angew. Chemie - Int. Ed.,* vol. 46, pp. 1318-1320, 2007.

[22] Y. Lu, W. Shi, L. Jiang, J. Qin and B. Lin, "Rapid prototyping of paper-based microfluidics with wax for low-cost, portable bioassay," *Electrophoresis,* vol. 30, no. 9, p. 1497–500, 2009.

[23] K. Abe, K. Suzuki and D. Citterio, "Inkjet-printed microfluidic multianalyte chemical sensing paper," *Anal. Chem.,* vol. 80, pp. 6928-6934, 2008.

[24] G. Chitnis, Z. Ding, C. Chang, C. Savran and B. Ziaie, "Laser-treated hydrophobic paper: an inexpensive microfluidic platform," *Lab on a Chip,* vol. 11, p. 1161–1165, 2011.

[25] A. K. Yetisen, M. S. Akram and C. R. Lowe, "Paper-based microfluidic point-of-care diagnostic devices," *Lab on a Chip,* vol. 13, no. 12, pp. 2210-2251, 2013.

[26] E. Fortunato, N. Correia, P. Barquinha, L. Pereira, G. Goncalves and R. Martins, "High-performance flexible hybrid field-effect transistors based on cellulose fiber paper," *IEEE Electron Device Lett.,* vol. 29, p. 988–990, 2008.

[27] B. Lamprecht, R. Thünauer, M. Ostermann, G. Jakopic and G. Leising, "Organic photodiodes on newspaper," *physica status solidi (a),* vol. 202, no. 5, pp. R50-R52, 2005.

[28] A. J. Steckl, "Circuits on cellulose," *IEEE Spectrum,* vol. 50, no. 2, pp. 48-61, 2013.

[29] T. H. Nguyen, A. Fraiwan and S. Choi, "Paper-based batteries: a review.," *Biosensors and Bioelectronics,* vol. 54, pp. 640-649, 2014.

[30] K. Lee, "Urine-activated paper batteries for biosystems," *Journal of Micromechanics and Microengineering,* vol. 15, no. 9, p. S210, 2005.

[31] N. K. Thom, K. Yeung, M. B. Pillion and S. T. Phillips, "Fluidic batteries' as low-cost sources of power in paper-based microfluidic devices," *Lab on a Chip,* vol. 12, no. 10, pp. 1768-1770, 2012.

[32] S. S. Chen, C. W. Hu, I. F. Yu, Y. C. Liao and J. T. Yang, "Origami paper-based fluidic batteries for portable electrophoretic devices," *Lab on a Chip,* vol. 14, no. 12, pp. 2124-2130, 2014.

[33] L. Zhang, M. Zhou, D. Wen, L. Bai, B. Lou and S. Dong, "Small-size biofuel cell on paper," *Biosensors and Bioelectronics,* vol. 35, no. 1, pp. 155-159, 2012.

[34] A. Fraiwan, S. Mukherjee, S. Sundermier, H. S. Lee and S. Choi, "A paper-based microbial fuel cell: Instant battery for disposable diagnostic devices," *Biosensors and bioelectronics,* vol. 49, pp. 410-414, 2013.

[35] L. Hu, H. Wu, F. La Mantia, Y. Yang and Y. Cui, "Thin, flexible secondary Li-ion paper batteries," *Acs Nano,* vol. 4, no. 10, pp. 5843-5848, 2010.

[36] X. Zhang, Z. Lin, B. Chen, S. Sharma, C. P. Wong, W. Zhang and Y. Deng, "Solid-state, flexible, high strength paper-based supercapacitors," *Journal of Materials Chemistry A,* vol. 1, no. 19, pp. 5835-5839, 2013.

[37] H. Gräfen, E. Horn, H. Schlecker and H. Schindler, "Corrosion," in *Ullmann's Encyclopedia of Industrial Chemistry, 6th Edition*, Wiley, 2000.

[38] A. Covington, "Activity coefficients - Kaye & Laby," National Physical Laboratory, 2017. [Online]. Available: http://www.kayelaby.npl.co.uk/chemistry/3_9/3_9_6.html. [Accessed 6 June 2018].

[39] P. Vanýsek, "Electrochemical Series," in *CRC Handbook of Chemistry and Physics, 93rd Edition*, CRC Press, 2012, pp. 5-80.

[40] P. C. Pandey, G. Singh and P. K. Srivastava, "Electrochemical synthesis of tetraphenylborate doped polypyrrole and its applications in designing a novel zinc and potassium ion sensor," *Electroanalysis: An International Journal Devoted to Fundamental and Practical Aspects of Electroanalysis,* vol. 14, no. 6, pp. 427-432, 2002.

[41] N. Perez, "Mixed Potential Theory," in *Electrochemistry and Corrosion Science*, Boston, MA, Springer, 2004, pp. 155-166.

[42] C. Wan, H. Cheh and H. Linford, "A study of electrochemical kinetics of copper deposition under pulsed current conditions," *Journal of applied electrochemistry,* vol. 9, no. 1, pp. 29-35, 1979.

[43] J. Bockris, M. Devanathan and K. Müller, "On the structure of charged interfaces," *Proc. R. Soc. Lond. A,* vol. 274, no. 1356, pp. 55-79, 1963.

[44] T. I. Quickenden and X. Jiang, "The diffusion coefficient of copper sulphate in aqueous solution," *Electrochimica acta,* vol. 29, no. 6, pp. 693-700, 1984.

[45] P. Little, S. Turner, K. Rumsby, G. Warner, M. Moore, J. Lowes, H. Smith, C. Hawke and M. Mullee, "Developing clinical rules to predict urinary tract infection in primary care settings: sensitivity and specificity of near patient tests (dipsticks) and clinical scores," *Br J Gen Pract,* vol. 56, no. 529, pp. 606-612, 2006.

[46] R. Orenstein and E. S. Wong, "Urinary tract infections in adults," *American family physician,* vol. 59, no. 5, pp. 1225-34, 1999.

[47] P. Griess, "Griess Reagent: A Solution of Sulphanilic Acid and A-Naphthylamine in Acetic Acid Which Gives a Pink Colour on Reaction with the Solution Obtained after Decomposition of Nitrosyl Complexes.," *Chem. Ber,* vol. 12, p. 427, 1879.

[48] L. G. SMITH, W. R. THAYER, E. M. MALTA and J. P. UTZ, "Relationship of the Griess nitrite test to bacterial culture in the diagnosis of urinary tract infection," *Annals of Internal Medicine,* vol. 54, no. 1, pp. 66-72, 1961.

[49] A. W. Czerwinski, R. G. Wilkerson, J. A. Merrill, B. Braden and J. P. Colmore, "Further evaluation of the Griess test to detect significant bacteriuria: Part II.," *American journal of obstetrics and gynecology,* vol. 110, no. 5, pp. 677-681, 1971.

[50] J. Dutt and J. Davis, "Current strategies in nitrite detection and their application to field," *Journal of Environmental Monitoring,* vol. 4, no. 3, pp. 465-471, 2002.

[51] Y. Zhao, D. Zhao and D. Li, "Electrochemical and other methods for detection and determination of dissolved nitrite: a review.," *Int. J. Electrochem. Sci,* vol. 10, pp. 1144-1168, 2015.

[52] N. Lopez-Ruiz, V. F. Curto, M. M. Erenas, F. Benito-Lopez, D. Diamond, A. J. Palma and L. F. Capitan-Vallvey, "Smartphone-based simultaneous pH and nitrite colorimetric determination for paper microfluidic devices," *Analytical chemistry,* vol. 86, no. 19, pp. 9554-62, 2014.

[53] V. J. Sieben, C. F. Floquet, I. R. Ogilvie, M. C. Mowlem and H. Morgan, "Microfluidic colourimetric chemical analysis system: Application to nitrite detection," *Analytical Methods,* vol. 2, no. 5, pp. 484-491, 2010.

[54] J. D. Peele, R. H. Gadsden and R. Crews, "Semi-automated vs. visual reading of urinalysis dipsticks," *Clinical chemistry,* vol. 23, no. 12, pp. 2242-2246, 1977.

[55] J. R. Askim and K. S. Suslick, "Hand-held reader for colorimetric sensor arrays," *Analytical chemistry,* vol. 87, no. 15, pp. 7810-6, 2015.

[56] M. Badea, A. Amine, G. Palleschi, D. Moscone, G. Volpe and A. Curulli, "New electrochemical sensors for detection of nitrites and nitrates," *Journal of Electroanalytical Chemistry,* vol. 509, no. 1, pp. 66-72, 2001.

[57] J. Davis, M. J. Moorcroft, S. J. Wilkins, R. G. Compton and M. F. Cardosi, "Electrochemical detection of nitrate and nitrite at a copper modified electrode," *Analyst,* vol. 125, no. 4, pp. 737-742, 2000.

[58] J. Davis and R. G. Compton, "Sonoelectrochemically enhanced nitrite detection," *Analytica Chimica Acta,* vol. 404, no. 2, pp. 241-247, 2000.

[59] B. Néel, M. Ghahraman Asfhar, G. A. Crespo, M. Pawlak, D. Dorokhin and E. Bakker, "Nitrite- Selective Electrode Based On Cobalt (II) tert- Butyl- Salophen Ionophore," *Electroanalysis,* vol. 26, no. 3, pp. 473-480, 2014.

[60] R. G. V. K. &. K. A. Prasad, "Metallo-tetraazaporphyrin based anion sensors: regulation of sensor characteristics through central metal ion coordination," *Analytica Chimica Acta,* vol. 508, no. 1, pp. 61-70, 2004.

[61] S. S. Hassan, S. A. Marzouk and H. E. Sayour, "Selective potentiometric determination of nitrite ion using a novel (4-sulphophenylazo-) 1-naphthylamine membrane sensor," *Talanta,* vol. 59, no. 6, pp. 1237-1244, 2003.

[62] E. Malinowska and M. E. Meyerhoff, "Role of axial ligation on potentiometric response of Co (III) tetraphenylporphyrin-doped polymeric membranes to nitrite ions," *Analytica chimica acta,* vol. 300, no. 1, pp. 33-43, 1995.

[63] A. Zazoua, C. Dernane, I. Kazane, M. Belghobsi, A. Errachid and N. Jaffrezic-Renault, "Gold electrode functionalized with catalase for impedimetric detection of nitrite," *Sensor Letters,* vol. 9, no. 6, pp. 2283-2286, 2011.

[64] H. Wang, W. Yang, S. C. Liang, Z. M. Zhang and H. S. Zhang, "Spectrofluorimetric determination of nitrite with 5, 6-diamino-1, 3-naphthalene disulfonic acid," *Analytica chimica acta,* vol. 419, no. 2, pp. 169-173, 2000.

[65] M. Yaqoob, B. Folgado Biot, A. Nabi and P. J. Worsfold, "Determination of nitrate and nitrite in freshwaters using flow-injection with luminol chemiluminescence detection," *Luminescence,* vol. 27, no. 5, pp. 419-425, 2012.

[66] K. Zhang, Y. Hu and G. Li, "Diazotization-coupling reaction-based selective determination of nitrite in complex samples using shell-isolated nanoparticle-enhanced Raman spectroscopy," *Talanta,* vol. 116, pp. 712-718, 2013.

[67] L. W. Gapper, B. Y. Fong, D. E. Otter, H. E. Indyk and D. C. Woollard, "Determination of nitrite and nitrate in dairy products by ion exchange LC with spectrophotometric detection," *International dairy journal,* vol. 14, no. 10, pp. 881-887, 2004.

[68] D. Connolly and B. Paull, "Rapid determination of nitrate and nitrite in drinking water samples using ion-interaction liquid chromatography," *Analytica Chimica Acta,* vol. 441, no. 1, pp. 53-62, 2001.

[69] A. K. Ellerbee, S. T. Phillips, A. C. Siegel, K. A. Mirica, A. W. Martinez, P. Striehl, N. Jain, M. Prentiss and G. M. Whitesides, "Quantifying Colorimetric Assays in Paper-Based Microfluidic Devices by Measuring the Transmission of Light through Paper," *Analytical chemistry,* vol. 81, no. 20, pp. 8447-52, 2009.

[70] J. L. Delaney, C. F. Hogan, J. Tian and W. Shen, "Electrogenerated chemiluminescence detection in paper-based microfluidic sensors," *Analytical chemistry,* vol. 83, no. 4, pp. 1300-6, 2011.

[71] M. O'Toole and D. Diamond, "Absorbance based light emitting diode optical sensors and sensing devices," *Sensors,* vol. 8, no. 4, pp. 2453-79, 2008.

[72] F. d. Souza, G. Alves and W. Coltro, "Capillary-driven toner-based microfluidic devices for clinical diagnostics with colorimetric detection," *Analytical chemistry,* vol. 84, no. 21, pp. 9002-7, 2012.

[73] E. Hecht, Optics, 5th ed., Pearson Education, 2017.

[74] M. M. Braun and L. Pilon, "Effective optical properties of non-absorbing nanoporous thin films," *Thin Solid Films,* vol. 496, no. 2, pp. 505-514, 2006.

[75] R. Mansencal, "Cellulose," in *Polymer Data Handbook*, New York, NY, Oxyford University Press, 1999, pp. 39-48.

[76] L. S. RAMANATHAN, S. SIVARAM and M. K. MISHRA, "Polyurethane," in *Polymer Data Handbook*, Oxford University Press, Inc., 1999, pp. 870-873.

[77] D. F. Swinehart, "The beer-lambert law," *Journal of chemical education,* vol. 39, no. 7, p. 333, 1962.

[78] W. Seo, W. Yu, T. Tan, B. Ziaie and B. Jung, "Diaper-Embedded Urinary Tract Infection Monitoring Sensor Module Powered by Urine-Activated Batteries," *IEEE Trans. Biomed. Circuits and Systems,* vol. 11, no. 3, pp. 681-691, 2017.

[79] D. A. Skoog, D. M. West, F. J. Holler and S. R. Crouch, Fundamentals of Analytical Chemistry, 9ed, Belmont, CA: Brooks/Cole, Cengage Learning, 2014.

[80] "Typical Properties of Filter Papers and Glass Fiber Filters," GE Healthcare Life Sciences, [Online]. Available: https://bit.ly/2LWCMr0. [Accessed 20 June 2018].

[81] "VWR International – Filter papers - a guide," 06 2011. [Online]. Available: https://www.simada.co.il/images/filters/Whatman_filter_paper_guide_en.pdf. [Accessed 16 June 2018].

[82] E. T. F. b. T. L. C. o. t. (.-). B. Law, "Thomas G. Mayerhöfer; Harald Mutschke; Jürgen Popp," *ChemPhysChem,* vol. 17, no. 13, pp. 1948-1955, 2016.

[83] Z. Zhong, Z. Wang and G. Huang, "Investigation of wax and paper materials for the fabrication of paper-based microfluidic devices," *Microsystem technologies,* vol. 18, no. 5, pp. 649-659, 2012.

[84] E. Fu, S. A. Ramsey, P. Kauffman, B. Lutz and P. Yager, "Transport in two-dimensional paper networks," *Microfluidics and nanofluidics,* vol. 10, no. 1, pp. 29-35, 2011.

[85] E. W. Washburn, "The dynamics of capillary flow," *Physical review,* vol. 17, no. 3, pp. 273-283, 1921.

[86] P. Rai, B.-M. Lee, T.-Y. Liu, Q. Yuhui, E. Krause, D. S. Marsman and S. Felter, "Safety Evaluation of Disposable Baby Diapers Using Principles of Quantitative Risk Assessment," *Journal of Toxicology and Environmental Health, Part A,* vol. 72, no. 21-22, pp. 1262-1271, 2009.

[87] "Adult Diaper Reviews," XP Medical, [Online]. Available: https://www.xpmedical.com/adult-diaper-reviews. [Accessed 3 June 2018].

[88] J. M. L. i. a. t. a. J. M. L. t. a. J. M. LATINI, E. MUELLER, M. M. LUX, M. P. FITZGERALD and K. J. KREDER, "Voiding frequency in a sample of asymptomatic American men," *The Journal of urology,* vol. 173, no. 3, pp. 980-984, 2004.

[89] E. V. Haarst, E. Heldeweg, D. Newling and T. Schlatmann, "The 24- h frequency- volume chart in adults reporting no voiding complaints: defining reference values and analysing variables," *BJU International,* vol. 93, no. 9, pp. 1257-1261, 2004.

[90] M. Blanker, F. Groeneveld, A. Bohnen, R. Bernsen, A. Prins, S. Thomas and J. Bosch, "Voided volumes: normal values and relation to lower urinary tract symptoms in elderly men, a community-based study," *Urology,* vol. 57, no. 6, pp. 1093-1098, 2001.

[91] B. Haylen, D. Ashby, J. Sutherst, M. Frazer and C. West, "Maximum and average urine flow rates in normal male and female populations—the Liverposl nomograms," *BJU International,* vol. 64, no. 1, pp. 30-38, 1989.

[92] "Water Potential - Definition, Formula & Quiz," Biology Dictionary, [Online]. Available: https://biologydictionary.net/water-potential/. [Accessed 3 June 2018].

[93] M. Sasaki, M. J. Pugia, D. R. Parker, K. Kuromoto, I. Furukawa and I. Konishi, "Measurement of the albumin content of urinary protein using dipsticks," *Journal of clinical laboratory analysis,* vol. 13, no. 5, pp. 246-250, 1999.

[94] M. J. Pugia, J. A. Lott, J. A. Profitt and T. K. Cast, "High-sensitivity dye binding assay for albumin in urine," *Journal of clinical laboratory analysis,* vol. 13, no. 4, pp. 180-187, 1999.

VITA

Wuyang Yu received the B.S. degree in Microelectronics from Tsinghua University, Beijing, China, in 2012. He is currently pursuing the Ph.D. degree in Electrical and Computer Engineering at Purdue University, West Lafayette, IN, USA. Since September 2012, he has been a research assistant with Ziaie Biomedical Microdevices Laboratory, Purdue University. His research mainly focuses on developing low-cost and flexible microdevices and microsystems for biomedical sensing and drug delivery.

PUBLICATIONS

Journal Publications (7)

- H. Jiang, **W. Yu**, et al. "A Smart Capsule with a Hydrogel-Based pH-Triggered Release Switch for GI-Tract Site-Specific Drug Delivery." *IEEE Transactions on Biomedical Engineering* (2018).
- W. Seo, **W. Yu**, et al. "Diaper-Embedded Urinary Tract Infection Monitoring Sensor Module Powered by Urine-Activated Batteries." *IEEE transactions on biomedical circuits and systems* 11.3 (2017): 681-691.
- R. Rahimi, **W. Yu**, et al. "Directly embroidered microtubes for fluid transport in wearable applications." *Lab on a Chip* 17.9 (2017): 1585-1593.
- **W. Yu**, et al. "A Smart Capsule With GI-Tract-Location-Specific Payload Release." *IEEE Transactions on Biomedical Engineering* 62.9 (2015): 2289-2295.
- R. Rahimi, M. Ochoa, **W. Yu**, et al. "Highly stretchable and sensitive unidirectional strain sensor via laser carbonization." *ACS applied materials & interfaces* 7.8 (2015): 4463-4470.
- R. Rahimi, M. Ochoa, **W. Yu**, et al. "A sewing-enabled stitch-and-transfer method for robust, ultra-stretchable, conductive interconnects." *Journal of Micromechanics and Microengineering* 24.9 (2014): 095018.
- Q. Chen, **W. Yu**, et al. "Reliability of through-silicon-vias (TSVs) with benzocyclobutene liners." *Microelectronics Reliability* 53.5 (2013): 725-732.

Conference Publications (10)

- H. Jiang, **W. Yu**, et al. "A biodegradable sensor housed in 3d printed porous tube for in-situ soil nitrate detection." *Solid-State Sensors, Actuators and Microsystems Workshop,* Hilton Head, 2018.
- H. Jiang, **W. Yu**, et al. "A pH-sensitive hydrogel-based smart switch for GI-tract payload release." *Micro Electro Mechanical Systems (MEMS), 2017 IEEE 30th International Conference*.
- **W. Yu**, et al. "Modular customizable 3d-printed batteries for wearable applications", *The 20th International Conference on Miniaturized Systems for Chemistry and Life Sciences(MicroTAS), 2016.*
- **W. Yu**, et al. "A diaper-embedded disposable nitrite sensor with integrated on-board urine-activated battery for UTI screening." *Engineering in Medicine and Biology Society (EMBC), 2016 IEEE 38th Annual International Conference*.
- W. Seo, **W. Yu**, et al. "Diaper-embedded urinary tract infection monitoring system powered by a urine-powered battery." *Biomedical Circuits and Systems Conference (BioCAS), 2015 IEEE*.
- R. Rahimi, M. Ochoa, **W. Yu**, et al. "A highly stretchable pH sensor array using elastomer-embedded laser carbonized patterns." *Solid-State Sensors, Actuators and Microsystems (TRANSDUCERS), 2015 Transducers-2015 18th International Conference*.
- R. Rahimi, **W. Yu**, et al. "A low-cost fabrication technique for direct sewing stretchable interconnetions for wearable electronics." *Solid-State Sensors, Actuators and Microsystems (TRANSDUCERS), 2015 Transducers-2015 18th International Conference*.

- R. Rahimi, M. Ochoa, **W. Yu**, et al. "A facile fabrication technique for stretchable interconnects and transducers via laser carbonization." *Micro Electro Mechanical Systems (MEMS), 2015 28th IEEE International Conference.*
- R. Rahimi, M. Ochoa, **W. Yu,** et al. "Flexible supercapacitor based on MnO2 coated laser carbonized electrodes." *Journal of Physics: Conference Series*. Vol. 660. No. 1. IOP Publishing, 2015.
- **W. Yu**, et al. "Optical nitrite sensor and urine-activated electrochemical power source on paper through laser-assisted patterning and lamination." *Proceedings of the MicroTAS, San Antonio* (2014).

Patents (2)

- B. Jung, B. Ziaie, **W. Yu**, W. Seo, "DEVICES, SYSTEMS, AND METHODS FOR DETECTING TARGETED COMPOUNDS." WIPO Patent Application WO2017160399A1. 21 Dec. 2017. Print.
- B. Ziaie, R. Rahimi, and **W. Yu**. "Smart capsule with GI-tract-location-specific payload release." U.S. Patent Application No. 14/919,120.